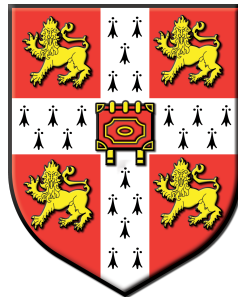


UNIVERSITY OF CAMBRIDGE

DOCTORAL THESIS

Incorporating Range Uncertainty into Proton Therapy Treatment Planning



Author:

Stacey Elizabeth McGowan

Supervisors:

Prof. Neil G. Burnet

Dr Simon J. Thomas

Selwyn College

This dissertation is submitted for the degree of

Doctor of Philosophy

in the Department of Oncology

Tuesday 14th April, 2015

In memory of my Grandmother

Janet Jenkins

6th July 1923 - 17th August 2014

Declaration

This dissertation is the result of my own work and includes nothing which is the outcome of work done in collaboration except as specified in the text. It is not substantially the same as any that I have submitted, or, is being concurrently submitted for a degree or diploma or other qualification at the University of Cambridge or any other University or similar institution except as specified in the text. I further state that no substantial part of my dissertation has already been submitted, or, is being concurrently submitted for any such degree, diploma or other qualification at the University of Cambridge or any other University or similar institution except as declared in specified in the text. It does not exceed the prescribed word limit for the relevant Degree Committee.

Stacey Elizabeth McGowan

April 2015

Acknowledgements

I would like to acknowledge and thank both my supervisors, Professor Neil Burnet and Dr Simon Thomas, for all their guidance and support. I would also like to acknowledge the support provided by Dr Hayley Woffendin.

I would like to thank everyone in Medical Physics, all the staff in the Radiotherapy and Oncology Departments at Addenbrooke's Hospital, the members of VoxTox and everyone who worked with me at the Paul Scherrer Institute in Switzerland, especially Professor Tony Lomax and Dr Francesca Albertini.

Thank you to the Medical Research Council for funding my research and financially supporting my project in Switzerland. Also thank you to the NHS, ACT, IPEM, PARTNER and CNAO who have all either contributed financially to this work or to my professional and academic development during my time at Cambridge. Thank you to ETH, Orsay Proton Centre and the Surrey Ion Beam centre for their contributions to this work in the form of data, lectures, presentations and interesting conversation.

I want to mention the support from my friends and family and thank them. I also want to thank Baden Rowing Club for their friendships and for making me feel so welcome during my time working in Switzerland.

Finally, a special thank you to the Trebilcock family and their amazing contribution to the Addenbrooke's Charitable Trust, supporting research in this area.

Abstract

This dissertation addresses the issue of *robustness* in proton therapy treatment planning for cancer treatment. Proton therapy is considered to be advantageous in treating most childhood cancers and certain adult cancers, including those of the skull base, spine and head and neck. Protons, unlike X-rays, have a finite range highly dependent on the electron density of the material they are traversing, resulting in a steep dose gradient at the distal edge of the Bragg peak. These characteristics, together with advancements in computation and technology have led to the ability to plan and deliver treatments with greater conformality, sparing normal tissue and organs at risk.

Radiotherapy treatment plans aim to meet set dosimetric constraints, and meet them at every fraction. Plan robustness is a measure of deviation between the delivered dose distribution and the planned dose distribution. Due to the same characteristics that make protons advantageous, conventional means of using margins to create a Planning Target Volume (PTV) to ensure plan robustness are inadequate. Additional to this, without a PTV, a new method of analysing plan quality is required in proton therapy.

My original contribution to the knowledge in this area is the demonstration of how site- and centre- specific robustness constraints can be established. Robustness constraints can be used both for proton plan analysis and to identify patients that require plans of greater individualisation. I have also used the daily volumetric imaging from patients previously treated with conventional radiotherapy to quantify range uncertainty from inter- and intra-fraction motion. These new methods of both quantifying and analysing the change in proton range in the patient can aid in the choice of beam directions, provide input into a multi- criteria optimisation algorithm or can be used as criteria to determine when adaptive planning may be required. This greater understanding in range uncertainty better informs the planner on how best to balance the trade-off between plan conformality and robustness in proton therapy.

This research is directly relevant to furthering the knowledge base in light of HM Government pledging £250 million to build two proton centres in England, to treat NHS patients from 2018. Use of methods described in this dissertation will aid in the establishment of clear and pre-defined protocols for treating patients in the future.

Table of contents

| | |
|--|-----------|
| Table of contents | 11 |
| List of figures | 13 |
| List of tables | 17 |
| Abbreviations | 21 |
| 1 Introduction | 1 |
| 1.1 The Cancer Burden | 1 |
| 1.1.1 NHS England | 2 |
| 1.2 Proton Therapy | 4 |
| 1.2.1 Accelerating Protons for Therapy | 6 |
| 1.2.2 Delivering Proton Therapy | 8 |
| 1.3 Treatment Planning | 13 |
| 1.4 Overview of PhD | 16 |
| 2 Uncertainties in Proton Therapy | 17 |
| 2.1 Uncertainties in Proton Planning | 17 |
| 2.1.1 Sources of Range Uncertainty | 17 |
| 2.1.2 Range Calculation Uncertainties in the Treatment Planning System | 19 |
| 2.1.3 Discrepancies Between Planned Dose and Delivered Dose | 21 |
| 2.2 Managing Uncertainties Including Positional Discrepancies and Motion . . | 23 |
| 2.2.1 Motion Mitigation | 23 |
| 2.2.2 Margins | 25 |
| 2.2.3 Probablistic Planning and Robust Optimisation | 26 |
| 2.2.4 Treatment Analysis and Validation | 30 |
| 2.3 Discussion | 31 |

| | | |
|----------|---|------------|
| 3 | A Method for Quantifying Random Range Uncertainty | 35 |
| 3.1 | Introduction | 35 |
| 3.2 | TomoTherapy | 38 |
| 3.3 | Calculating WEPL Changes in the CTV from TomoTherapy Shift & MVCT Data | 38 |
| 3.3.1 | Coding | 48 |
| 3.3.2 | Analysis | 51 |
| 3.4 | Summary | 52 |
| 4 | Quantifying Site-specific Range Uncertainty | 53 |
| 4.1 | Introduction | 53 |
| 4.2 | Methods and Materials | 53 |
| 4.3 | Results | 55 |
| 4.3.1 | Prostate | 55 |
| 4.3.2 | Head and Neck | 62 |
| 4.3.3 | Population Data | 69 |
| 4.4 | Discussion | 76 |
| 4.5 | Conclusion | 80 |
| 5 | Defining Robustness Protocols | 81 |
| 5.1 | Introduction | 81 |
| 5.1.1 | Methods and Materials | 82 |
| 5.1.2 | Retrospective Robustness Analysis | 85 |
| 5.2 | Results | 87 |
| 5.2.1 | Retrospective Robustness Analysis | 87 |
| 5.2.2 | How to use the Robustness Database in Practice | 89 |
| 5.3 | Discussion | 98 |
| 6 | Summary | 99 |
| 6.1 | Discussions | 99 |
| 6.2 | MVCT and Proton Therapy | 104 |
| 6.3 | Conclusion | 107 |
| | References | 109 |
| | Appendix A Published Work and Presentations | 121 |
| A.0.1 | Other Presentations | 125 |

Table of contents 13

Appendix B Code **129**

List of figures

| | | |
|-----|---|----|
| 1.1 | An illustration of the proton dose fall-off with depth known as the Bragg Peak. The target drawn above the Bragg peak represents how dose can be deposited in the tumour at depth in the patient. | 4 |
| 1.2 | The world showing current and planned proton therapy centres (Centre locations provided at (<i>Proton Therapy Today - The online magazine for proton therapy</i> , 2014), image created using Google Maps) | 5 |
| 1.3 | Photograph of the cyclotron at Orsay, which feeds 3 treatment rooms with a high energy of 230MeV | 7 |
| 1.4 | Photograph of the synchrotron at CNAO, Italy used to accelerate high energy protons and carbon ions for patient treatments | 8 |
| 1.5 | Schematic of Bragg peak delivery along a single profile through a target. (a) A flat spread-out Bragg peak (SOBP) is achieved by placing spots with increasing weights throughout the target to produce a uniform field, as used in passive scattering and single-field uniform dose. (b) Only the most distal single pristine Bragg peak (BP) is used for distal-edge tracking. (c) Optimally weighted spots are positioned throughout the volume to achieve fields with non-uniform doses for three dimensional intensity-modulated particle therapy. | 10 |
| 1.6 | Photo of a patient specific collimator | 11 |
| 1.7 | Photo of a scattering beam compensator | 11 |
| 2.1 | Schematic of sources of range uncertainties in proton therapy | 18 |
| 2.2 | Illustrating two parameters for optimisation, conformity and robustness, and how a Pareto front can be used to investigate clinically achievable plans with the same Pareto-optimised solution, but with different values of importance on robustness and conformity. | 30 |

| | | |
|-----|---|----|
| 3.1 | TomoTherapy at Addenbrooke's. Provides daily imaging with positional correction on all patients (<i>Burnet et al.</i> , 2010). | 38 |
| 3.2 | Example of how CT data (left image) can be converted into WEPL (right image) at a beam angle of 90° using calibration curves and ray-tracing | 39 |
| 3.3 | Image taken from the Addenbrooke's Radiotherapy Department's work instruction for carrying out MVCT HU QA using the Cheese phantom on TomoTherapy | 42 |
| 3.4 | Average MVCT IVDT from several months on both TomoTherapy units at Addenbrooke's | 45 |
| 3.5 | Calibration curve of MVCT HU to electron density relative to water | 45 |
| 3.6 | Calibration curve of MVCT HU to proton stopping power relative to water | 47 |
| 3.7 | Image of truncated patient on TomoTherapy showing the the scanning circle (white circle). | 50 |
| 4.1 | Heat plots of %volume range error histograms for prostate patients 4, 7, 21, 34, and 36 (in order top to bottom) with fraction using 0 and 90 degree beam angles. | 58 |
| 4.2 | Heat plots of %volume range error histograms for prostate patients 58, 72, 78 and 95 (in order top to bottom) with fraction using 0 and 90 degree beam angles. | 59 |
| 4.3 | Plots of the standard deviation for patients 4, 7, 21, 34, and 36 (in order top to bottom) of range error with fraction and beam angle. | 60 |
| 4.4 | Plots of the standard deviation for patients 58, 72, 78 and 95 (in order top to bottom) of range error with fraction and beam angle. | 61 |
| 4.5 | Screen shot of a single slice of Patient 78 showing the high dose CTV and approximate angles used to calculate WEPL | 63 |
| 4.6 | Heat plots of %volume range error histograms for all head and neck patients with treatment fraction at 0 and 25 degree beam angles. | 65 |
| 4.7 | Heat plots of %volume range error histograms for all head and neck patients with treatment fraction at 70 and 110 degree beam angles. | 66 |
| 4.8 | Heat plots of %volume range error histograms for all head and neck patients with treatment fraction at 180 degree beam angle. | 67 |
| 4.9 | Plots of the standard deviation of range error for each patient with fraction and beam angle. | 68 |

| | | |
|------|--|----|
| 4.10 | The fractional means of WEPL difference for each prostate patient was plotted as a histogram for both angles (top is 0° and bottom 90°). The total mean can be taken from these plots for each angle as well as the standard deviation which is the systematic component of the range error for these sites. | 70 |
| 4.11 | The fractional means of WEPL difference for each head and neck patient was plotted as a histogram for three angles (top is 0° , middle is 25° and bottom 70°). The total mean can be taken from these plots for each angle as well as the standard deviation which is the systematic component of the range error for these sites. | 71 |
| 4.12 | The fractional means of WEPL difference for each head and neck patient was plotted as a histogram for three angles (top is 110° and bottom 180°). The total mean can be taken from these plots for each angle as well as the standard deviation which is the systematic component of the range error for these sites. | 72 |
| 4.13 | The fractional means of WEPL difference for all prostate patients (top) and all the head and neck (bottom) were plotted as a histogram for all angles. The total mean can be taken from these plots as well as the standard deviation. | 73 |
| 4.14 | The binned prostate data for each beam angle from each fraction for all patients was summed and plotted as a histogram normalised to one. Each colour represents a beam angle, and the black histogram is of all binned data. | 74 |
| 4.15 | The binned Head and neck data for each beam angle from each fraction for all patients was summed and plotted as a histogram normalised to one. Each colour represents a beam angle, and the black histogram is of all binned data. | 75 |
| 4.16 | Example of tooth filling artefact in kV CT image (left) and in MVCT image (right) | 78 |
| 4.17 | Possible weight loss leading to negative Σ for Head and Neck. Images left to right of patients 52, 91, 92 | 78 |
| 5.1 | The ebDD represents in each voxel a dose-error-bar that brackets the calculated deviations from the nominal dose distribution. Here are the screenshots of the nominal plan (using typical PSI beam arrangements referenced as $A(4f)$ in this chapter) and the ebDD calculated for $\pm 3\%$ HU from one patient. | 83 |

| | | |
|-----|--|-----|
| 5.2 | The A(4f) plan consists of four non-coplanar fields, two posterior oblique and two anterior lateral oblique fields. Clockwise from top left the beam angles and couch twists used are (290°, 340°), (70°, 20°), (110°, 20°) and (250°, 340°), where the first angle is the gantry orientation and the second is the table orientation. | 86 |
| 5.3 | Robustness results, represented as percentage dose uncertainty for 16 skull-base IMPT plans from 8 patients to both the range and set-up uncertainties modelled in (a) in the brainstem, (b) in the chiasm and (c) in the CTV. On each box plot the central mark is the median, the edges of the box are the 25th and 75th percentiles, the whiskers extend to the most extreme data points not considered outliers, and outliers are plotted individually. Outliers are considered points $\pm 2.7\sigma$ | 88 |
| 5.4 | Volume Histogram of (a) systematic range uncertainties and (b) random set-up uncertainties for an underdose scenario in the CTV for five plans of different beam orientations. | 91 |
| 5.5 | Dose distribution for the A(4f) (top left) and B(4f) (top right) plans and ebDD of systematic range uncertainties for the worst-case underdose scenario for the A(4f) (bottom left) and B(4f)(bottom right) treatment plans showing the CTV in green. | 92 |
| 5.6 | Dose distributions from the A(4f) (top left) and B(4f) (top right) plans and the corresponding ebDD from B(4f) (bottom left) and A(4f) (bottom right) treatment plans showing the brainstem in green and the target in yellow. . . | 94 |
| 5.7 | Volume histogram of (a) the systematic range uncertainties, (b) the random set-up uncertainties for an overdose scenario in the brainstem and (c) the random set-up uncertainties for overdose scenario in the chiasm, for five plans of different beam orientations. | 95 |
| A.1 | REVIEW ARTICLE: Treatment planning optimisation in proton therapy . . | 122 |
| A.2 | Accepted ESTRO33 ePoster 2014 | 123 |
| A.3 | Winning popular press poster describing my research to the general public at the School of Clinical Medicine Research day 2012 | 126 |
| A.4 | Copy of my certificate for presenting a popular press poster at the clinical school Research day | 127 |

List of tables

| | | |
|-----|---|----|
| 1.1 | Proton beam delivery techniques, production methods and planning techniques. The further down the table, the more conformal the technique . . . | 12 |
| 3.1 | Calculating a mean β to use in the Bethe-Bloch equation to establish an energy independent proton stopping power relative to water | 43 |
| 3.2 | calculation of proton stopping power relative to water for each tissue using the energy specific β in the Bethe-Bloch equation. The I-values have been interpolated from the Gammex data tables | 44 |
| 3.3 | Table of density inserts used to calibrate the MVCT and their corresponding physical densities, estimated electron densities and proton stopping powers relative to water as calculated from the Bethe-Bloch equation using the β value to a 150MeV proton beam | 46 |
| 4.1 | Prostate data showing the target and number of fractions used. The final column shows the percentage of fractions that did not suffer target truncation at daily imaging | 57 |
| 4.2 | Table of Intra-fraction changes in WEPL for a single prostate patient, 58, at beam angles 0° and 90° | 63 |
| 4.3 | Table of Head and Neck data showing the targets and number of fractions used. The final column shows the percentage of fractions that did not suffer target truncation at imaging | 64 |
| 4.4 | Table of prostate range error in mm for all patients at each beam angle. . . . | 74 |
| 4.5 | Table of head and neck range error in mm for all patients at each beam angle | 75 |
| 5.1 | Descriptions of each plan | 87 |
| 5.2 | The use of retrospective plan analysis to establish planning parameters of robustness | 89 |

- 5.3 Robustness values for each parameter set in the site specific robustness database in Table 5.2 for plans A(4f) and B(4f). Bold italic values are those that are out of tolerance 96
- 5.4 This table shows robustness results from the original A(4f) plan that patient X was treated with and those from the re-plan created for this work B(4f). Tolerances have not been set for these OARs as they had for the brainstem and chiasm in the robustness database, but they have been supplied here to use to further compare plans. 97

Abbreviations

4DCT Four Dimensional Computed Tomography

BP Bragg Peak

CBCT Cone Beam Computed Tomography

CNAO Centro Nazionale di Adroterapia Oncologica

CNS Central Nervous System

CPAC Compact Particle Acceleration Corporation

CRUK Cancer Research UK

CT Computed Tomography

CTV Clinical Target Volume

DDA Dose Difference Analysis

DECT Dual Energy Computed Tomography

DET Distal Edge Tracking

DH Department of Health

DICOM Digital Imaging and Communications in Medicine

DVH Dose Volume Histogram

DWA Dielectric wall accelerator

ebDD error-bar Dose Distribution

ebDD error-bar Dose Distribution

ebVH error-bar Volume Histogram

FOV Field of View

GTV Gross Tumour Volume

HU Hounsfield Unit

ICRU International Committee on Radiation Units and Measurements

IGRT Image Guided Radiotherapy Treatment

IMPT Intensity-Modulated Particle Therapy

IMRT Intensity-Modulated Radiotherapy

IVDT Image Value Density Table

kVCT Kilovoltage Computed Tomography

Linac Linear Accelerator

MCO Multi-Criteria Optimisation

MVCT Megavoltage Computed Tomography

NICE National Institute of Health and Care Excellence

NRAG National Radiotherapy Advisory Group

OAR Organ at Risk

PET Positron Electron Emission

PRV Planning organ at Risk Volume

PSI Paul Scherrer Institute

PTV Planning Target Volume

QALY Quality-Adjusted Life Years

RBE Relative Biological Effectiveness

RF Radio Frequency

ROI Region of Interest

SFUD Single Field Uniform Dose

SID Source to Isocentre Distance

SOBP spread-out Bragg peak

TPS Treatment Planning System

VOI Volume of Interest

WEPL Water Equivalent Path-Length

Chapter 1

Introduction

Throughout the first two chapters I have reproduced, with permission, the literature review which I wrote, entitled *Treatment planning optimisation in proton therapy* published in the British Journal of Radiology (*McGowan et al.*, 2013).

1.1 The Cancer Burden

Cancer is a major worldwide health problem with approximately 11 million people being diagnosed with cancer and 7 million people dying from cancer each year (*Dosanjh et al.*, 2008). Cancer Research UK (CRUK) reports that in the UK there were 331,487 cancer cases in 2011, 274,233 of which presented in England alone. Of these, 7490 cases were brain, other central nervous system (CNS) and intracranial tumours (*Cancer Research UK*, 2014c). Based on the same set of statistics, childhood cancers (<14 years) account for approximately 1% of cancer cases in the UK with 1,574 new cases of cancer diagnosed in children between 2009 and 2011. Brain, other CNS and intracranial tumours are the most common cause of childhood cancer death. (*Cancer Research UK*, 2014a).

Despite increased post-diagnosis life expectancy due to developments in early diagnosis and treatment, incidences of cancer will increase in the coming years due to the increasing lifespan of the general population. Of the adult patients diagnosed with a malignant tumour, CRUK estimates that 50% will survive their cancer for at least 10 years (*Cancer Research UK*, 2014b). For 40% of these patients, radiotherapy will play a role in their treatment, whether on its own or as part of a combined therapy. This corresponds to around 100,000 patients receiving radical radiotherapy each year in the UK; for 60% of patients it is given with curative intent. Radiotherapy includes external beam radiotherapy and also

brachytherapy. External beam radiotherapy can include the use of high energy photons, electrons, protons or carbon ions. In this thesis photon based, or X-ray based radiotherapy, will be referred to as *conventional radiotherapy* whereas radiotherapy using protons will be referred to as *proton therapy*. Other forms of particle therapy are beyond the scope of this thesis, the focus of which is on developments in proton therapy in line with the prospect of bringing proton therapy to England.

1.1.1 NHS England

In 2007, the National Radiotherapy Advisory Group (NRAG) recommended for the Department of Health to give NHS patients access to proton therapy (*Department of Health, 2014*). A business case was proposed to establish English proton therapy centres and in the meantime overseas access was established. In the UK, patients have been able to access proton therapy abroad under the auspices of the National Health Service Proton Overseas Programme since 2008 (*NHS Specialised Services, 2011*). Between 2008 and 2012 160 patients, 107 of whom were children, were treated with proton therapy overseas. In 2009 NRAG determined that there was a need to treat up to 1,487 patients from England and the devolved administrations with proton therapy each year. Four hundred of these patients are classed as high priority patients, consisting of a casemix of complex cases including adults, children and very young children (*Department of Health, 2014*).

The decision to establish two proton therapy centres in the UK was made based on the costs, benefits and risks of each option investigated. Two centres, one in Manchester and one in London, has been determined to be the most cost effective option for the provision of the NHS service. This solution is based on the incremental cost effectiveness ratio of each option compared to the baseline option, misleadingly named, ‘do nothing’.

The ‘do nothing’ option refers to the cost to treat these patients with conventional radiotherapy within the UK. Conventional radiotherapy is priced in fractions, with each fraction costing between £85 and £242. This works out on average, £7,500 to treat a child, and £4,600 to treat an adult (*Department of Health, 2014*). The measure of benefit to a patient from carrying out an intervening treatment is measured in Quality-Adjusted Life Years, or QALYs . QALYs take into account both the quantity and quality of life created by the intervening healthcare, in this case radiotherapy. It is the product of life expectancy and a measure of the quality of the remaining life-years. A QALY places a weight on the time the patient has at different levels of healthiness. For example a year of perfect health is worth 1

and a year of less than perfect health is worth less than 1, with death considered to be equivalent to zero (*Phillips, 2009*). The estimate of QALYs per patient gained over their lifetime from radiotherapy treatment is between 9.4 and 14 years (*Department of Health, 2014*). This is the ‘do nothing’ baseline: on average from radiotherapy treatment one quality-adjusted life year costs £517. However, it should be noted that the concept of the QALY has limitations; it is based on survival probabilities and does not take into account the context of each given patient’s life or chronic side effects from treatment such as deafness or a drop in IQ (*Phillips, 2009*). However, the QALY is a useful metric for comparing treatment options in terms of benefit received and the cost incurred.

Models have been used to determine the difference in QALYs between treating patients deemed to benefit from proton therapy based on current evidence. It was estimated that the high priority patients could benefit from an extra 2.5 QALYs from being treated with proton therapy over conventional radiotherapy and other patients referred for protons could gain 1.8 extra QALYs from this treatment (*Department of Health, 2014*). Based on this, the number of patients treated per year and the 30-year lifetime of the machines the cost is £19,187 per QALY. Due to that fact that 80% of the estimated costs are fixed, it is the limited throughput of patients that drives the cost up. To put this into perspective, NICE’s (National Institute for Health and Care Excellence) notional threshold on per QALY cost is £30,000. Costs for drugs such as trastuzumab (Herceptin) and imatinib (Glivec), which are both supplied on the NHS are above this threshold (*Towse, 2002*). It is estimated that each of the two centres will treat 675 patients each a year. The low throughput takes into account the complicated casemix of patients to be treated. There is no facility in the world that treats an equally complex casemix of patients as those proposed for England.

On the 10th February 2012, the Her Majesty’s Treasury and the Department of Health formally confirmed full approval of the Strategic Outline Case for the National Proton Beam Therapy Development Programme, pledging £250 million (*Department of Health, 2014*). It has decided that all patients treated in England with proton therapy, will be treated within clearly pre-defined protocols (*Department of Health, 2014*). With the aim to provide further evidence of the effectiveness of proton therapy every patient will also be enrolled into a prospective programme of evaluation with outcome tracking. It is hoped that the centres will start to treat patients in 2018 (*Burnet et al., 2012; www.dh.gov.uk, 2012*), such that developments discussed within this thesis will be directly relevant.

1.2 Proton Therapy

The aim of radiotherapy is to create and deliver the ideal treatment plan, where the target volume receives 100% of the prescribed dose and normal tissue receives 0% (Bortfeld, 1999). It is, however, impossible to achieve this perfect balance. Instead, multiple trade-offs are required to achieve a clinically acceptable plan, so the problem becomes one of optimisation.

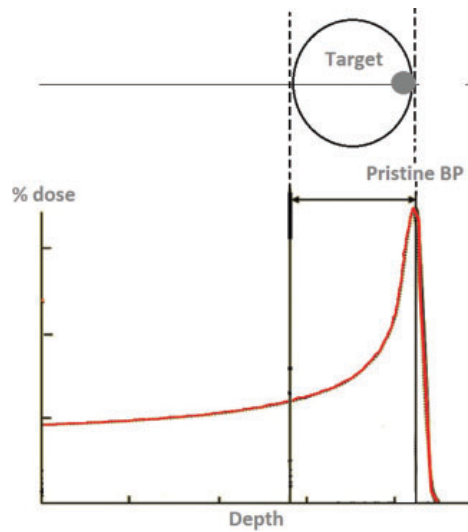


Fig. 1.1 An illustration of the proton dose fall-off with depth known as the Bragg Peak. The target drawn above the Bragg peak represents how dose can be deposited in the tumour at depth in the patient.

The nature of proton therapy makes the aim of cure without complications potentially more achievable due to the highly localised deposition of dose in the characteristic Bragg peak (Bragg, 1904) (see Figure 1.1). This relates predominantly to the ability to deliver high doses of radiation close to normal tissue structures which are dose-limiting in conventional X-ray treatments, and to the finite range of protons, which results in a reduced integral dose to surrounding normal tissues. However, for a plan to be optimal it must also be deliverable. The term *robustness* is used within this thesis to define how well a plan can maintain its dosimetric integrity at every fraction throughout the patient's treatment. It is the finite range and the steep dose gradients achievable in proton beam therapy that lead to its inherent lack of robustness when compared to conventional radiotherapy.

From a clinical perspective, the exact role of proton therapy has yet to be defined. However,

for childhood cancers proton therapy delivers a lower dose to tissues around the tumour and lower whole body dose. This results in less growth disturbance and lower risk of secondary malignancies, compared to X-rays. There is also the suggestion that the use of proton therapy can reduce impairment of neuropsychological and IQ development (*Merchant et al.*, 2008). In adults, proton therapy seems particularly effective in the treatment of radio-resistant tumours close to critical structures such as the brain stem and spinal cord. For example, outstanding results have been published for the use of proton therapy in the treatment of chordoma and chondrosarcoma (*Ares et al.*, 2009). The current evidence for the use of proton therapy at different sites has been extensively reviewed (*Allen et al.*, 2012; *Ares et al.*, 2009; *De Ruyscher et al.*, 2012; *Jones*, 2008). The reader is referred to the literature (*Durante and Loeffler*, 2010; *Lodge et al.*, 2007; *Ramaekers et al.*, 2011; *van de Water et al.*, 2011) for more clinical data. Nevertheless, substantial opportunity for further clinical research development and evaluation remains (*McGowan et al.*, 2013).

Presently, proton therapy has not been investigated to either the desired or required extent through clinical trials. This is due to several factors including limited samples sizes, ethical implications (*Glimelius and Montelius*, 2007; *Sheehan et al.*, 2014) and, most significantly, the lack of experience as compared to that in conventional radiotherapy. A significant advantage of conventional X-ray therapy over proton therapy is the wealth of experience and knowledge available. A key area for optimising the treatment planning process is in gaining experience in planning proton treatments. The number of proton facilities available worldwide is rapidly increasing (Figure 1.2), yet there is a substantial shortage of oncologists, dosimetrists and physicists with the required expertise (*Dosanjh et al.*, 2008).

1.2.1 Accelerating Protons for Therapy

The aim of radiotherapy is to be able to deliver the desired dose anywhere in a patient and for protons, the penetration depth is energy dependent. Therefore to be able to adequately treat to depths of 26-38cm in a patient, beam energies of 200-250 MeV are required. The energy also needs to be variable during treatment delivery to allow for uniform coverage of the treatment volume at all depths. It is also required that the treatment delivery time be as short as possible so that more patients can be treated, for patient comfort, and to reduce uncertainties caused by motion. Depending on the delivery system used, to achieve a 2Gy dose uniformly to a target volume of 1 litre in 1 minute intensities of about $3\text{-}6 \times 10^{10}$ particles per second are required (*ICRU 78*, 2007). The current methods for accelerating protons for radiotherapy are briefly described.



Fig. 1.2 The world showing current and planned proton therapy centres (Centre locations provided at (*Proton Therapy Today - The online magazine for proton therapy*, 2014), image created using Google Maps)

Cyclotron

The cyclotron, (Figure 1.3), was invented by Ernest Lawrence in 1929 (*Lawrence*, 1934). It uses a large magnet to confine the motion of the particles to that of a spiral path. As particles enter into the opposite half of the accelerator, known as a ‘dee’, they are accelerated by a radio frequency (RF) electric field. A large potential difference is applied across the gap between the dees, giving particles a ‘kick’ every half orbit. As they gain energy the radius of their orbit increases spiralling outward until they are extracted at the maximum radius, and energy, capable for the dimensions of the cyclotron. For non-relativistic particles, $Bvq = \frac{mv^2}{r}$, where B is the magnetic field, q is the charge of the particle, v is the velocity of the particle, m is the mass of the particle and r is the radius of orbit. In considering the frequency, f, of the RF field required, the relationship between frequency, velocity and radius can be used. Since $\omega = 2\pi f = \frac{v}{r}$ then, $f = \frac{Bq}{2\pi m}$. This shows that for a particle with a constant mass the frequency is independent of the radius and so a fixed RF can be used. This only works for non-relativistic cases as the particles nears the speed of light its mass will increase and this convenience no longer stands (*Kirby*, 2010)). There are two types of accelerators to work around this problem. One is a Synchrocyclotron that uses a variable RF. The other is an isochronous cyclotron, which increases the magnetic field with radius.



Fig. 1.3 Photograph of the cyclotron at Orsay, which feeds 3 treatment rooms with a high energy of 230MeV

Synchrotron

The synchrotron has a fixed radius so that a bunch of particles can be confined in an evacuated pipeline (see Figure 1.4). The particles travel in straight segments with bending magnets in between. The particles are accelerated using an RF oscillator that supplies an energy boost each time a particle passes through the accelerating cavity. The RF increases as the particles increase in energy and velocity and is synchronised with an increase in the magnetic field in the bending magnets. The synchrotron offers a flexible energy variation system where the beam energy can quickly be changed instead of using a physical range modifier in the treatment delivery system. A limitation though is the number of particles per bunch and therefore a limit on intensity.

New Technology

As all the methods of particle acceleration mentioned above require large accelerators to be built they cannot be used on a gantry as with conventional radiotherapy Linacs (radiotherapy linear accelerators). This means that one accelerator will feed particles to several treatment rooms allowing only one treatment room to operate at a time. Several new technologies are being developed by different groups to overcome these problems.

- The Dielectric wall accelerator (DWA) - The Compact Particle Acceleration Corporation (CPAC) is developing and commercializing a highly compact fixed beam



Fig. 1.4 Photograph of the synchrotron at CNAO, Italy used to accelerate high energy protons and carbon ions for patient treatments

intensity-modulated proton therapy (IMPT) system powered by the dielectric-wall accelerator. DWA uses high gradient linear accelerator technology to produce a compact accelerator capable of producing proton energies up to 200MeV and suitable for gantry mounting (*Caporaso et al.*, 2009).

- Laser plasma particle accelerators can create a very large and localised electric field using a laser to knock protons from a thin target. It is theorized that by using a given target thickness, therapeutic energies can be reached using an accelerator that can be mounted on a gantry (*DeLaney and Kooy*, 2008).
- Non-Scaling Fixed Field Alternating Gradient accelerator known as PAMELA in the UK. This design aims to incorporate the best qualities of a cyclotron (fixed magnetic field) for rapid acceleration and of a synchrotron (alternating gradient) for variable energy extraction. This group envisage that this type of accelerator will be able to be gantry mounted and will be suitable for delivering spot scanning and rescanning techniques (*Peach et al.*, 2009).

1.2.2 Delivering Proton Therapy

The choice in how the protons are delivered can have a large impact on the ability to both produce conformal dose distributions, and to produce plans that are robust to uncertainties. There are three main treatment delivery techniques used clinically (Table 1.1):

1. passive scattering (*Haberer et al.*, 1993),
2. uniform, and
3. active scanning (*DeLaney and Kooy*, 2008; *Pedroni et al.*, 1995).

These techniques are used to broaden the narrow proton beam created by the accelerator into one that can achieve uniform dose coverage of the target at all depths. This is achieved for passive scattering and uniform scanning through the delivery of so-called spread-out Bragg peaks (SOBP) (Figure 1.5). Orthogonal to the beam direction, the beam is spread using carefully designed scatterers (for passive scattering) or by continually deflecting the proton beam in a regular pattern orthogonal to the beam direction with constant intensity (uniform scanning). For both approaches, three-dimensional (3D) conformation of the final dose to the target is achieved through the additional use of patient- and field-specific collimators (which conform the dose in directions orthogonal to the beam - see Figure 1.6) and compensators (which conform the dose in the beam direction - see Figure 1.7) inserted in the beam nozzle (*DeLaney and Kooy*, 2008). Active scanning also uses magnets to scan the proton beam across the target volume. In contrast to uniform scanning, however, active scanning allows the fluence (dose) applied at each Bragg position to be continuously varied. Active scanning can offer an advantage to the patient by allowing for greater flexibility in the delivered dose and a reduction in integral dose to healthy tissues. This allows for the delivery of intensity-modulated particle therapy (IMPT) (*Lomax*, 1999), which is analogous with Intensity- Modulated Radiotherapy (IMRT) in conventional radiotherapy. Although there is in principle, a continuum of solutions to the IMPT problem, at its extremes IMPT can be divided into two *flavours*: distal-edge tracking (DET) (*Deasy*, 1998), where Bragg peaks are placed only at the edges of the target volume, and 3D IMPT (*Lomax*, 1999), where Bragg peaks are optimally distributed and weighted throughout the target volume (Figure 1.5). IMPT allows for delivery of single inhomogeneous but optimised fields to produce a final homogeneous dose distribution in the target volume. This permits the planner to be more flexible in the placement of residual dose to healthy tissues. However, although IMPT offers greater optimisation of dose delivery at the planning stage, it has the potential to be especially sensitive to range uncertainties (*Nil et al.*, 2004; *Oelfke and Bortfeld*, 2000). Table

1.1 summarises all these modes of producing and manipulating proton dose distributions.

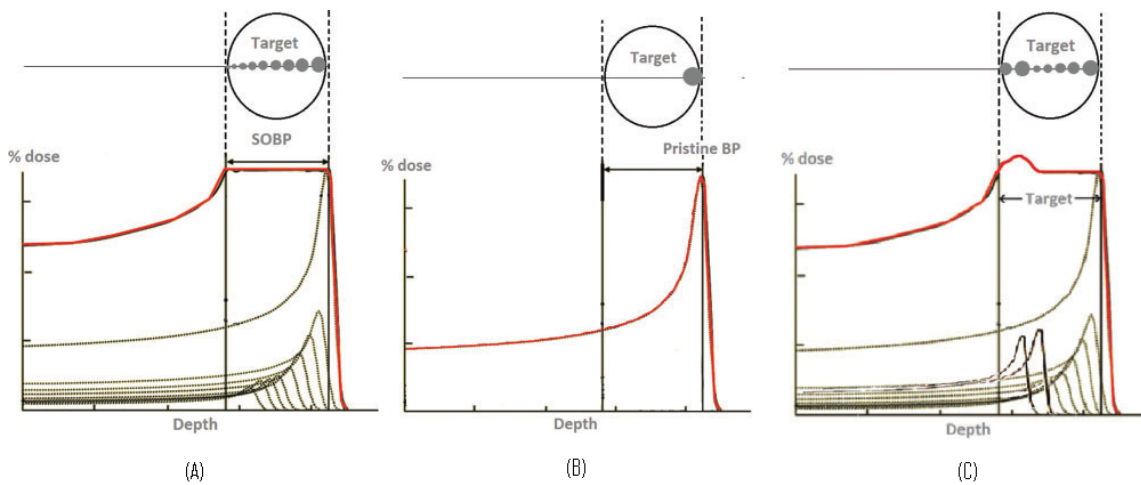


Fig. 1.5 Schematic of Bragg peak delivery along a single profile through a target. (a) A flat spread-out Bragg peak (SOBP) is achieved by placing spots with increasing weights throughout the target to produce a uniform field, as used in passive scattering and single-field uniform dose. (b) Only the most distal single pristine Bragg peak (BP) is used for distal-edge tracking. (c) Optimally weighted spots are positioned throughout the volume to achieve fields with non-uniform doses for three dimensional intensity-modulated particle therapy.



Fig. 1.6 Photo of a patient specific collimator

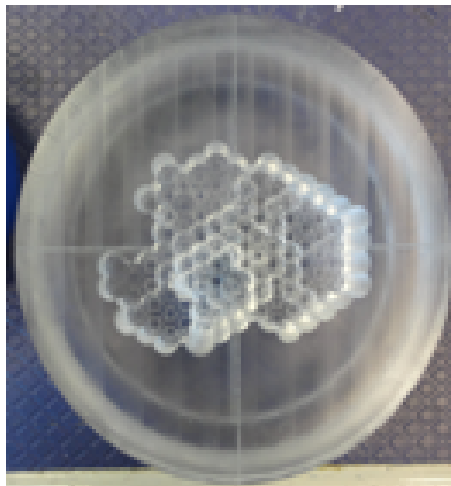


Fig. 1.7 Photo of a scattering beam compensator

Table 1.1 Proton beam delivery techniques, production methods and planning techniques. The further down the table, the more conformal the technique

| Methods of producing a clinical proton beam to treat entire target volume | Descriptions |
|---|---|
| Passive scattering | Works on the principle that high atomic number materials, such as lead, scatter the beam with minimum energy loss and low atomic number materials, such as plastic, decrease proton energy with minimum scatter. Combining these materials to produce patient-specific collimators and compensators results in a conformal treatment beam with a spread-out Bragg peak. |
| Uniform scanning | This is similar to passive scattering with the difference that the beam is spread in the lateral direction through magnetically deflecting the beam with constant fluence instead of using a scattering foil. Different spot weights are produced using a compensator, as in passive scattering |
| Active Scanning | This uses magnetic fields to deflect the path of each proton beam towards the planned position in the target volume. Individual Bragg peaks are distributed within the target volume and the cumulative effect produces an effective SOBP without the need for compensators. This is achieved by either continuous magnetic scanning or spot scanning. The latter is analogous to the step-and-shoot mode in IMRT, i.e. a non-continuous delivery of dose, where the exact position is determined before the dose is delivered |
| Methods of achieving adequate dose distributions | Descriptions |
| Single Field Uniform Dose (SFUD) | Single individually optimised proton fields that each deliver a homogeneous dose to a volume. If necessary, these can be combined by simple addition |
| Field patching | The sharp distal edge dose gradient can be matched up to the lateral edges of another “patch” field to produce a continuous dose distribution. Where possible, equivalent opposite fields are also used to reduce the potential for dose variation at the abutting edges. Multiple fields in patch work can be used to achieve multiple dose gradients inside a treatment volume. Field patching is a 3D extension of matching lateral field edges. Therefore, if multiple fields are used, each one can deliver a homogeneous dose to part of the volume |
| IMPT | IMPT is analogous to IMRT, and is a mode of treatment delivery achievable only with active scanning beams. IMPT uses narrow proton beams which are magnetically moved over the volume in the transverse plane while the energy and intensity are altered to control dose to a point and sculpt the dose at depth. Unlike SFUD treatments, IMPT can deliver a number of non-uniform fields to produce the desired dose distribution. |
| "Flavours" of IMPT | Descriptions |
| 3D IMPT | This is most similar to IMRT. Bragg peaks are placed throughout the entire volume and their weights optimally adjusted. |
| DET | DET is a method by which pristine Bragg peaks of optimal weights are distributed only along the distal edge of the target and not throughout the target volume. |

1.3 Treatment Planning

The developments in technology have allowed for the ability to deliver treatments of greater conformality and complexity in radiotherapy. This led to the need for treatment planning using inverse planning and optimisation. In current inverse planning systems for IMRT the dose distribution is determined using a computerised optimisation based on dose objectives for targets and other volumes which have been assigned an importance level (*Thieke et al.*, 2007). To determine the plan quality, a number is assigned based on the deviation from objective dose for each volume and the optimisation result is the plan with the lowest number. This is a trial and error process, given that the resulting plan may not be clinically acceptable and the importance levels assigned to each volume may need adjusting and the optimisation re-run. This can be time-consuming and the best-quality plan may not have been achieved as the planner cannot try every combination of parameters. There also exists a problem that, if upper and lower constraints are met, the optimisation process will not further improve doses to these volumes. This means that IMRT and IMPT cannot necessarily be exploited to their full potential owing to limitations with inverse planning (*Thieke et al.*, 2007).

Besides meeting planning constraints the treatment plan is also required to meet the aims of the planner *at each and every fraction*. The ability to plan and deliver treatments of greater conformality and complexity led to the need for uniform recording, reporting and prescribing to account for geometric uncertainties. An *uncertainty* refers to any variation between the planned and delivered dose distribution and they arise from the fact that treatment plans are based on a static view of a living, and therefore, a very non-static patient. The variation between the planned dose distribution and the delivered dose distribution is a measure of a plan's robustness: the smaller the variation the greater the plan robustness. Residual uncertainties are unavoidable despite efforts in variation reduction such as patient immobilisation and image guided radiotherapy treatment (IGRT). International Committee on Radiation Units and Measurements (ICRU) Reports 50 and 62 (*ICRU 50*, 1993; *ICRU 62*, 1999) provided a solution by defining target volumes in conventional radiotherapy including the Gross Tumour Volume (GTV), the visible tumour, the Clinical Target Volume (CTV), which includes the GTV and microscopic growth, and the Planning Target Volume (PTV) which encompasses both the GTV and CTV as well as accounting for any deviations from our static model. Analogous to the PTV, a Planning organ at Risk Volume (PRV) is used for Organs at Risk (OAR) (*ICRU 83*, 2010).

In regard to conventional radiotherapy, *Stroom et al.* (1999) and *van Herk et al.* (2000)

suggested that uncertainties fall into two categories, namely preparation and treatment execution uncertainties. Treatment execution uncertainties are random and act to blur the ideal dose distribution by a Gaussian distribution with a width dependent on the photon penumbra and the standard deviation of day-to-day variations in the CTV location. Preparation uncertainties are present at every fraction of the treatment and are therefore systematic in nature. Using the shift invariance assumption, systematic uncertainties result simply in a shift of the dose distribution with the same direction and magnitude.

Van Herk also addressed the problem of how to combine both these types of uncertainty in an analytical model to determine the CTV-PTV margin. It was shown that it was incorrect to combine the standard deviations of the uncertainties linearly due to the lack of correlation between systematic and random uncertainties. It was acknowledged that the systematic uncertainty is stochastic across the patient population. Van Herk's PTV margin for systematic uncertainties is defined so that the CTV has a 90% chance of being in the PTV. This, now well known, margin recipe (equation 1.1) allows that in 90% of patients treated to meet the ICRU recommendations, the CTV receives at least 95% of the prescribed dose.

$$PTVmargin = 2.5\Sigma + 1.64(\sqrt{(\sigma_p^2 + \sigma^2)}) - 1.64\sigma_p \quad (1.1)$$

where, Σ is the standard deviation of the systematic uncertainty, σ is the standard deviation of the random uncertainty and σ_p is the unblurred beam penumbra width. In this paper Van Herk (*van Herk et al.*, 2000) suggests redefining the PTV as,

"The volume defined in treatment room coordinates to which the prescribed dose must be delivered in order to obtain a clinically acceptable and specified probability that the prescribed dose is actually received by the CTV, which has an uncertain location."

In this way uncertainties are condensed into the CTV-to-PTV margin. The *static PTV* represents the *moving CTV* and is therefore a useful method of evaluating a plan, by using Dose Volume Histograms (DVHs) to report the minimum dose to the CTV with a pre-specified confidence level. The PTV then becomes a surrogate target for both treatment plan optimisation and evaluation.

Planning with a PTV has some limitations; for example it is problematic in cases where the CTV is close to the skin. It is important that there is confidence in quantifying and identifying uncertainties used to grow the PTV margin and that they are specific for treatment site,

modality used, and treatment regime to ensure optimal treatment. In using Image Guided Radiotherapy (IGRT) greater information about the systematic uncertainty can be acquired, allowing for corrections to be made and a reduction in the margins used. IGRT is the use of imaging at pre-treatment and delivery to improve or verify the accuracy of radiotherapy. IGRT includes methods of simple visual field alignment checks, to the more complex volumetric imaging that allows direct visualisation of the target volume and surrounding anatomy (*NRIG*, 2012). In the case of online IGRT (where the images are analysed and used on set), information about the random component can be gained and corrected for by applying rigid shifts to the treatment table, aligning either soft tissue or bony landmarks in the daily image to the planning image. This again, allows for a reduction in the CTV to PTV margin. However, if reduced too much the margin may become inadequate and the tumour control probability or other endpoint may worsen, such as biochemical failure as seen by (*Engels et al.*, 2009). If the margin is too large, greater incidence and severity in normal tissue complication may be seen.

Furthermore, the PTV concept is still present in newer approaches where inhomogeneous doses are prescribed. Such cases are in conflict with several of the underlying assumptions taken in van Herk's original margin design. As a consequence, the indirect estimation of the confidence level becomes unreliable. Intensity modulated particle therapy (IMPT) is one such example, where complex and inhomogeneous dose distributions are delivered, often with steep dose gradients. Along with the extra degree of freedom in the proton range, this renders the PTV an inadequate planning tool. This is partly due to the shift invariance assumption (also known as *static-cloud*) as it cannot be applied to the proton case. This assumption relies on a rigid isocentric shift of the dose distribution, in the same direction and magnitude as the geometric uncertainty, and is representative of the delivered dose when experiencing the same geometric uncertainty. For example if a shift, S is applied, this means that the dose value at a voxel D_i , is now $D_{(i-S)}$. The shift invariance relies on assuming the patient contour is unchanged when the dose isocentre is moved and also on the radiation passing through tissue of the same density before and after the dose isocentre shift (*Nguyen et al.*, 2009). The sensitivity of the proton range to density heterogeneities in the traversing material means this assumption can no longer be made. Even if there has been no shift by the patient and no change in the tumour size, shape or positioning there is still an uncertainty due to changes in the radiological path-length, resulting from patient changes such as weight gain or loss.

1.4 Overview of PhD

With the primary focus on including range uncertainty into proton therapy treatment planning, the purpose of this PhD is to explore how range uncertainties may be quantified and to develop a solution for evaluating plan quality in terms of robustness that can be included into the treatment planning workflow. The structure of the thesis is as follows:

Chapter 2 The current knowledge of range uncertainties, including source, magnitude and management, as well as their impact on proton dose is discussed. Methods of how to incorporate range uncertainties into the plan optimisation and evaluation process is examined.

Chapter 3 A method has been suggested to quantify the inter-fraction range uncertainty in proton therapy by calculating range changes throughout treatment using daily volumetric imaging. The process of creating a calibration curve of HU to relative proton stopping power for the TomoTherapy MVCT has been laid out and assumptions and limitations considered.

Chapter 4 Clinical patient data is used to measure random range uncertainty from inter-fraction motion for a sample of patients and two treatment sites. This includes analysis of individual patient data and of the samples as a whole. This information may be used within plan optimisation or evaluation, or both.

Chapter 5 A method to introduce robustness analysis into plan evaluation is presented. In particular, a method to define a site-specific, and centre-specific, robustness database by retrospectively analysing clinical IMPT plans is shown. Such a database could be used during the plan evaluation and during the plan calculation phase to aid the planner to select the optimal plan.

Chapter 6 Discussions

Chapter 2

Uncertainties in Proton Therapy

2.1 Uncertainties in Proton Planning

Sources of uncertainty present in conventional radiotherapy also apply to proton therapy. Most geometrical uncertainties can be managed in the same way, including variation in delineation, set-up uncertainties, imaging inaccuracies and patient motion. However, there exists an important and fundamental difference in proton therapy, namely the proton range. Protons have a finite range highly dependent on the electron density of the material they are traversing, resulting in a steep dose gradient at the distal edge of the Bragg peak. Positioning of these dose gradients is critical to successful planning and treatment. Therefore, an uncertainty of even a few millimetres can lead to under-dosage in the target volume or over-dosage of an organ at risk (OAR).

Several authors have addressed the problem of range uncertainties in proton therapy, and the purpose of this section is to analyse their conclusions. Understanding the causes and magnitude of range uncertainties and incorporating them into the planning process is essential for optimised proton planning.

2.1.1 Sources of Range Uncertainty

The main factors leading to range uncertainty are shown in (Figure 2.1). Because the main advantage of using protons in cancer treatment is their finite range, this advantage can be fully exploited only if the proton range in the patient can be precisely predicted (*Lomax, 2008a*). It has been suggested that range uncertainties can be between 1 and 15mm for lung tumours (*España and Paganetti, 2010*), but larger changes are possible owing to anatomical

changes in the patient (e.g. weight loss or gain and differential filling of anatomical cavities). Uncertainties are normally compensated for in conventional radiotherapy by introducing safety margins around the treatment volume and around OARs to produce a planning target volume (PTV) and planning OAR volume (PRV), as recommended by the ICRU Reports 50, 62 and 83 (*ICRU 50*, 1993; *ICRU 62*, 1999; *ICRU 83*, 2010). A similar method has been recommended by the ICRU for protons (*ICRU 78*, 2007). The larger the safety margin, the less conformal the resulting dose distribution. Therefore, to achieve an optimum proton treatment plan, the range prediction needs to be as accurate as possible.

The variables that give rise to uncertainties in the range prediction (Figure 2.1) can be divided into two main groups: those causing uncertainties in the range calculation in the treatment planning system (TPS), and those leading to discrepancies between planned dose and delivered dose.

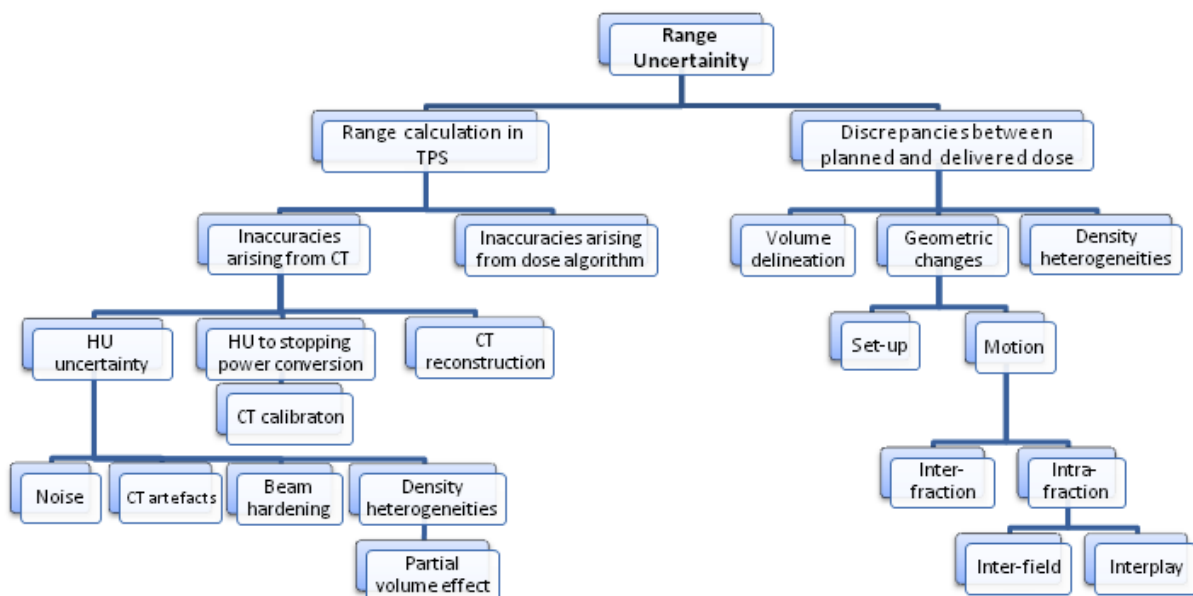


Fig. 2.1 Schematic of sources of range uncertainties in proton therapy

2.1.2 Range Calculation Uncertainties in the Treatment Planning System

Inaccuracies Arising from the Planning CT

With respect to range calculation uncertainties, these can arise from inaccurate data exported to the TPS. CT is used to acquire patient image data and the Hounsfield units (HUs) are then converted into proton-stopping powers so dose calculations can be made. Uncertainties arise in proton range calculation from CT-based plans owing to inaccuracy in the HU to proton stopping power conversion and inaccuracies in the HU values themselves (*Chvetsov and Paige, 2010*). Inaccuracies in the HU values are caused by noise, CT artefacts and beam hardening.

Schaffner and Pedroni (1998) and *España and Paganetti (2010)* investigated how the conversion of HUs to stopping power affects the range calculation in comparison with the real treatment range. *España and Paganetti (2010)* tested different conversion methods, including the traditional stoichiometric calibration method. Positron emission therapy (PET) imaging was used to determine the range of the proton beam in a phantom and compare it with the calculated range. It was noted that the back-to-back photons imaged with PET are generated from electron–positron annihilations caused by inelastic nuclear interactions between protons and target nuclei and not from atomic interactions, which primarily leads to dose deposition. *España and Paganetti (2010)* and *Schaffner and Pedroni (1998)* both concluded the same result: that the uncertainty caused by conversion was, $\pm 1\%$. There is research being undertaken into the development of proton CT. This would remove the uncertainty associated with the conversion from HUs to proton stopping powers (*Schulte et al., 2004*).

Noise is a stochastic uncertainty that either adds or subtracts from the HU value; this type of uncertainty is important only if the proton beam is sensitive enough to be affected by these changes in HU value. It was concluded that uncertainties caused by noise have a similar contribution to conversion uncertainties $\pm 1\%$ (*Schaffner and Pedroni, 1998*). Beam hardening had a greater effect on the assigned HU value. This was dependent on the position and density of the tissue and added uncertainties of the order of $\pm 1.8\%$ and $\pm 1.1\%$ for bone and soft tissue, respectively (*Schaffner and Pedroni, 1998*).

It is essential for CT-scanner-specific calibrations to be carried out (*ICRU 78, 2007; Schaffner and Pedroni, 1998*). This is because, even though proton stopping power is independent of

the imaging X-ray energy and the position of the target, HUs are dependent on the X-ray spectrum and target position. Each scanner will produce a different X-ray spectrum generated with a different tube potential and current, therefore requiring individual calibration. *Moyers et al.* (2010) carried out the measurement of the relative linear stopping powers of 21 different tissue substitutes. These were then scanned using both kilo-voltage and mega-voltage CT and the relationship between stopping power and HU value was determined.

Lomax (2008b) has described how the combined effects of the proton's sharp distal fall-off, finite range and multiple Coulomb scattering can have an impact on the sensitivity of plans to density heterogeneities in the patient. At the Paul Scherrer Institute in Switzerland the CT scanner has been stoichiometrically calibrated to have an accuracy of 1% for soft tissue and 2% for bony tissue, but, owing to inherent uncertainties such as beam hardening, reconstruction artefacts and reconstruction algorithms (*Lomax*, 2008b), it has been stated that an uncertainty in HU value of 3% is more realistic. To investigate the effect of this uncertainty, each plan was recalculated with the HU value increased and decreased by 3% to simulate an undershoot and overshoot scenario. The results were obtained for a simple prostate case and a skull base case. The distal-edge tracking (DET) approach was found to incur a systematic over- and under-dosage of the clinical treatment volume (CTV) of 5% when a $\pm 3\%$ HU uncertainty was introduced, whereas the 3D IMPT dose-volume histogram (DVH) for the nominal, under- and overshoot plans showed little difference suggesting DET is less robust than 3D IMPT.

Inaccuracies arising from the Dose Calculation Algorithm

Lomax (2008a) investigated the limitations in analytical dose calculations and the effects of uncertainties in density calculation from CT data in DET and 3D IMPT dose distributions. To investigate uncertainties arising from using an analytical dose calculation algorithm the dose distributions for Version 1 and Version 2 DET and 3D IMPT skull base plans were compared with the same plans calculated using Monte Carlo models (Version 1 plans use less stringent constraints on OARs than Version 2 plans, therefore, target coverage has a greater priority in the optimisation in Version 1 plans). In contrast to using an analytical mathematical algorithm to calculate dose distributions, Monte Carlo models use a probability distribution to model interactions and the production of secondary particles in a medium for a given energy. For the skull base case the two calculation methods were in close agreement for an acceptance level of $\pm 10\%$, but decreased for lower acceptance levels. At all acceptance levels, 3D IMPT plans showed better agreement in the PTV than DET plans,

with 87% of points in the 3D IMPT plan agreeing to within $\pm 3\%$ and only 80% of points agreeing to within $\pm 3\%$ in the DET plan for Version 1 plans. However, for the Version 2 plans, agreement falls to 77% and 70% for 3D IMPT and DET, respectively. In the OARs it was found that the Monte Carlo calculation predicted smaller doses in the optic nerve and brain stem than the analytical calculation, especially in the Version 2 plans. The trend showed that for both cases 3D IMPT showed smaller differences than the DET plans. It was concluded that DET was relatively sensitive to calculation uncertainties; in comparison, 3D IMPT was more robust with respect to both types of uncertainty.

In planning with photons there is a wealth of experience in prescribing doses to PTVs and dose constraints to OARs. This has meant that when planning with protons there was a need to prescribe doses relative to those used previously with photons by applying the concept of radiobiological equivalent dose, Gy(RBE). ICRU report 78 (*ICRU 78*, 2007) offers a method for dealing with the Relative Biological Effectiveness (RBE) of protons when it comes to determining the best estimate of RBE to be used in any calculation relating proton and x-ray doses. A generic RBE value for protons for all therapeutic energies (60-250 MeV) of 1.10 is used. This value is derived from RBE values for a variety of in vivo systems using animal tissues and organs. 1.10 is the mean value for all proton energies, dose levels and tissue systems (*ICRU 78*, 2007). There is, however, a related range uncertainty owing to the RBE of proton beams, which is beyond the scope of this thesis. For more information on RBE the reader is referred to the literature (*Carabe et al.*, 2012; *Grassberger et al.*, 2011; *Matsuura et al.*, 2010; *Robertson et al.*, 1975).

2.1.3 Discrepancies Between Planned Dose and Delivered Dose

Despite algorithms being able to calculate range in the presence of density heterogeneities, range uncertainties can be introduced by geometric changes in the position of density heterogeneities relative to the proton beam by set-up uncertainties and patient motion (*Deasy*, 1998).

Motion

In many treatment sites, organ motion has to be considered and incorporated into the planning and delivery workflow. Organ motion includes inter-fraction motion (between each fraction) and intra-fraction motion (during the treatment delivery). Patient motion influences the position of the inter-fractionally moving organ and intervention in the form of immobilisation and image guidance for precise bony or soft tissue anatomy setup at the be-

ginning of each fraction is required to optimise treatment delivery and minimise CTV to PTV margins. These are well-established techniques in radiotherapy (*Burnet et al.*, 2010).

Intra-fraction motion includes both inter-field (i.e. between each field) and intra-field (i.e. during the field) motion. Intra-fraction motion changes during the delivery over the time period of seconds and minutes and includes anatomical changes such as bowel movements, respiration and heartbeats. Studies have been carried out to determine the magnitude of inter- and intra-fraction motion at different tumour sites (*Booth and Zavgorodni*, 1999; *Lan-gen and Jones*, 2001; *Rimmer et al.*, 2008).

With proton therapy, geometric changes caused by motion can also result in density changes, and therefore a change in radiological path length, along the beam path. In X-ray therapy, the dose distribution changes by only a few per cent, owing to density changes. However, their influence in proton therapy can result in severe under-dosage of the CTV and over-dosage of OARs and normal tissues distal to the target (*Lambert et al.*, 2005). This effect is the same for both scattering and scanning delivery techniques. In addition, for active scanning, the major effect of intra-field motion is *interplay*, which relates to motion, usually respiratory motion, with a frequency similar to that of the scanned beam, and which can lead to over- and under-dosage in the target volume (*Knopf et al.*, 2011; *Phillips et al.*, 1992; *Seco et al.*, 2009; *Zenklusen et al.*, 2010).

Lomax (2008a) investigated the effects of inter-fraction, intra-fraction and inter-field motion for both 3D and DET IMPT treatment plans. It was reported that, for a 5mm shift in the dose distribution, an under-dosage of up to 20% can occur in the CTV when plan optimisation for maximum OAR sparing is used. Treatment deliveries involving high dose gradients that rely on matching contributing fields are very sensitive to any changes in position between deliveries of each field. An important conclusion from this paper is that for certain IMPT plans a simple PTV margin cannot be applied to compensate for inter-fraction motion. Further investigation into the management of uncertainties and more assessment for IMPT treatments at the treatment planning level are needed. *Lomax* (2008a) also described the greater sensitivity protons have to density heterogeneities owing to their physical characteristics and that these could accentuate motion uncertainties. Without a PTV, there is no method for recording dose to a moving CTV or for evaluating plans through the use of DVH's and for IMPT plans, no other compensation method to ensure that the CTV is covered. After comparing the effects of geometrical and density heterogeneities for both DET and 3D IMPT it was found that DET plans are very sensitive to motion uncertainties and considerable changes in

the dose distribution were found. The reasoning behind this is that internal dose gradients in the individual fields in DET can cause large variations in dose within the target volume when mismatched. This was observed for inter-field motions, but would also be an issue when intra-field motions were present.

Simulations have also been carried out by *Lambert et al.* (2005), albeit only in homogeneous geometries, to investigate how interplay affects the dose distribution in the CTV. Lambert et al took the ICRU 50 (*ICRU 50*, 1993) recommendations for PTV dose homogeneity of 95–107% as threshold. Their results showed that in extreme cases up to 100% of the target volume received doses below that recommended by ICRU 50 and with a minimum dose as low as 34% of the prescribed dose. These results were backed up by simulations carried out by *Grözinger et al.* (2006) and experimental work by *Bert et al.* (2008). *Bert et al.* (2008) carried out the first patient simulation that confirmed under-dosage using four-dimensional computed tomograph (4DCT) lung data. Despite using margins that consider the effect of the changing radiobiological path length, adequate CTV coverage could not be achieved.

2.2 Managing Uncertainties Including Positional Discrepancies and Motion

The management of uncertainties is critical to successful radiotherapy. Current methods of reducing geometric uncertainties include immobilisation, in-room imaging, image guidance, planning from 4D CT and gated radiotherapy for respiratory motion. These are all methods that are routine in X-ray therapy and are now being applied to proton therapy (*Bert and Durante*, 2011).

2.2.1 Motion Mitigation

Two main methods of motion mitigation have been developed for active scanning to mitigate the effects of interplay: rescanning (repainting) and beam tracking (*Bert and Durante*, 2011).

Rescanning

Typically in proton therapy, multiple dose *painting* is required to deliver the prescribed dose distribution to each layer of the target volume. In IMPT the dose is delivered using multiple

field directions and with a range of different proton energies to produce a uniform dose distribution throughout the target volume. To increase dose conformity, steep dose gradients are used at the target border and field edges. This increases the complexity of the fluence maps per field and therefore makes the plan less robust to uncertainties. Intra-fraction motion can lead to an under and overdose pattern that is dependent on the motion parameters (initial phase, period and amplitude) and the speed of the scanning process or direction of scanning. By rescanning the PTV several times per treatment fraction an averaging effect of the over- and under-dose pattern can be achieved. As long as the intra-fraction motion changes between each rescan, so that there is no synchronisation between delivery and organ motion, a homogeneous dose distribution to the CTV can be achieved with a “blurred” dose distribution in the region of the margins (*Bert and Durante, 2011*). There are two main types of rescanning:

- rescanning by energy slice, also known as slice-by-slice, level painting or non-volumetric rescanning.
- rescanning of volume, also known as volumetric rescanning or uniform repainting.

The problem of organ motion and rescanning synchronism has also been tackled by several groups, including *Furukawa et al. (2007)* and *Seco et al. (2009)*. Solutions include:

- using random modulations *e.g.* a change in scan speed
- repainting energy slices in different orders (random repainting)
- random delays between repaints (time delay)
- change in scan paths between two rescans
- use of data from motion monitoring systems in combination with modulation dose rate, either as phase-controlled rescanning or as breath-sampled rescanning.

Data from phase-controlled rescanning and breath sampled rescanning show that uniform spreading of rescans over the motion of the breathing cycle leads to more robust treatment delivery, requiring fewer rescans than the other methods for the same level of homogeneity in the CTV. There are also two methods of delivering rescanned treatments (*Zenklusen et al., 2010*):

- Scaled rescanning – this is delivering each rescan with a proportionally reduced dose per scan and is the most typical method.

- Isolayered rescanning – where a specified number of protons per spot are delivered at each scan, which leads to a different spot position in each rescans. This is because some spots will have received sufficient dose from previously completed scans.

Beam Tracking

In beam tracking the motion of the CTV is monitored and compensated for so that a PTV margin is reduced (*Bert and Durante, 2011*). Owing to the need to compensate for both CTV motion and the change in radiological path length in proton therapy, the German national heavy-ion physics laboratory, the Gesellschaft für Schwerionen, in Darmstadt, has established a method of using a motor-driven compensation system for changes in radiological path-length (*Bert et al., 2007; Saito et al., 2009*) and raster scanning (*Furukawa et al., 2007*).

2.2.2 Margins

The widely used CTV–PTV margin recipe, derived by *van Herk (2004)*, is used to ensure that 90% of patients have CTV coverage of at least 95% of the prescribed dose. The static PTV represents the moving CTV and is therefore a useful method of evaluating a plan, by using DVHs to report the minimum dose to the CTV. In proton therapy, if conventional PTV margins do not produce plans robust to uncertainties, another method of ensuring confidence in a planned dose distribution representing the delivered dose distribution is required. This can be achieved by increasing margins or by *smearing* the proton range with a compensator in the case of passive scattering. However, this will lead to a reduction in dose conformity in the plan. The concept of a safety margin also partly fails for set-up uncertainties because they not only shift the dose distribution but also change the range where there are density changes in the beam path, leading to a distorted dose distribution (*Grözinger et al., 2008*). In proton therapy, any concept used to compensate for organ motion-generated uncertainties must include both geometric motion and the influence it has on the beam range, as this can have a severe dosimetric impact (*Grözinger et al., 2008*).

PTV margin sizes in proton therapy have been investigated by *Thomas (2006)*. In many comparative studies of achievable dose distributions between protons and X-rays, the CTV and PTV margin sizes are the same for both modalities. The CTV and OAR volumes are the same for any treatment modality. However, the size of the margin between CTV to PTV and OAR to PRV is modality dependant. *Thomas (2006)* quantified margins required for PTVs

and PRVs in proton therapy for anterior single, anterior–posterior parallel opposed and four-field brick proton beam arrangements. Each type of systematic and random uncertainty was considered and the effect they had in geometry and range was discussed, as was the modality dependency. The key message is that isodoses defined by lateral edges, for instance, can be treated in the same way as for X-rays, whereas isodoses defined by the distal edge will have a different uncertainty arising from inaccurate electron densities derived from CT data. Margins were calculated for a head and neck (H&N) and a prostate case. For the H&N case the CTV–PTV margins in all three planes for the single field and parallel opposed fields were smaller than those required by X-rays; however, they were greater for the four-field brick plan. This same pattern was observed for the prostate case. This is because a smaller margin size is needed in the anterior–posterior direction for single and parallel opposed (3mm compared with 10.5mm for the H&N case), as set-up uncertainties and motion in this direction will not affect the dose distribution. Beam specific margins were further explored by *Rietzel and Bert (2010)* and *Park et al. (2012)*. *Park et al. (2012)* showed a method of creating beam specific PTV margins by ray-tracing and shifting ray lines to account for tissue misalignment. They found that plans created using them provided better coverage in the presence of setup and range uncertainties.

Albertini et al. (2011b) addressed the issue of whether safety margins in proton planning are necessary. In this paper two types of treatment delivery were investigated: single field uniform dose (SFUD) plans and IMPT plans. Plans included:

- (i) 3 field SFUD plan to the PTV.
- (ii) 2 field IMPT plan delivering uniform fields to the PTV.
- (iii) 4 field Non-uniform field IMPT plan, with strict constraints on OARs, planned to the PTV.
- (iv) Non-uniform field IMPT plan, with strict constraints on OARs, planned to the CTV.

The robustness of each plan to random set-up and systematic range uncertainties was compared. Robustness was determined using the concept of *error-bar dose distributions*, by shifting dose distributions relative to the expected uncertainties and then displaying a final *error-bar* dose distribution and *error-bar* volume histogram; therefore, it was representative of the possible discrepancies in dose between planning and delivery. The results from this work show that, for uniform field deliveries [(i) and (ii)], the use of margins improved the plan robustness, where <5% of the CTV contained dose uncertainties >10%. However, in highly complex non-uniform IMPT plans [(iii) and (iv)], margins improved robustness only

slightly. For 5% of the CTV, uncertainties of up to 55% were observed. For plans (iii) and (iv), steep dose gradients existed within the target, leading to uncertainties within the target. Because margins can help CTV coverage only at the edges of the target volume and not in the centre, they have little effect on plan robustness when steep dose gradients exist within the target volume (*Albertini et al.*, 2011b). Interestingly, it was found that complex IMPT plans were robust to OARs. It was concluded that there is a need for more sophisticated methods for taking into account uncertainties in highly modulated IMPT plans, such as including them in the optimisation. This work assumed that the set-up uncertainty was indeed random and considered only the systematic component of the range uncertainty. It did not include the effect on the dose distribution from motion uncertainties.

2.2.3 Probabilistic Planning and Robust Optimisation

An alternative to using margins is being developed by incorporating uncertainties directly into the optimisation algorithm, as proposed by *Unkelbach et al.* (2007) and *Pflugfelder* (2008) to achieve a high quality plan with a high probability of being deliverable (*Chu*, 2006). Due to the number of spots in 3D IMPT required to fill the target an optimisation algorithm is required to determine the optimal solution for their individual weights. Intensity modulation optimisation is highly degenerate (*Albertini*, 2011; *Webb*, 2003). There exist many dosimetrically equivalent solutions to the given problem of delivering a homogenous dose to the target whilst ensuring the dose to OARs are within predefined constraints. Some of these solutions may offer greater plan robustness and therefore a greater chance of cure whilst limiting the chance of normal tissue complications. This “degeneracy” of solutions can be used to reduce the sensitivity of the plan to uncertainties if they are incorporated into the optimisation process (*Pflugfelder*, 2008).

Probabilistic planning assumes prior knowledge of the probability distribution of the uncertainty; in most cases, the distribution was assumed to be normal. The probabilistic approach works on the principle that the total delivered dose to a voxel is random due to its dependency on both the dose delivered at each fraction and the location of the voxel during that fraction (*Chu*, 2006). It can be assumed that the total dose to a voxel is the sum of the N random variables, where N is the number of fractions. The total dose can therefore be approximated as a Gaussian distribution by following the central limit theorem. An approximation can be made then that the N random variables, which give the dose per fraction, are independently and identically distributed (*Chu*, 2006). The use of this approximation allows for the solution to be less computationally expensive by computing the mean and variance of

the dose from a single fraction to form a probability distribution (*Chu, 2006*). However, this approximation relies on the assumption that patient changes over time, for example weight gain or loss, or ‘relaxation creep’, are negligible to the uncertainty problem. To address this *Bangert et al. (2013)* use a method of analytical probabilistic modelling (APM) to include complex correlation models of the underlying uncertainties. Robust optimisation effectively optimises the worst case that may occur, assuming that the proton range may vary within some known interval (*Unkelbach et al., 2007*). An example of a robust optimisation algorithm is the worst-case dose distribution introduced by *Lomax et al. (2004)* and is a method of combining multiple dose distributions into a single one. Uncertainties can be applied to the CT data, for example a percentage change in HU or several isocentric shifts, and the dose calculated. For a voxel inside the target volume the minimum dose to this voxel is stored and for a voxel outside of the target volume the maximum dose is stored. Minimising these values results in the optimal worst-case plan. Each voxel is treated independently so the worst-case dose distribution is an “unphysical” one. Although the worst-case dose distribution is unphysical it can be used as a lower bound for the worst quality treatment plan. A best-case plan can be seen as the upper bound in the same respect, but to the best achievable plan quality. In this optimisation it is assumed that the range uncertainties for each Bragg peak are correlated, so that at the target the range uncertainty is accumulated and effects within the target are ignored. Both methods, probabilistic and robust planning, produce plans less sensitive to uncertainties, and mathematically each approach yields similar results as shown by (*Chu, 2006*).

Unkelbach et al. (2007) investigated how incorporating uncertainties into the IMPT optimisation yields qualitatively different treatment plans compared to conventional plans which do not account for uncertainty. Both probabilistic and robust methods were used to include uncertainties into the plan optimisation to allow for a comparison to be made. The dose from each beamlet was calculated at multiple ranges; three ranges between 2 and 5mm were used, and these were the nominal, maximum and minimum range uncertainties (*Lomax et al., 2004*). The set-up uncertainty was modelled as a shift of the target inside a sphere with a radius equal to the maximum setup uncertainty. Both approaches yielded similar results and both fell into a multi-criteria problem - that plans had greater robustness to uncertainties, but at a cost to conformality. They concluded that both methods led to treatment plans that were less sensitive to range variations and that both plans were of a similar quality. This was achieved by using the lateral edge instead of the distal edge to shape the dose distribution at the transition between the OAR and the tumour for both methods.

Pflugfelder (2008) applied the worst-case optimisation method to real patient data where the target surrounded the spinal cord. Uncertainties of the beamlet ranges of $\pm 5\text{mm}$ were considered. The range uncertainty was sampled at three positions: the nominal range, the maximum range and the minimum range. Using this optimisation process, the plan's sensitivity to range uncertainties was decreased. However, this was achieved by compromising the dosimetric quality of the plan by:

- (i) using the lateral instead of the distal edges of the Bragg peaks to shape the dose gradients between the target and the OAR
- (ii) adding a *safety margin* automatically at the distal field edge for each treatment beam
- (iii) flattening the dose profile in depth for each treatment beam compared with the nominal plan

For the tumour, the largest deviations between delivered and prescribed doses corresponded to an under-dosage close to the OAR, whereas the deviations in most other parts of the tumour were small. The maximum doses delivered to OAR voxels reached approximately 80% of the prescribed dose (*Pflugfelder*, 2008). The DVHs from each method showed very similar results. *Pflugfelder* (2008) showed comparable results to those of *Unkelbach et al.* (2007) using their worst-case optimisation function (*Pflugfelder*, 2008). When using the worst-case optimisation incorporating both setup and range uncertainties, the resulting change to the dose distribution was such that the distal dose gradient of the treatment beam was smoothed.

Chen et al. (2012) introduced a method of including robustness into a multi-criteria optimisation (MCO) framework for IMPT. The concept of multi-objective Pareto optimisation (often known MCO) has been introduced into radiotherapy treatment planning to overcome these problems (*Cotrutz et al.*, 2001). A Pareto optimal treatment plan is not a single plan but a database of plans where each one represents a Pareto optimal solution which cannot be improved without worsening at least one other parameter (*Thieke et al.*, 2007). In this case the planner can navigate through the pre-calculated database of Pareto optimal plans and visualise in real time the trade-offs for each case (*Craft et al.*, 2005). MCO allows for the plan which strikes the best balance between different objectives to be selected from a Pareto front.

Chen et al. (2012) suggested that the trade-off between robustness and dosimetric quality in IMPT can be investigated using MCO. An example is shown in Figure 2.2. A planning

objective for robustness represents the worst case realised for any uncertainty scenario and so can provide a measure of plan robustness. The MCO method used by this group was based on a linear projection solver using *minimax* optimisation, meaning that the objective was minimised for the worst-case uncertainty scenario and was used to investigate plan robustness to uncertainties. The computing time required for the robustness optimisation for each Pareto optimal plan was 5 minutes. Range uncertainties were modelled using an overshoot and undershoot scenario of $\pm 3\%$ (as used by *Lomax (2008b)*). The set-up uncertainty was modelled using discrete rigid shifts of the patient with respect to the isocentre. A base of skull tumour was planned twice: once using robust optimisation (but without MCO) and once with margins. A chordoma case was planned with MCO as an ideal example of the trade-off between brain stem sparing, CTV coverage and robustness. In the skull base case the DVH of the CTV for both the robust plan and the margin plan showed similar coverage for the nominal plan. However, once plans with uncertainties were introduced, the coverage was worse for the margin case. In consideration of brain stem sparing the robust plan ensured that in all uncertainty cases the dose was limited to 60Gy; this was not seen in the margin plan. In the chordoma case the Pareto surface of objectives allowed the planner to have greater control when deciding between a robust plan, a conformal plan or somewhere in between.

2.2.4 Treatment Analysis and Validation

For all areas in radiotherapy, validation and quality assurance are routinely carried and are a necessity for safe, effective treatment. Phantom work and technical assessment are carried out when a new technology or method is being implemented, such as motion mitigation techniques. However, patient-specific quality assurance is also required, and this starts at the decision to accept a given plan design. In cases where margins are in use, the PTV is used as a tool for reporting the minimum dose to the CTV. If the PTV method is to be discarded then a new method for recording dose to a moving CTV, and for evaluating plans through the use of DVHs, is needed. As discussed above, *Albertini et al. (2011a)* have devised a possible solution to this problem by determining plan robustness for set-up and range uncertainties using an error-bar dose distribution method. This method was later validated experimentally using a customised anthropomorphic phantom based on a diagnostic head phantom, and GafChromic H EBT2 batch F100070903B film, to carry out patient-specific quality assurance under realistic conditions and with deliberately introduced uncertainties. A large part of ensuring optimum treatment delivery to the patient is verifying the accuracy

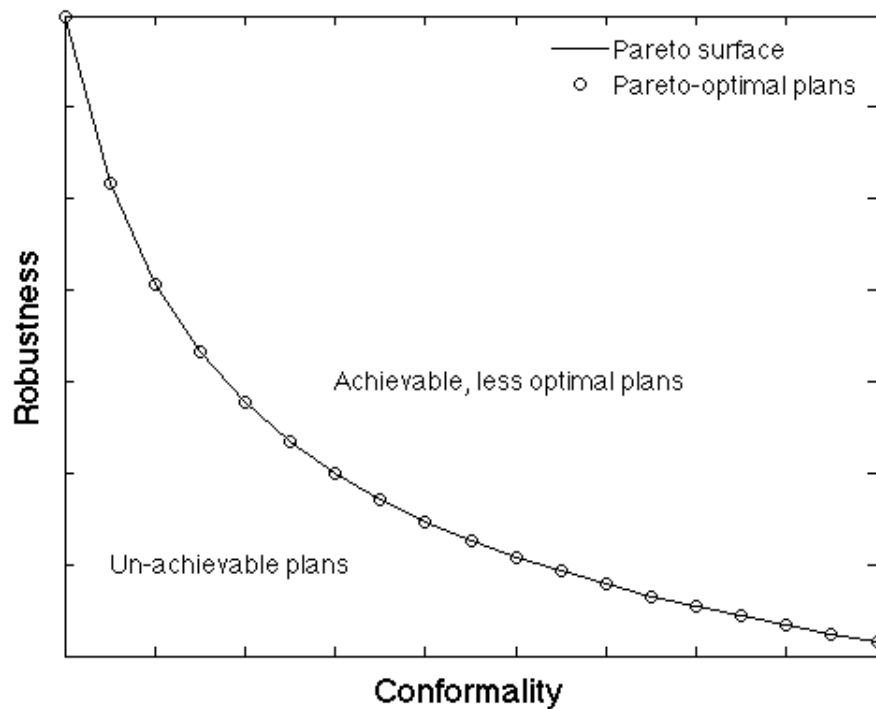


Fig. 2.2 Illustrating two parameters for optimisation, conformity and robustness, and how a Pareto front can be used to investigate clinically achievable plans with the same Pareto-optimised solution, but with different values of importance on robustness and conformity.

of the dose delivered and comparing it with that predicted by the planning system. In cases where uniform fields are being delivered it is enough to experimentally measure the individual field doses, and in the case of proton therapy, the dose in homogeneous water (*Albertini et al.*, 2011a).

The highly modulated nature of IMPT means that ever more complex methods of plan verification are being developed to cope with the advancing treatment technology to ensure safe patient treatment. *Safai et al.* (2004) described how a scintillation dosimetry system was used to verify such proton treatments. The problem with this method was that, even though it could accurately measure the dose delivered, the dose from the TPS needed to be recalculated in a homogeneous material to be compared with the measured results (*Albertini et al.*, 2011a). This approach of patient-specific plan verification is not adequate when fields of inhomogeneous dose distributions are being applied. Each inhomogeneous dose distribution will, in combination, achieve a uniform dose in the target volume, but any

slight misalignment of a steep dose gradient could lead to a severe under- or over-dosage in comparison with the plan (*Albertini et al.*, 2011a). This effect could be worsened by the presence of density heterogeneities in the patient (*Albertini et al.*, 2011a). By using the customised phantom, *Albertini et al.* (2011a) have been able to measure the accuracy of dose and the effect of spatial and range uncertainties by deliberately introducing uncertainties. Setup uncertainties were introduced by moving the phantom by known amounts, and range uncertainties simulated by modifying the HU values by $\pm 3\%$ (*Lomax*, 2008a). From this work it was found that 3D IMPT plans were more robust than DET plans. The theory is that there are fewer Bragg peaks used in DET, whereas in 3D IMPT more spots are used (about 180 for DET compared with about 1500 for 3D IMPT in the example used), each with a lower weighting than those in DET, so that any misalignments would have a greater impact on the DET plan.

2.3 Discussion

To produce optimal plans using protons, knowledge of the proton range in the patient is essential. There are many factors that can contribute to range uncertainty. HU uncertainties can contribute to approximately $\pm 3\%$ uncertainty in range even after site-specific CT scanner calibrations have been carried out. Owing to the steep dose gradients that can be achieved at the edges of, and within, the target volume, precise field matching is required to prevent over- or under-dosage in the target. Simulation and patient data examples have been used to show that the use of a PTV margin does not ensure uniform dose coverage to the CTV for complex IMPT plans. Despite these results, there is still a need for facility based and treatment protocol-specific simulations to be carried out to achieve quantitative assessments for different tumour sites (*Bert and Durante*, 2011). Parameters such as dose regime, scan path pattern and beam extraction rate need to be included because they will affect the resulting dose distribution.

Methods of improving plan robustness to range uncertainties beyond the use of margins are being developed for use in complex IMPT plans to ensure CTV coverage. However, all of these methods will decrease the achievable conformity of a plan. Robust optimisation using the worst-case scenario will produce a robust plan, but at the cost of sacrificing conformity by placing a lateral edge instead of the sharp distal edge to shape the dose between the target and the OAR. The use of robust MCO gives the planner greater control over objective weights. This is important because there is little evidence or known experience in

determining what type of plan, conformal or robust, is most beneficial for the population of patients.

The difficulty with deliberately introducing uncertainties into either the optimisation or the plan evaluation is that all probability distributions are assumed known. *Albertini et al.* (2011b) and *Chen et al.* (2012) only considered range uncertainties created in the range calculation arm in Figure 2.1. The assumption is then that any change in radiological path length caused by set-up discrepancies or motion, whether during a fraction or between fractions, has a negligible effect on the range. Motion uncertainties will be dependent on anatomical location and setup uncertainty will be protocol specific, based on what IGRT schedules are in place and the type of immobilisation used. More research is needed in quantifying range uncertainties for different anatomical locations so that they can be implemented into the robust optimisation of dose modelling. This would include investigating range uncertainties associated with different IGRT schemes and types of motion.

In the absence of a PTV, novel methods to evaluate dose coverage have been developed such as the error-bar DVH and the use of worst-case and best-case optimisation to give upper and lower bounds on a DVH. A challenge for all these methods will be how to carry out adequate and efficient patient-specific verification. The data available from non-patient heterogeneity studies have shown that rescanning techniques produce improved results compared with beam tracking, but further investigations using real patient data are required (*Bert and Durante*, 2011). There is no information in the literature regarding patient-specific validation for rescanning and beam tracking methods because they are not yet in routine clinical use. However, the group at PSI did publish the first experimental results of motion mitigation by discrete spot (*Schätti et al.*, 2013) and continuous line (*Schätti et al.*, 2014) rescanning in 2013 and 2014 respectively.

The question remains as to whether adaptive therapy can become an integral part of a proton therapy treatment, to allow re-optimisation during the course of a patient's treatment and if so how this can be achieved. Adaptive radiotherapy is the adjustment during the treatment course of the parameters initially chosen at planning, in order to re-optimize the treatment as a direct result of unavoidable changes in the patient. In proton therapy, the use of adaptive therapy may prove to be valuable for ensuring the delivered dose matches the planned dose at each fraction. In this context, access to high quality daily volumetric imaging, fast dose recalculation algorithms and computing power will be required. This may provide the opportunity for greater individualisation of the patient's treatment. Use of a multi-objective

Pareto optimisation function could allow plans to be recalculated when necessary using different weights for robustness and conformity, incorporating image guidance data to optimise the plan.

It has been shown that a PTV may not be the best solution for ensuring target coverage in the case of complex IMPT plans. This is the result of the sensitivity of the proton range to density heterogeneities and the achievable steep dose gradients inside the volume. Many groups have been working towards possible solutions for achieving dosimetric quality and plan evaluation without a PTV. The solutions described here show great promise for optimising proton therapy planning. Based on the literature discussed here the purpose for the following work in this thesis was determined. The following chapters explore the effect of start conditions on plan robustness and look to develop methods of plan robustness analysis, and to quantify range uncertainties for different anatomical locations due to patient motion.

Chapter 3

A Method for Quantifying Random Range Uncertainty

Techniques such as probabilistic planning, robust optimisation, and methods of simulating uncertainties to analyse plan robustness are becoming more widely used. For example these include, the worst case optimisation (*Lomax et al.*, 2004; *Pflugfelder*, 2008), used in a research capacity, and the RayStation TPS 4.5 which supports robust optimisation commercially for both photon and proton planning (*Raysearch Laboratory*, 2014). It is becoming evident that there is a need for a greater understanding of the magnitude and probability of range uncertainties for the population.

In this chapter a method for acquiring centre- and site-specific prior knowledge of random range uncertainties for the population is provided. In Chapter 4 patient examples are given.

3.1 Introduction

It has been previously established that there are many sources of uncertainty in proton therapy. These include both the systematic and random components arising from the uncertainty in HU, dose calculation algorithms, daily setup, target delineation and organ motion (see figure 2.1). Within conventional radiotherapy, IGRT provides information about the systematic uncertainty, allowing for this uncertainty to be corrected and for the possibility of reducing margins. Using IGRT online can allow for inter-fraction changes to be partly compensated for by applying rigid couch shifts before each fraction. The same technology is available in proton therapy. Though margins may not be an adequate way of providing CTV coverage (to a pre-designed probability) for complex proton plans, the same methods can be imple-

mented for calculating the prior information required as an input into the robust optimisation and for models designed to analyse plan robustness.

The range uncertainty problem may be relatively new to radiotherapy, but the uncertainty problem is not. Previously the ICRU recommendations for uniform prescribing and reporting (*ICRU 50*, 1993; *ICRU 62*, 1999; *ICRU 83*, 2010), as well as the margin recipes (*Stroom et al.*, 1999; *van Herk et al.*, 2000), came as a solution to solve the sensitivity of treatment plans to geometric uncertainties. The margins are grown based on known systematic and random uncertainties inserted into the recipe. In deriving his margin recipe, van Herk and colleagues (*van Herk et al.*, 2000) started from a well-defined probabilistic criterion; that the CTV-to-PTV margin should be grown to ensure the CTV minimum dose is greater than or equal to the planned PTV minimum dose, for 90% of patient treatments (*van Herk et al.*, 2000). The limitations of the PTV in complex proton cases have been discussed and several authors (*Chen et al.*, 2012; *Fredriksson et al.*, 2011; *Liu et al.*, 2012; *Pflugfelder*, 2008; *Unkelbach et al.*, 2007) have addressed this head on by developing probabilistic and robust optimisation algorithms for use in radiotherapy. To clarify, the probabilistic approach considers all possible range variation scenarios as a term in the objective function by weighting each with its probability of occurring. This is represented by optimizing the expected value of the objective function. The robust approach does not perform a weighting of each different scenario, but instead minimises the maximum deviation of delivered and prescribed dose, which can occur for all allowable ranges (*Unkelbach et al.*, 2007). Through using these methods, the treatment planner is no longer responsible for adding margins. Instead, the TPS builds its own “margins” into the dose distribution, governed by probabilistic planning criteria or a lower boundary with a predefined probability of occurring. (*Gordon et al.*, 2010). These approaches appear to be the correct way to deal with uncertainties when planning complex proton therapy treatments and it should be noted that treatment plans obtained by the probabilistic or robust methods cannot be reproduced by a safety margin approach (*Unkelbach et al.*, 2007).

Though finding, potentially, a limited place for PTVs in complex proton therapy the quantification of range uncertainties is required as input into robust optimisation (*Gordon et al.*, 2010; *Unkelbach et al.*, 2007). It has been shown how systematic setup uncertainties can be measured for each centre and site as described by Bolsi and colleagues (*Bolsi et al.*, 2008), but there is still a challenge in quantifying the random range uncertainty, and the associated probability arising from patient motion. In most cases robust optimisation and probabilistic

planning approaches had been modelled relying on rigid isocentric shifts in CT data sets or from uniform percentage changes in HUs. In Unkelbach's paper (*Unkelbach et al., 2007*) values of $\pm 5\text{mm}$ and $\pm 2.5\text{mm}$ were used to represent the systematic range and setup uncertainties respectively, random errors were not taken into account. These assumptions on the amount of range uncertainty are due to the lack of measured data to support more sophisticated models (*Unkelbach et al., 2007*). *Unkelbach et al. (2007)* suggested that for future studies tighter bounds on the actual magnitude of range uncertainty could be added with the aim to derive more precise uncertainty models for specific tumour sites and planning protocols. Gordon and colleagues (*Gordon et al., 2010*) suggest estimates could be obtained from a population of patients or, in adaptive therapy, from patient-specific data. PTV-based and probabilistic/robust plans are equally dependent on sufficiently accurate knowledge of the distribution of the geometric uncertainty (*Gordon et al., 2010*). In proton therapy this statement is equally true of the range uncertainty. In both conventional radiotherapy and in proton therapy, if the uncertainty distribution model is inaccurate, both types of plan, whether PTV or probabilistic, will produce underdosing of the target and/or overdosing of OAR(*Gordon et al., 2010*).

In this work the focus is on determining the random range error from inter-fraction motion after online IGRT based corrections have been applied. The clinical Mega-Voltage Computed Tomography (MVCT) data has been used offline along with the shifts recorded by TomoTherapy for each fraction to provide the relevant information. Using the shifted 3D MVCT data and structure sets (outlined by the doctor at planning) the Water Equivalent Path-Length (WEPL) within the CTV can be calculated. By taking the difference in WEPL between the first and consecutive fractions an indication of inter-fraction range uncertainty for a given set of beam directions can be obtained. When carried out for a large sample of patients an indication of the population probability distribution of WEPL changes that occur between fractions may be gained. This information would be specific to the anatomical location, immobilisation and method of IGRT. Using this method, probability distributions can be generated and used in either the robust optimisation or at plan analysis, or in both. By calculating this information online, action levels for carrying out dose difference analysis can be established allowing for adaptive planning.

3.2 TomoTherapy

TomoTherapy, shown in Figure 3.1 is an integrated helical IMRT and IGRT system consisting of a compact in-line 6MV accelerator mounted on a CT ring gantry with a detector array (xenon gas ion chamber) opposite. It provides volumetric, fan-beam megavoltage (MV) CT imaging on the treatment couch (*Langen et al., 2005*). Since 2007 at Addenbrooke's Hospital patients have been imaged daily on TomoTherapy using MVCT with rigid couch shifts and roll applied to correct for set-up and inter- fraction motion.



Fig. 3.1 TomoTherapy at Addenbrooke's. Provides daily imaging with positional correction on all patients (*Burnet et al., 2010*).

3.3 Calculating WEPL Changes in the CTV from TomoTherapy Shift & MVCT Data

In proton therapy it is essential for dose calculation that accurate conversion of HU to relative proton stopping power is carried out. In this work proton dose will not be calculated, yet it will still be required to establish the relationship between the CT data and the water-equivalent path length for protons to account for density variations between fractions. The method used to determine this relationship between HU and relative proton stopping power is explained so that WEPL calculations may be made from clinical TomoTherapy MVCT data.

The WEPL of each pixel in the beam direction is calculated using an effective depth algorithm. This means that high density pixels will have a larger path-length than that for water and low density pixels will have a shorter path-length. Therefore, confidence in the conversion between HU and proton stopping power is required. In this way the trajectory of a proton through the CT is transformed from the CT system into a water-equivalent system in the beam's-eye view. This then transforms the original target volume shape into a distorted one in the water-equivalent system. Figure 3.2 is an example to illustrate the process in a prostate MVCT scan. A 90° beam direction was used when converting from CT system (right image) to the water equivalent one (left image). The orange area in this image is the mask used to represent the prostate.

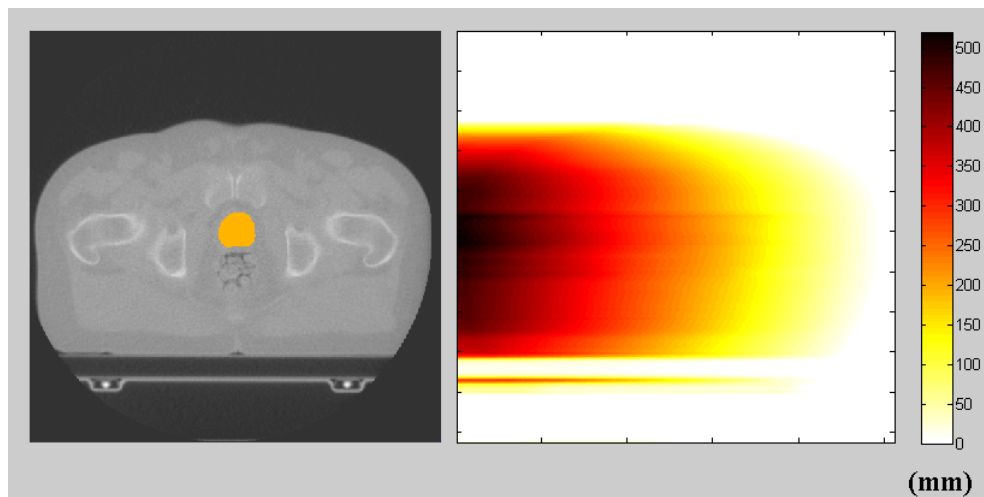


Fig. 3.2 Example of how CT data (left image) can be converted into WEPL (right image) at a beam angle of 90° using calibration curves and ray-tracing

There is no direct functional dependence between HU and WEPL. The HUs reflect the attenuation of X-rays, mainly by the Compton scattering, whereas ion energy loss processes dominate the proton path length. The actual chemical composition of the material (or tissue) affects both quantities, but with a different functional dependence on the Atomic number, Z , of the contributing atoms. Hence the desired relation cannot be retrieved from the knowledge of the HU alone. Until work investigating proton tomography (*Schulte et al.*, 2004) is complete the option left is to carry out CT-scanner and site-specific CT calibration.

A Quick Note on Stopping Power

Charged particles interact primarily by ionisation and excitation and deposit dose directly. These interactions are mediated by the Coulomb force between the electric fields of the incoming proton and the orbital electrons and nuclei of atoms in the medium (Khan, 2010). Collisions between the proton and orbital electrons result in excitation and ionisation of the atom by raising an electron to a higher shell or, if provided with sufficient energy, the electron will leave the atom. If this happens the electron may have sufficient kinetic energy to go on to cause further ionisations. These electrons are known as δ rays which are responsible for the microscopic structure of energy deposition around the primary track. Atomic interactions occur so frequently that energy loss appears continuous. The rate of loss of energy per travelled distance for charged particles is known as stopping power (S), which is the change in energy with distance, $S = \frac{dE}{dx}$. However, this equation does not hold unless we assume that all the dose is deposited at the site of interaction and ignore dose carried away by δ rays. The stopping power is proportional to the square of the particle's charge and inversely proportional to the square of its velocity, $\frac{q^2}{v^2}$ (Khan, 2010). As the proton slows down, the rate of energy loss increases and therefore so does the amount of dose deposited. The dose increases until near the proton range where it rises steeply at the Bragg peak before falling steeply to zero. This is described using the Bethe-Bloch formula (equation 3.1), which can be used to determine the mean range of the particle. As defined in ICRU 78 (2007) the distal fall off is the distance in gcm^{-1} in which the dose decreases from 80% to 20% of the maximum value when measured along the central axis in water. The range is defined as the depth in gcm^{-1} along the the beam central axis in water to the distal 90% point of the maximum dose value. There is also a mass stopping power, $\frac{S}{\rho}$, known as total stopping power and is expressed in $MeVcm^2g^{-1}$ which takes into account the mass density of the medium and includes energy losses from both collisional and nuclear interactions.

Calibrating CT Scanners

There exists a significant source of uncertainty in the HU conversion arising from the use of tissue substitutes, that have different chemical compositions to that of real tissue, to calibrate scanners. This leads to different values of electron density as the oxygen, carbon, hydrogen and calcium contents of these substitutes are changed to allow them to be usable often for radiobiological purposes (Schneider *et al.*, 1996). To address this challenge, many centres, including PSI in Switzerland and Orsay in France, have adopted a method of stoichiometric

calibration as described by *Schneider et al.* (1996) to calibrate their CT scanners.

In a stoichiometric calibration both real tissue and tissue substitutes are used to predict the HUs for human tissues (*Schneider et al.*, 1996). *Schneider et al.* (1996) verified this method of calibration for protons using a sheep's head and radiographic film measurements. The relative stopping power through the sheep's head was calculated using both the conversion established from the real tissue samples and the substitute tissues. The comparison in measurements and calculations showed that the stoichiometric calibration was of greater precision than the tissue substitutes for proton beam therapy. *Schneider et al.* (1996) also advises that this method could improve on the precision for X-ray radiotherapy treatment planning.

Calibrating the TomoTherapy Imaging Beam

The TomoTherapy imaging beam also supplies a second use beyond daily correction: it provides a method of planned adaptive radiotherapy. At Addenbrooke's, Dose Difference Analysis (DDA) is routinely carried out for TomoTherapy patients to create a comparison of the planned dose and the delivered dose distributions for a fraction of treatment using the TomoTherapy planned adaptive module. The delivered dose is calculated by applying the delivered sinogram (describing MLC opening with time and gantry angle) to the MVCT image taken for the specified fraction. The dose distribution from the fraction and the planned distribution are then compared by viewing a dose difference map or by analysing DVHs. DDAs are performed routinely on specified fractions for several types of treatment, and also if a change in dose distribution is suspected, for example if there are set up issues or a change in weight. Out of tolerance DDAs are discussed with the clinician, and may indicate that a re-plan is necessary. As the MVCT images from TomoTherapy are used for DDAs, the TomoTherapy MVCT images require a conversion of HU to relative electron density for dose calculation. TomoTherapy use a method of converting to physical density, rather than relative electron density, using Image Value to Density Tables (IVDT) to allow for dose calculation. The energy relationship in both Compton Scattering and the Photoelectric Effect, as well as their atomic number dependency, accounts for a decrease in contrast in MVCT images compared to kVCT images. In the megavoltage energy range, Compton interactions are dominant even in high Z materials. Due to this difference in physical interaction probabilities a linear HU to electron density curve is expected for MV images. To use the MVCT images from TomoTherapy for dose computations, an MVCT HU number

to physical density calibration curve must be periodically obtained (*Langen et al.*, 2010).

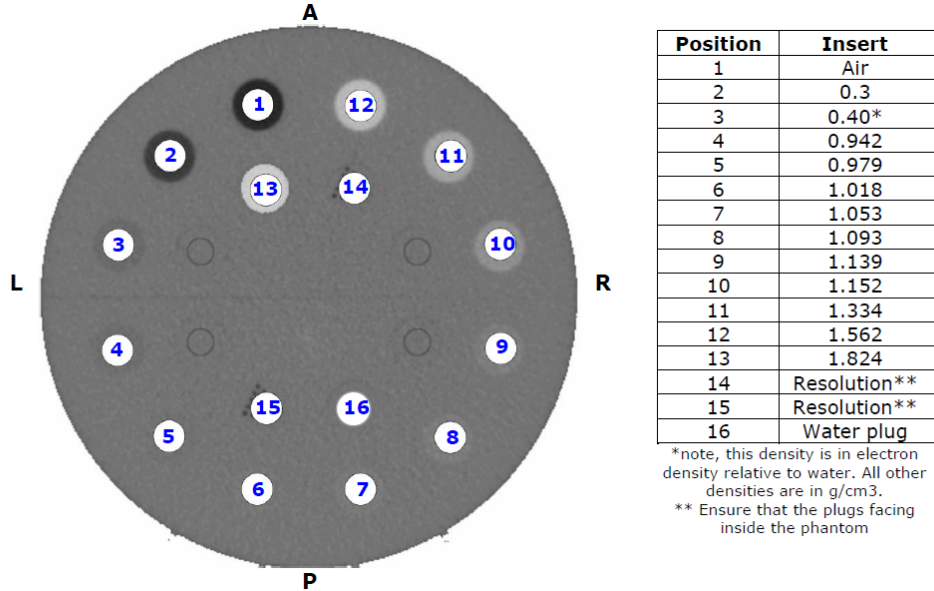


Fig. 3.3 Image taken from the Addenbrooke's Radiotherapy Department's work instruction for carrying out MVCT HU QA using the Cheese phantom on TomoTherapy

Without a stoichiometric phantom available for calibrating the MVCT to proton stopping powers relative to water another method was used. To calculate the WEPL from the MVCT data sets a calibration curve of HU to relative proton stopping power to water is required. The Addenbrooke's data were calculated by calibrating the scanner to electron density using the TomoTherapy 'Cheese' phantom with density plugs inserted as shown in Figure 3.3. This process is carried out routinely as part of the monthly MVCT imaging QA. The density plugs provided have values specified in g/m^2 . To convert the TomoTherapy HU to relative proton stopping power the approximate values for the electron density relative to water for the density plugs directly from Gammex were interpolated for values required. These values were then converted to relative proton stopping power using used the ratio shown in equation 3.2 (*Schaffner and Pedroni*, 1998)) and the mean beta value shown in the Table 3.1, where I_t and I_w are the ionisation potentials of tissue and water respectively, and I_w has been taken as 75eV (*ICRU 50*, 1993). The approximate mean excitation values, I-values, were supplied by Gammex (*Gammex*, 2009).

$$-\frac{dE}{dx} = \left(\frac{1}{4 \cdot \pi \cdot \epsilon_0}\right)^2 \cdot \left(\frac{4\pi^2 e^2 \rho_e}{m_e v^2}\right) \cdot \left[\ln\left(\frac{2m_e c^2 \beta^2}{I \cdot (1 - \beta^2)}\right) - \beta^2\right] \quad (3.1)$$

hence,

$$S_{rel} = \frac{\rho_e}{\rho_{ew}} \cdot \frac{\left[\ln \left(\frac{2m_e c^2 \beta^2}{I \cdot (1-\beta^2)} \right) - \beta^2 \right]}{\left[\ln \left(\frac{2m_e c^2 \beta^2}{I_w \cdot (1-\beta^2)} \right) - \beta^2 \right]} \quad (3.2)$$

The absolute stopping power is clearly energy dependent from the Bethe-Bloch formula ($\beta = \frac{v}{c}$). Using *Bortfeld and Schlegel (1996)*'s range-energy relationship shown in equation 3.3, four proton beam energies were chosen, within (or a bit above) the therapeutic range, to test if the relative stopping power can be assumed independent of proton energy allowing for one curve to be used for all therapeutic energies (*Hünemohr et al., 2014; Yang et al., 2012*).

$$R = \alpha \cdot E_0^P \quad (3.3)$$

where R is the range, E_0 is the initial particle energy; P is taken as 1.77 (*ICRU 78, 2007*) and α is proportional to the square root of the effective atomic mass divided by the density of the medium, which has been taken as 0.0022 for water (*Jette and Chen, 2011*).

In Table 3.2, β is calculated for four proton energies. For each insert the percentage difference between the relative proton stopping power calculated for each energy is shown in the far right column. As cortical bone has an I-value furthest from that of water, this is the tissue that will show the largest β dependency. The percentage difference in relative stopping power for the cortical bone insert was less than 0.6% for the two most extreme energies used, 90 MeV and 310MeV. With an error on the β value less than 0.6%, energy independency can be assumed for this work. The relative proton stopping powers have been calculated using the β associated with a 150MeV proton beam, as this beam energy can deliver a suitable treatment depth. It is already known from previous studies (such as *Yadav*

et al. (2010) and *Duchateau et al. (2010)*) that the IVDT can change over time, especially with target change, which if not taken into account, could result in an error in the dose calculation. Clinically we take a new IVDT each month to be compared to the one used in the adaptive module. However for this case each patient was treated at a different time period so an average IVDT has been used. The data plotted in Figure 3.4 is the average IVDT taken from both TomoTherapy units at Addenbrooke's taken over several months. Using all

Table 3.1 Calculating a mean β to use in the Bethe-Bloch equation to establish an energy independent proton stopping power relative to water

| Energy (MeV) | 90 | 150 | 260 | 310 |
|----------------------------|--------|--------|--------|--------|
| Proton Range in water (mm) | 63.3 | 156.35 | 413.92 | 565.11 |
| β | 0.4092 | 0.5067 | 0.6221 | 0.6596 |

Table 3.2 calculation of proton stopping power relative to water for each tissue using the energy specific β in the Bethe-Bloch equation. The I-values have been interpolated from the Gammex data tables

| Tissue Sub | I value (eV) | 90 MeV | 150 MeV | 260 MeV | 310 MeV | %diff |
|-----------------------|--------------|--------|---------|---------|---------|-------|
| Lung | 73.8 | 0.481 | 0.481 | 0.481 | 0.481 | -0.03 |
| Water | 75 | 1.00 | 1.00 | 1.00 | 1.00 | 0.00 |
| inner bone | 80.1 | 1.081 | 1.081 | 1.082 | 1.082 | 0.11 |
| Bone mineral | 80.2 | 1.091 | 1.091 | 1.091 | 1.092 | 0.11 |
| 30% CaCO ₃ | 80.8 | 1.259 | 1.258 | 1.259 | 1.259 | 0.12 |
| 50% CaCO ₃ | 93.1 | 1.432 | 1.431 | 1.433 | 1.434 | 0.36 |
| Cortical bone | 104.5 | 1.622 | 1.622 | 1.625 | 1.626 | 0.56 |

of the above, the following Table 3.3 and the plots in figures 3.5 and 3.6 were created. The equation of the line in figure 3.6 is the equation required in the equivalent depth algorithm to calculate the WEPL through the MVCT images for a proton beam. (If we wanted to know the WEPL change for conventional radiotherapy the line equation from 3.5 would be required.)

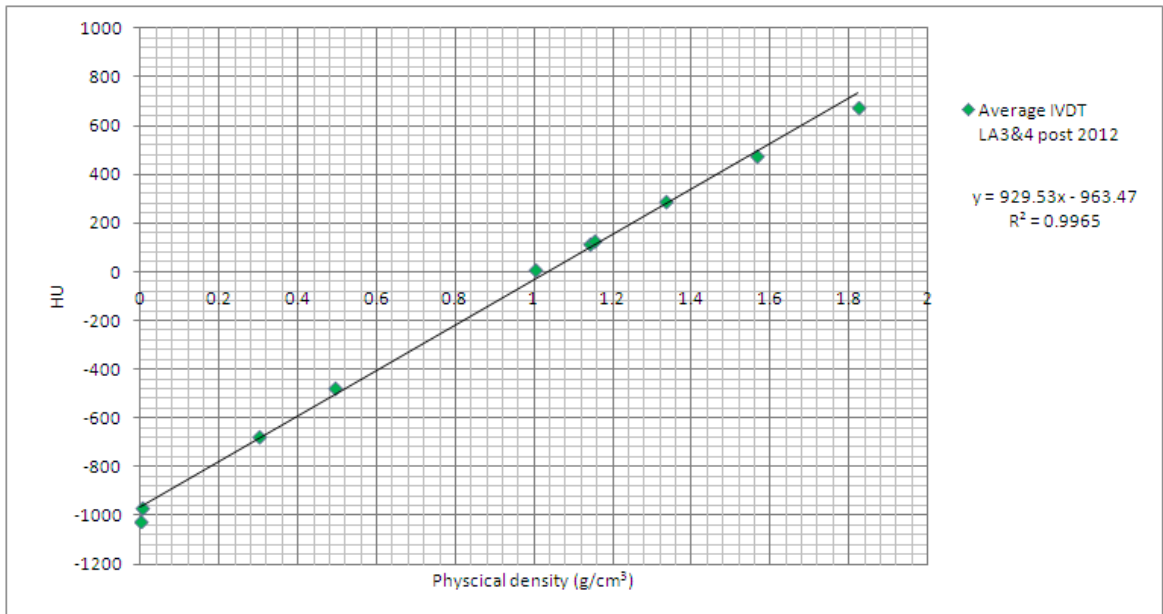


Fig. 3.4 Average MVCT IVDT from several months on both TomoTherapy units at Addenbrooke's

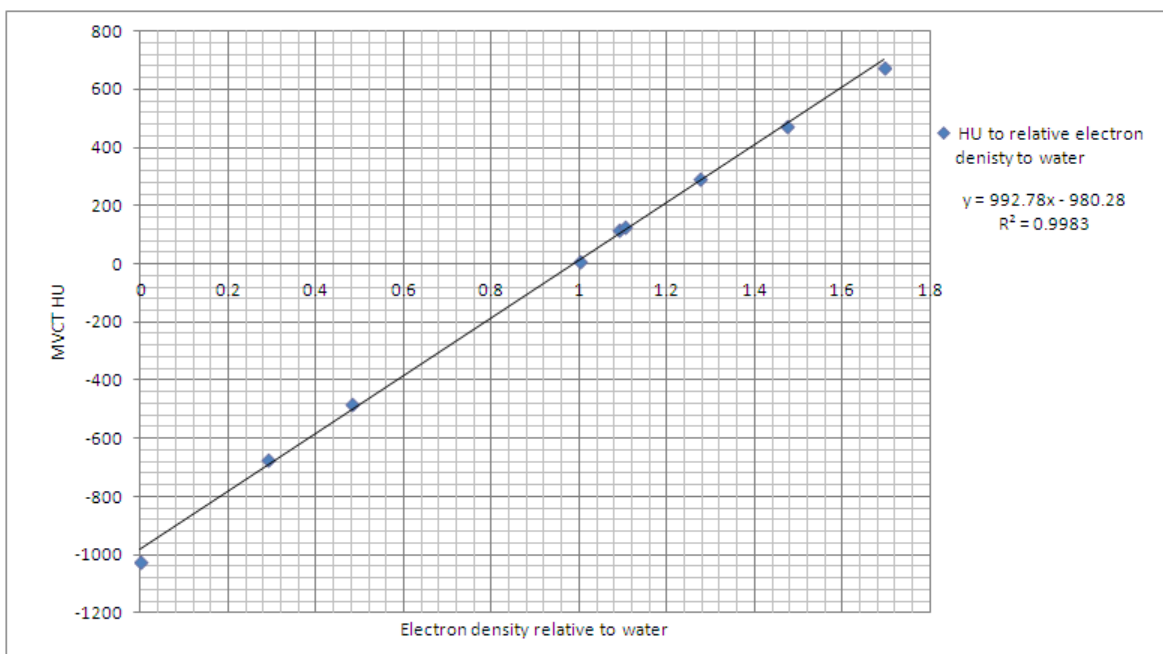


Fig. 3.5 Calibration curve of MVCT HU to electron density relative to water

Table 3.3 Table of density inserts used to calibrate the MVCT and their corresponding physical densities, estimated electron densities and proton stopping powers relative to water as calculated from the Bethe-Bloch equation using the β value to a 150MeV proton beam

| Tissue Sub | Density | e- Density | $SP_{w,150MeV}$ | HU |
|-----------------------|---------|------------|-----------------|------|
| Air | 0 | 0 | 0 | -970 |
| Lung | 0.49 | 0.48 | 0.481 | -479 |
| Water | 1 | 1.00 | 1.00 | 9.5 |
| inner bone | 1.139 | 1.09 | 1.081 | 118 |
| Bone mineral | 1.152 | 1.10 | 1.091 | 127 |
| 30% CaCO ₃ | 1.334 | 1.27 | 1.258 | 292 |
| 50% CaCO ₃ | 1.562 | 1.47 | 1.431 | 474 |
| Cortical bone | 1.824 | 1.69 | 1.622 | 673 |

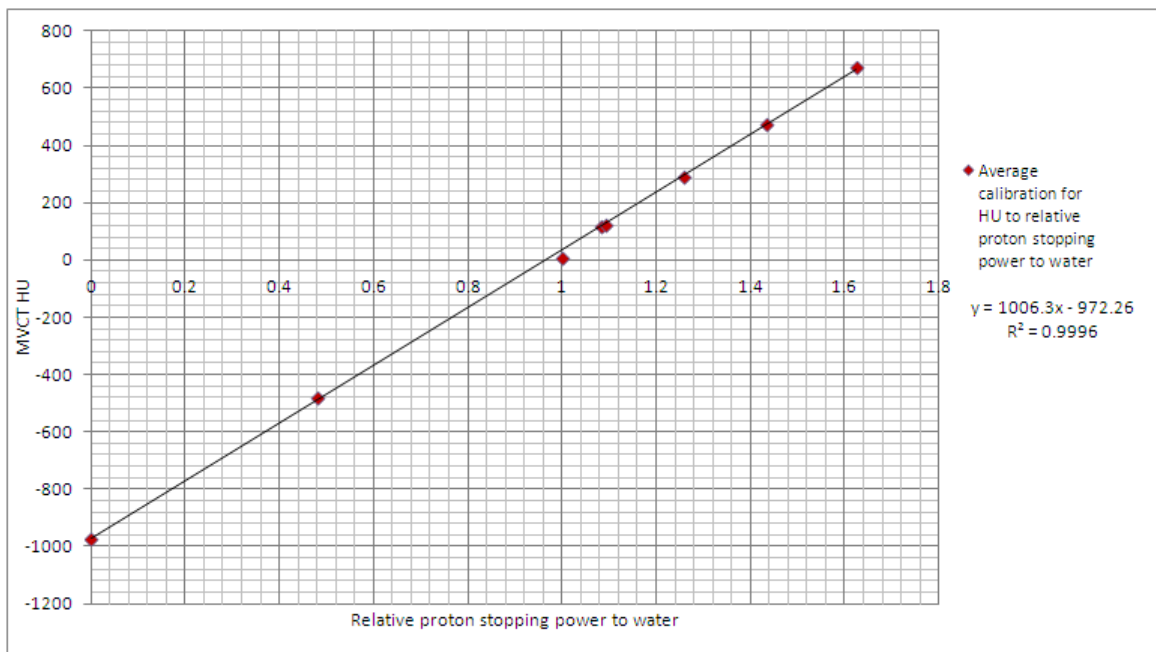


Fig. 3.6 Calibration curve of MVCT HU to proton stopping power relative to water

A shift in the HU representing water will have a larger impact than a shift in the HU representing bone since a typical patient image contains more water equivalent density material than bone-like materials (*Langen et al.*, 2010). For this reason real water has been used in the HU calibration. There is a large variability in the Addenbrooke's MVCT calibrations between the two scanners used to treat and image the patients in this study. There also exist errors related in interpolated I-values and electron densities of the inserts used in the Cheese phantom. The values supplied by Gammex required an interpolation, and as the relationship was hard to predict, a linear model was used. The I-value themselves constitute the largest error in stopping power in the Bethe-Bloch equation, with up to a 10% mean excitation energy variation, even for water (*Yang et al.*, 2012), the clinical impact of which is discussed in *Besemer et al.* (2013). Taking into account many of the uncertainties in calibrating HU to relative proton stopping power, it is estimated that even using a stoichiometric calibration errors of $\pm 3.5\%$ still exist (*Yang et al.*, 2012). There is currently research investigating the use of both kV-kV and kV-MV Dual Energy CT (DECT), where kV-MV DECT has the advantage of being less sensitive to uncertainties in the patient CT imaging (*Yang et al.*, 2012). The method described to calibrate the Addenbrooke's MVCTs to proton stopping power is not ideal for accurate measurements of WEPL and highlights the importance of using a stoichiometric calibration and purpose built phantoms. For the patient data used,

patients have been treated across both scanners and in different months throughout 2012 - 2014. For an exact study, appropriate curves are required for each scanner and each time period. The HU for each density insert has been acquired as part of the department's routine TomoTherapy QA. Due to beam hardening effects it would be better practice to image each insert at a time at the centre of the phantom. In this work it has been investigated whether this method of WEPL calculation could be used and whether it can yield a better estimate of random range error due to inter- and intra- fraction motion. It is envisioned that such a method could be applied in a proton centre using MVCT, or potentially CBCT. Due to the nature of this calibration and the assumptions made, the data presented in Chapter 4 is relative and not absolute and would be specific to Addenbrooke's Hospital.

3.3.1 Coding

I carried out all coding (described below) using MatLab which is a high level computing language that has pre-built functions which allows for fast programming (*Matlab UK*, 2011). It also has capabilities for reading and writing DICOM data and reading information from DICOM headers, which makes it a good language to use for this project. DICOM stands for Digital Imaging and Communications in Medicine and is a network protocol for medical data exchange. DICOM data includes a variety of image sources such as CT, MRI and PET. DICOM data can also be in the form of radiotherapy objects such as treatment plans, dose cubes and delineated structures. DICOM defines how all this data is stored and shared.

The list of the key functions, the description of their roles and the assumptions used as well as the code can be found documented in Appendix B. Here a short description of the process used to generate the probability distributions of inter-fraction range changes from patient MVCT data.

Daily Shifts

Beyond having an effective depth algorithm and a calibration to be used within it, the daily rigid couch shifts used on set for each fraction are required. For each treatment fraction on TomoTherapy the radiographer will set the patient up for treatment and perform an MVCT scan. The radiographer will perform image registration of the MVCT image to the planning kVCT making any of their own adjustments online and determine the final shift required in each axis (x , y , z) and for the roll. These shifts are translated to changes in the couch position

and are applied. The patient will then be treated in this position, further details of the treatment approach are given in *Burnet et al.* (2010). By applying these shifts to the MVCT image the patient position at the time of treatment can be simulated. The correction for roll has not been included in the calculation. As part of the VoxTox (*voxtox*, 2014) study shift data was extracted directly from TomoTherapy for all patients. This data was embedded into the DICOM header of each MVCT scan eliminating the human error involved in using numbers quoted on set.

To apply a shift to the 3D MVCT for a given fraction two coordinate systems of the same size of the MVCT matrix are created. The first is the coordinate system as retrieved from the DICOM header; the second is this coordinate system with the shifts added to it in each direction. For example if say pixel (1,1,1) existed at the coordinates (0,0,-12) and rigid couch shifts (0.5,1.5,-1) were applied, the new coordinate system for pixel (1,1,1) would be (0.5,1.5,-13). This is done to all pixels, in pixel dimension rather than in *mm*, and a 3D cubic interpolation is carried out to determine the new values of pixel data. In the x and y directions missing patient information is masked to correct for truncation artefacts. The pixels representing air are then all assigned to the same value.

Truncation Artefacts

If a patient is large compared to the field of view (FOV) or positioned with part of their body outside the FOV of the CT then truncation artefacts in the transmission data can occur (*McGowan et al.*, 2012). In radiotherapy truncation of either the region of interest, or of the patient outline is a problem for dose calculation. On TomoTherapy the scanning circle has a diameter of 38.6cm and truncation due to the scanning circle size is common, especially of the shoulders in head and neck plans and of the body in prostate plans. An example of scanning circle truncation of shown in Figure 3.7. Primarily the MVCT is used for daily registration, but in the case of dose re-computation for adaptive planning truncation needs to be corrected for. Solutions to correct for truncation artefacts include solutions such as using the kVCT data to fill in the missing data may be used. Alternatively, the body outline can be used to mask this missing data with a uniform pixel value. In both cases the daily shift will need to be applied to either the skin outline or the kVCT, so it will align correctly with the shifted MVCT. In this work a mixture of both methods was used. The kVCT was read in with the MVCT data and the shifts were applied to both. Knowing the scanning circle size, a mask was created for both CTs. The kVCT contributed the data that existed outside of the scanning circle and the MVCT provided the data within the scanning circle.

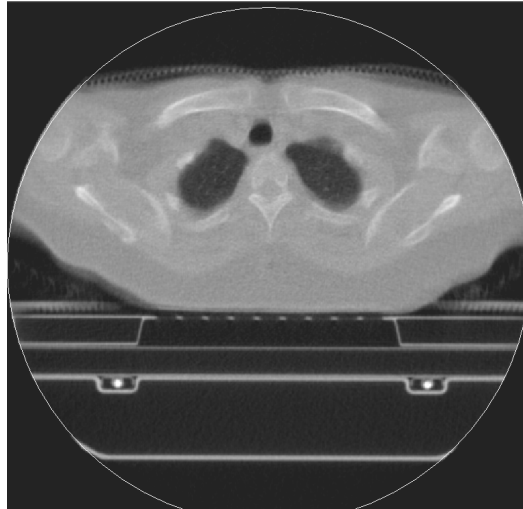


Fig. 3.7 Image of truncated patient on TomoTherapy showing the the scanning circle (white circle).

WEPL

To calculate the change in WEPL between fractions, each fraction is compared to a reference image. Due to the daily images and planning images having been obtained via different imaging modalities the reference image used was the MVCT of the first fraction in the treatment. The structure sets created at planning were used to determine the region of interest (ROI). The structure set of the ROI was read into the program and the coordinates of the structure were aligned to the corresponding shifted MVCT image slices. The resolution of the MVCT and the structure set differ in slice thickness so to determine which structure set slices were required the in-built MatLab function *ismember* was used to pinpoint the elements of the two matrix sets where the z coordinates were in correspondence.

The WEPL was calculated for a given beam direction, and beam parameters, using the shifted MVCT data and the effective depth algorithm previously described. To ensure the quality of the effective depth algorithm several verification tests have been carried out; these included testing the WEPL is accurate by setting the source to the surface of the CT image and the beam angle perpendicular to the pixels. This way the value of the pixel can be checked to determine if it was as expected and that the next pixel had a value equal to its own plus that of the previous pixel. An easy way to check the summation process is to look at water and see that the pixel value increases by a distance of one pixel each time.

Following the calculation of the WEPL, masks were used to retrieve the WEPL data from only pixels that exist inside the structure set for each fraction. Each subsequent fraction is then compared to the reference. All dimensions are converted into distances and volumes as required. Statistical parameters, such as the mean and standard deviation (in mm) of each data set were calculated; these represent the systematic and range errors associated with the treatment, both as a whole and at each fraction for that given beam angle.

Assumptions

Several assumptions have been made; these include

- The target has been delineated correctly.
- The target is in the correct location.
- The target has not rotated.
- Image matching and the shifts applied at treatment were correct.
- The target has not been deformed.
- Air outside the patient can be represented as a vacuum.
- The Source to Isocentre Distance (SID) has been set to seven metres in this study. This corresponds with the distance in the proton centre at CNAO, Pavia as provided to us by the physicists there, this is used simply as an example. At PSI, at dose calculation the SID is assumed infinite.

3.3.2 Analysis

For each set of patient data the WEPL for each pixel in the volume of interest for every fraction. The WEPL value stored in each pixel of the reference is then subtracted from that in each fraction. This gives the change in WEPL between the first and consecutive fractions. The data is stored in this raw form and also as binned data. A positive difference in range reflects undershoot scenario when compared to first fraction and for negative differences an overshoot scenario. The results can be displayed as histograms for each individual fraction.

The aim of this work is not to analyse individual fractions or even patients (though this information may be useful in analysing plan quality throughout the treatment delivery), but to analyse a sample of patient's treatments. The mean and standard deviation, σ of WEPL changes in mm are calculated for each beam angle across all patients and all fractions for both treatment site. The means of each individual fraction are also plotted as a histogram and the standard deviation calculated, Σ . It is these values that are being investigated and are required for a greater understanding of random range uncertainty in proton therapy.

3.4 Summary

There is a need to be able to quantify the random range uncertainty in proton therapy. In this chapter a method has been suggested by calculating the change in WEPL throughout treatment using daily volumetric imaging with rigid couch shifts applied. The process of creating a calibration curve of HU to relative proton stopping power for the TomoTherapy MVCT has been laid out. Though it is not a stoichiometric calibration, it is suitable for measuring changes in WEPL between fractions using daily MVCT images. Finally, an outline of the methods used to carry out this calculation have been described.

Chapter 4

Quantifying Site-specific Range Uncertainty

4.1 Introduction

The method described in chapter 3 is tested using clinical patient data to calculate the change in water equivalent path-length due to inter-fraction motion. Using a sample of patients and two treatment sites, the limitations of this method are explored. Finally, calculations for the overall mean, systematic and random range error for the patient sample are calculated.

4.2 Methods and Materials

Nine prostate and seven head and neck patients have been selected; these patients have been anonymised and tokenised for their relevant trials to uphold patient confidentiality. The standard protocol for prostate is to image daily using MVCT with a slice thickness of 6mm, and for head and neck it is 3mm. For the prostate cases, six of the patients were on the PIVOTAL trial. All patients, prostate and head and neck, are in the VoxTox study (*voxtox*, 2014). PIVOTAL is a phase II trial randomising between prostate and prostate + pelvic IMRT in patients with locally advanced prostate cancer (*Harris et al.*, 2011). VoxTox is a Cancer Research UK funded observational study at the University of Cambridge collecting toxicity data for patients undergoing image guided IMRT to the head and neck, prostate and CNS. For both treatment sites daily imaging has been carried out using MVCT on TomoTherapy and rigid shifts applied after soft tissue matching has been carried out by the treatment radiographers. This means that the range errors calculated in this chapter are

residual errors remaining after daily IGRT.

These specific patients have been selected because they were all treated on TomoTherapy at Addenbrooke's and have all given verbal and written consent for their images to be used for research. The VoxTox study was approved ethically by the NRES East of England Essex Ethics Committee in 2013. In the VoxTox study the head and neck cases required scans to have been long enough to ensure both parotid glands are imaged entirely on the MVCT. An increase in scan length by approximately 2cm was needed for around 80% of the cases. For the head and neck patients the estimated maximum dose using the standard protocol is 11.2 mSv. The estimated maximum dose using the study protocol is 12.2 mSv (*Bates et al.*, 2013). This dose is 0.2% of the maximum dose from their radiotherapy. The combined additional total dose corresponds to a risk of radiation-induced cancer during the rest of the lifetime of the standard population of approximately 1 in 20,750 (*ICRP*, 2007). The prostate patients were all treated for both prostate and nodes and no extra scan length was applied. In this work the change in WEPL within a Region of Interest (ROI) is carried out. The ROIs include the prostate without margins and the high dose CTV for the prostate and head and neck patients respectively. The advantage of the increased scan length in the head and neck data set, and the need for nodal irradiation in the prostate data set is that, despite the investigation only being focused on either the high dose CTV or prostate itself, there is a greater chance that the daily imaging will cover the entire ROI irrespective of the shifts that will need to be applied to align the patient. This will hopefully yield minimal truncation of the ROI in the scanning direction (superior-inferior direction). This is necessary for this study, as the results cannot be obtained if there is truncation of the ROI in the MVCT image at each fraction.

In the case of the prostate data two beam angles have been used to investigate inter-fractional changes in WEPL; a coplanar anterior and a lateral beam, 0° and 90° . In the case of the head and neck coplanar beam angles of 0° , 25° , 70° , 110° , and 180° have been used. The use of several beam angles was to gain an insight into how direction and the amount of traversing material affects the magnitude of range error. In the prostate case these two beam angles have been chosen, as they are clinically relevant beam angles. Though prostate is not a site that will be treated in the new proton centres in England, these data sets have been used in this work. For one of these patients there was opportunity to investigate intra-fraction changes. Permission was granted by the patient and ethically approved by NRES to image twice on some fractions, both before and after treatment as part of a study to determine

intra-fraction motion (*Thomas et al.*, 2013). However, using prostate cases within this work has been due partly to the data that was available. Irrespective of cancer site and whether this site will be eligible for treatment on the NHS, this data can be used to investigate how this method of quantifying range uncertainty could be used for any location. It also offers as an opportunity to investigate how range uncertainty can differ between site locations. The benefit of treating prostate cancer with protons over conventional radiotherapy has been a controversial topic in the proton therapy world and papers have been written on the topic (*Slater et al.*, 2004; *Vees et al.*, 2014; *Zietman et al.*, 2010).

Scanning circle truncation artefacts are present for both prostate and head and neck treatment sites and are an issue for several beam angles. In the case of prostate often a few centimetres (or less) of the body may suffer from truncation on several slices. This part of the body is fairly homogeneous and it has been assumed to have a uniform density. For the prostate patients a HU of -100 was used in the mask created from the kVCT. This was an estimate of the average HU value in this area based on several of the patient MVCT images. Truncation of the shoulders in the head and neck is more problematic due to the density changes in this region. A blanket HU number substitution could not be used and there was not a calibration created for the kVCT scanner. Due to the large number of slices the head and neck high dose CTV extends over, it was deemed acceptable to remove the last few MVCT slices so that the WEPL changes could be analysed without being compromised by truncation artefact.

In this chapter it is attempted to characterise the magnitude and probability of inter-fraction range error for prostate and head and neck treatments for the beam directions investigated. Though these sites and beam angles are not necessarily those that would be used clinically, the aim of this work is to demonstrate how using daily MVCT images could be used to quantify this error.

4.3 Results

4.3.1 Prostate

All prostate data sets were run for two beam angles, 0° and 90° . Despite using patient data sets that required prostate and nodal irradiation some fractions were found to be unusable due to missing prostate data in the scanning direction once the shifts were applied. This is a form of truncation artefact of the prostate itself. This is a real issue for IGRT studies,

including for VoxTox (*Bates et al.*, 2013). In Table 4.1 the full information about each prostate data set is supplied. This includes the patient token, the name of the structure investigated, the total number of fractions treated, the total number of fractions used in the analysis, what fraction the comparison was made to and finally, the percentage of the fractions that were used in the analysis. Though the names of the structures differ, all the volumes used were the prostate without margins applied. The different name was because for patients in the PIVOTAL trial it was required that the prostate be named 'Tp'. Despite attempting to use patient data that would not suffer from ROI truncation in the scanning direction many of the prostate fractions could not be analysed due to part of the ROI being missed off the scanning image.

The WEPL for each fraction is compared to the WEPL of a reference fraction and the difference is stored. This data has been presented as histograms, each of which are plotted in figures 4.1 to 4.2. Each of the plots in these figures are heat maps of the frequency of the WEPL difference at each fraction. The darker the colour the greater the frequency of a difference in WEPL of that magnitude. Along the x-axis is time in terms of fractions, and along the y-axis is the change in range in millimetres. The zero line is shown so it can be seen how the mean range error at each fraction changes with time. The plots have been truncated down for visual purposes so outliers are not always represented here. However all data, including outliers are included in the statistical analysis. The left hand set of the histograms are for a beam angle of 0° and the right hand set of the histograms are for a beam angle of 90° .

To investigate how the random range error changes with both the beam angle and treatment fraction the standard deviation of range errors for each fraction has been plotted in Figures 4.4 and 4.3 for each beam angle. The colour represents a different beam angle, with blue being 0° and red being 90° , and each plot is a single patient. Again the x-axis is time in terms of treatment fraction, but the y-axis is the standard deviation in millimetre for that fraction and beam angle. It can be seen there is a beam angle dependency for most of the patients with a 0° beam angle resulting in random range errors with a smaller standard deviation.

Table 4.1 Prostate data showing the target and number of fractions used. The final column shows the percentage of fractions that did not suffer target truncation at daily imaging

| Token | Target | Total #s | Usable #s | Compared to # | %data usable |
|-------|----------|----------|-----------|---------------|--------------|
| 4 | Tp | 37 | 26 | 3 | 70.3 |
| 7 | Prostate | 37 | 13 | 2 | 35.1 |
| 21 | Tp | 36 | 12 | 2 | 33.3 |
| 34 | Tp | 37 | 26 | 1 | 70.3 |
| 36 | Prostate | 37 | 12 | 1 | 32.4 |
| 58 | Tp | 37 | 37 | 1 | 100.0 |
| 72 | Prostate | 37 | 19 | 2 | 51.4 |
| 78 | Tp | 37 | 19 | 4 | 51.4 |
| 95 | Tp | 37 | 28 | 2 | 75.7 |

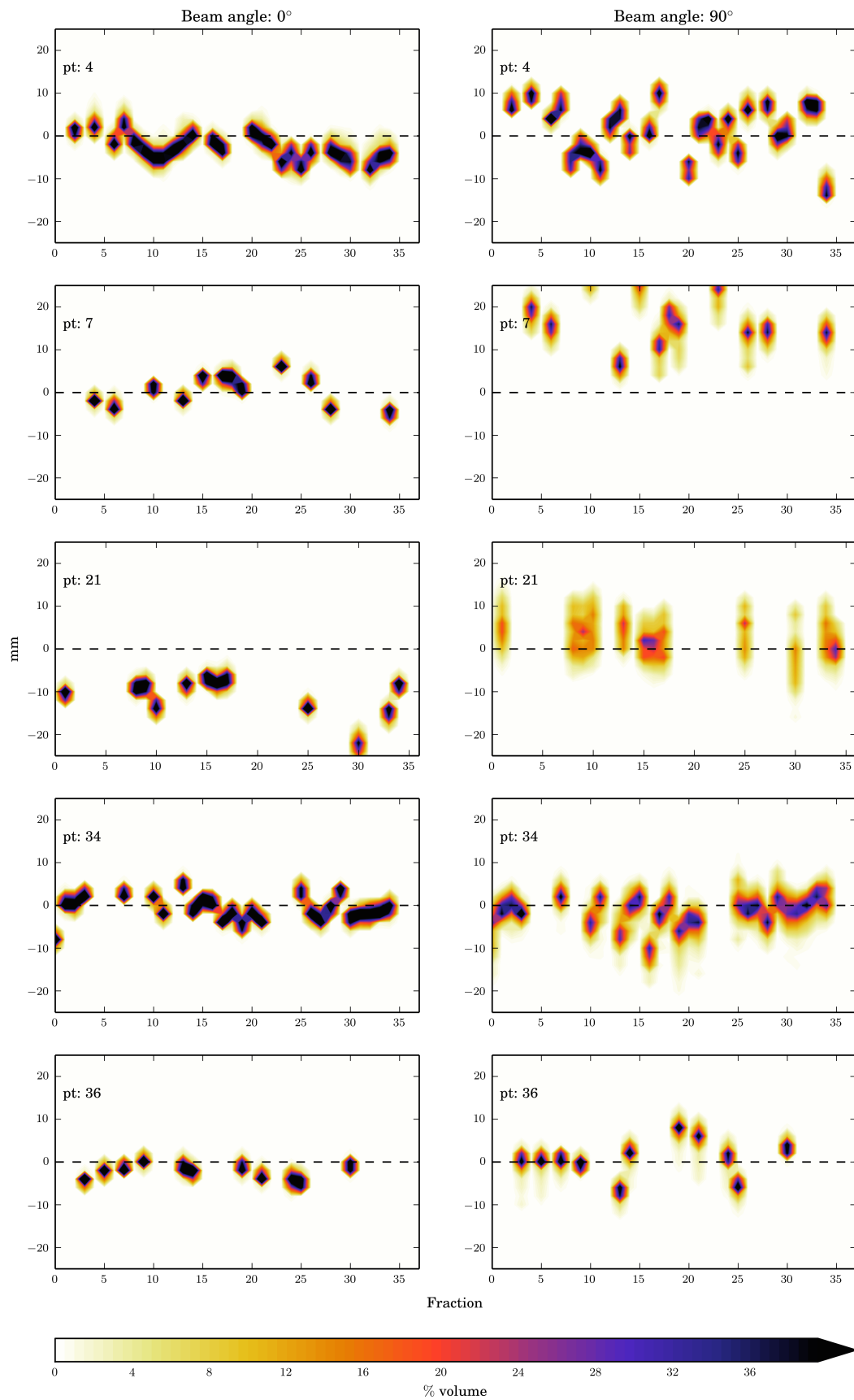


Fig. 4.1 Heat plots of %volume range error histograms for prostate patients 4, 7, 21, 34, and 36 (in order top to bottom) with fraction using 0 and 90 degree beam angles.

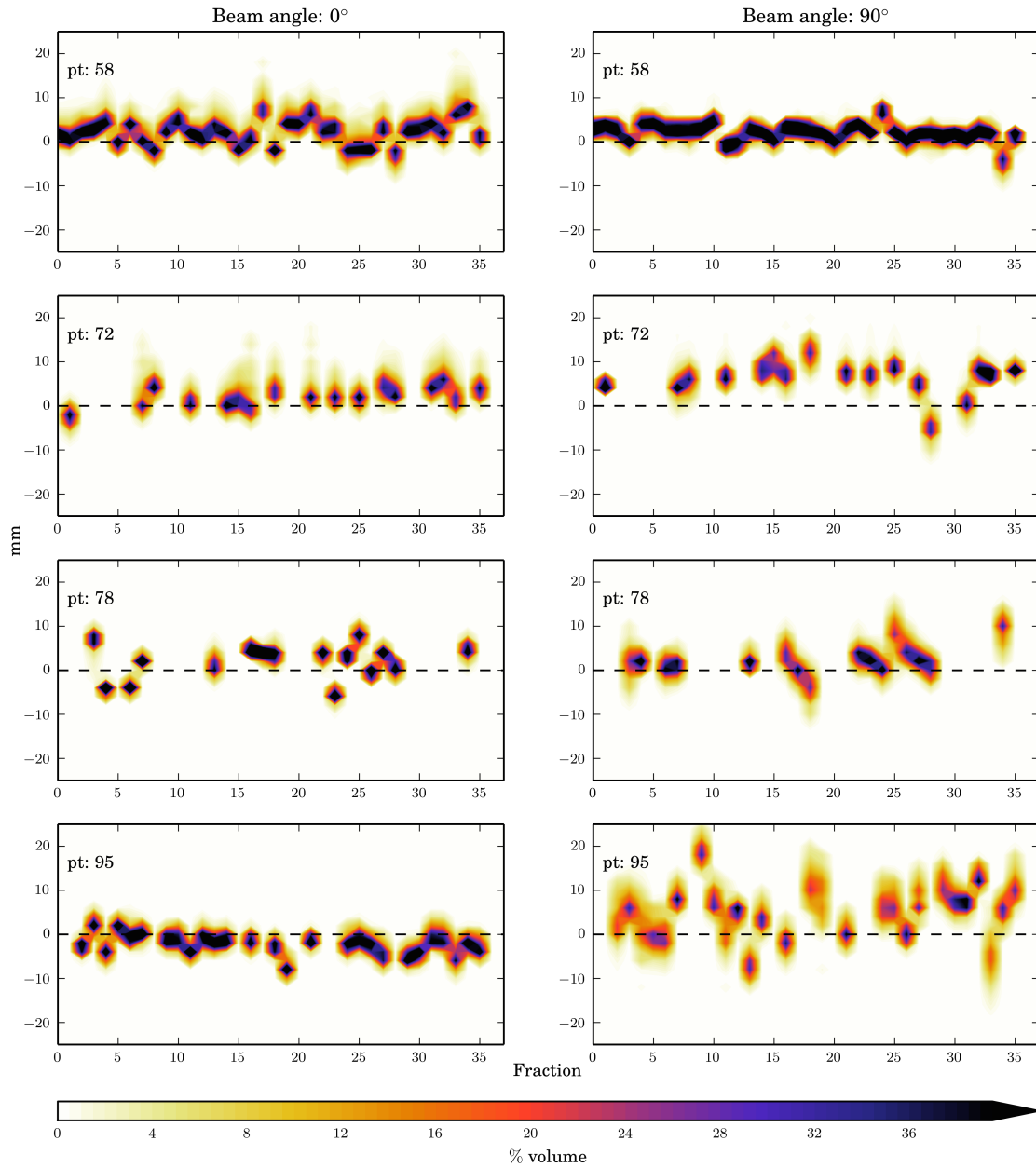


Fig. 4.2 Heat plots of %volume range error histograms for prostate patients 58, 72, 78 and 95 (in order top to bottom) with fraction using 0 and 90 degree beam angles.

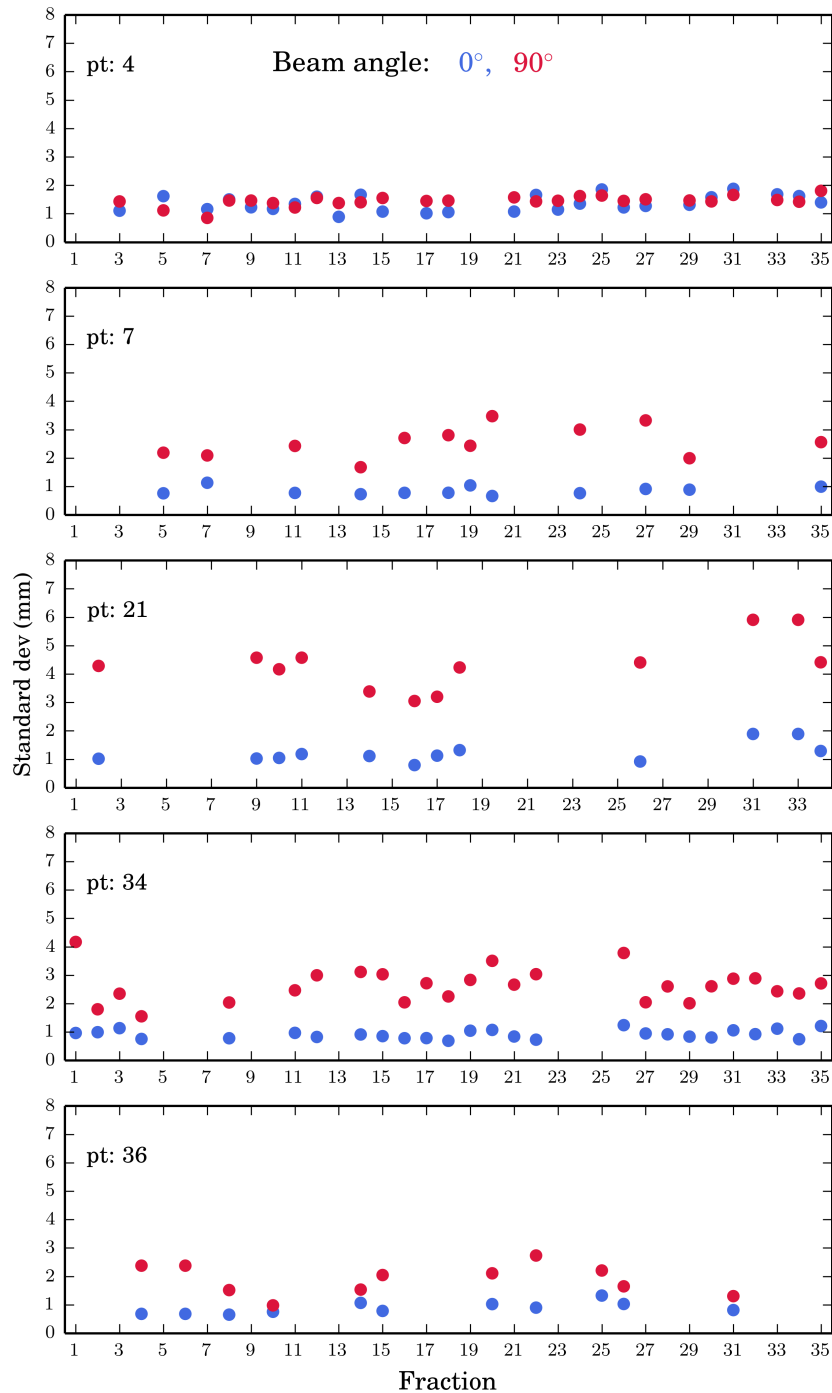


Fig. 4.3 Plots of the standard deviation for patients 4, 7, 21, 34, and 36 (in order top to bottom) of range error with fraction and beam angle.

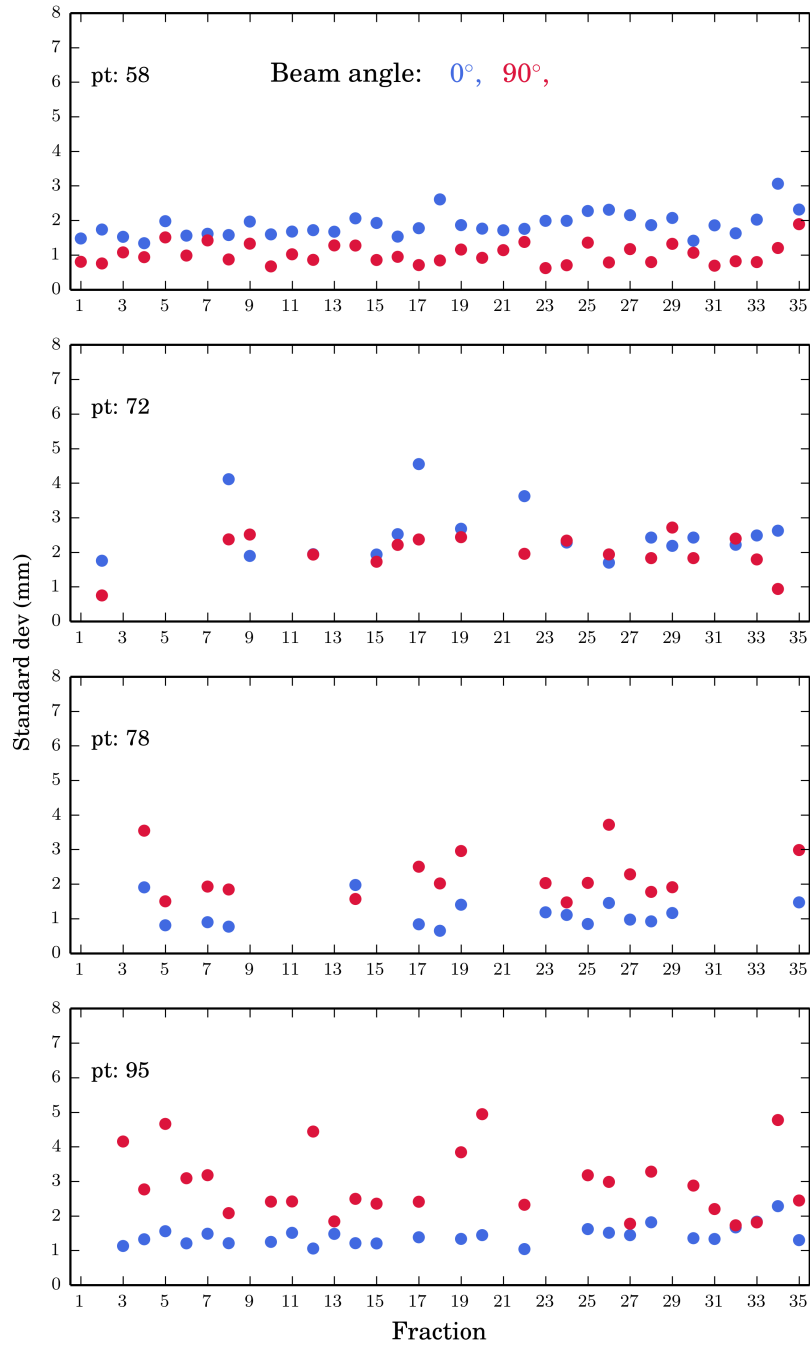


Fig. 4.4 Plots of the standard deviation for patients 58, 72, 78 and 95 (in order top to bottom) of range error with fraction and beam angle.

Intra-fraction

For patient 58, eight fractions were imaged before and after treatment. This has allowed for the WEPL change within a treatment fraction to be measured for this patient. The mean time between the start of the first image and the end of the second was 12 min (*Thomas et al.*, 2013). The intra-fraction results included in table 4.2 showing the patient mean and standard deviation (σ) in mm.

4.3.2 Head and Neck

Seven head and neck patients were analysed for five angles, 0° , 25° , 70° , 110° and 180° , as shown in Figure 4.5. The high dose CTV was used as the ROI for these patients. The high dose CTV includes the nodal region extending down the patient's neck. Table 4.3 includes all the information about these patients including the percentage of the treatment successfully analysed. The fractions that could not be analysed were due to part of the region of interest being missed off the scanning image. In the head and neck cases the first or second fraction has been used as the reference to make comparisons. Figures 4.6 to 4.8 show the heat plots of the change in WEPL histograms for each fraction and 4.9 shows the standard deviation of WEPL change in mm at each fraction for each patient and beam angle.

Table 4.2 Table of Intra-fraction changes in WEPL for a single prostate patient, 58, at beam angles 0° and 90° .

| Angle | 0° | | 90° | |
|----------|-----------|---------------|------------|---------------|
| Fraction | Mean (mm) | σ (mm) | Mean (mm) | σ (mm) |
| 1 | 1.6 | 1.46 | 3.68 | 0.77 |
| 5 | 0.15 | 1.66 | 2.36 | 1.2 |
| 12 | -1.42 | 0.57 | -1.22 | 0.93 |
| 13 | -0.13 | 1.72 | 3.84 | 1.48 |
| 21 | -0.24 | 0.79 | 0.39 | 0.69 |
| 26 | 1.77 | 1.66 | -5.95 | 0.85 |
| 27 | 5.6 | 1.5 | 7.3 | 1.41 |
| 28 | 1.73 | 2.05 | 1.81 | 1.54 |
| Average | 1.13 | 0.59 | 1.53 | 0.37 |

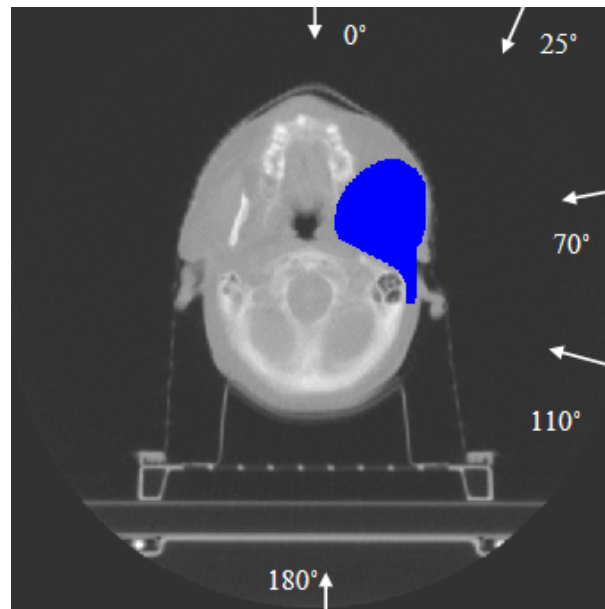


Fig. 4.5 Screen shot of a single slice of Patient 78 showing the high dose CTV and approximate angles used to calculate WEPL

Table 4.3 Table of Head and Neck data showing the targets and number of fractions used. The final column shows the percentage of fractions that did not suffer target truncation at imaging

| Token | Target | Total #s | Usable #s | Compared to # | %data usable |
|-------|--------|----------|-----------|---------------|--------------|
| 35 | CTV65 | 30 | 30 | 1 | 100.0 |
| 51 | CTV65 | 31 | 21 | 2 | 96.8 |
| 52 | CTV65 | 34 | 30 | 1 | 52.9 |
| 78 | CTV60 | 30 | 30 | 1 | 100.0 |
| 91 | CTV60 | 30 | 28 | 1 | 93.3 |
| 92 | CTV65 | 30 | 30 | 1 | 100.0 |
| 102 | CTV68 | 40 | 28 | 2 | 70 |

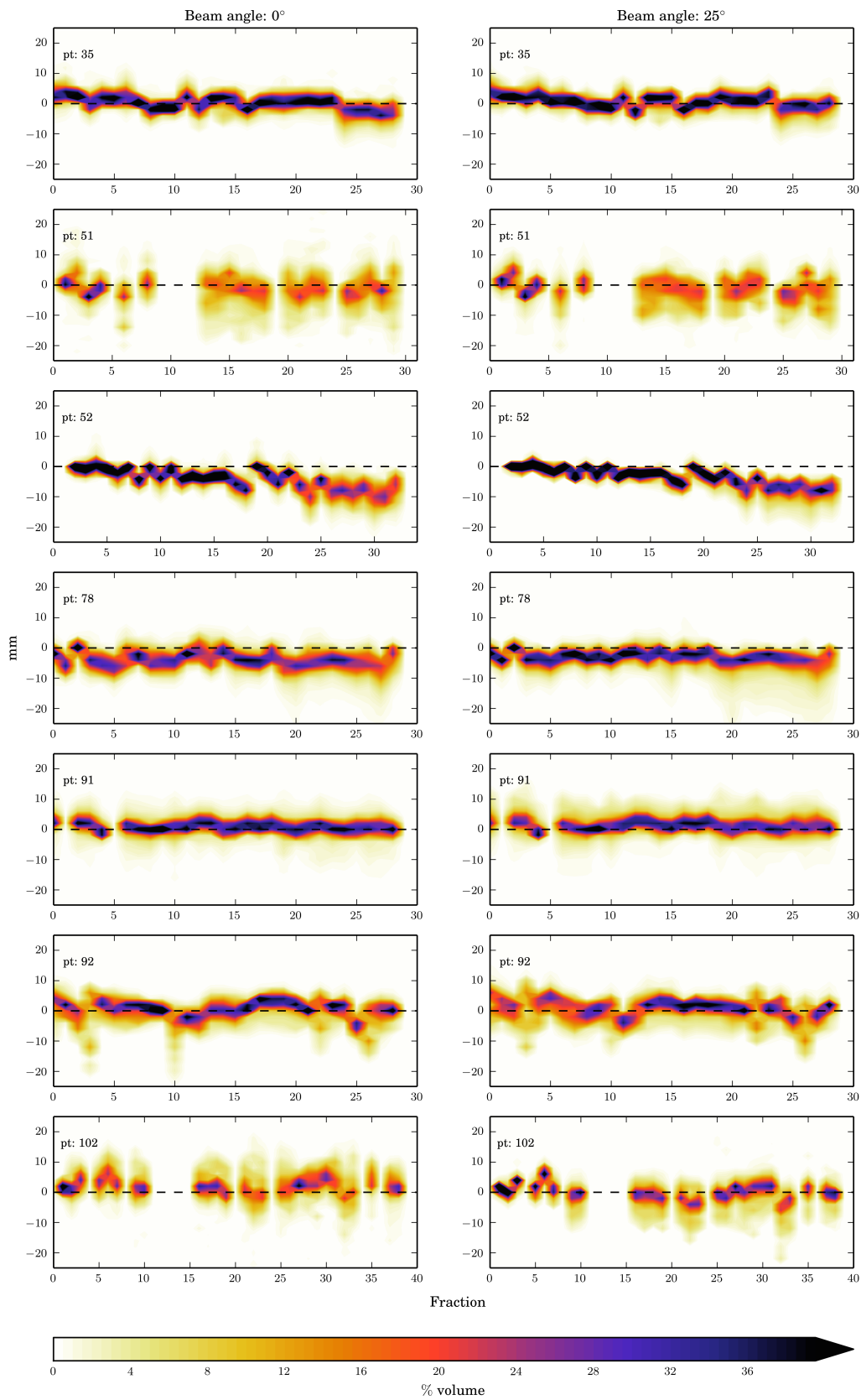


Fig. 4.6 Heat plots of %volume range error histograms for all head and neck patients with treatment fraction at 0 and 25 degree beam angles.

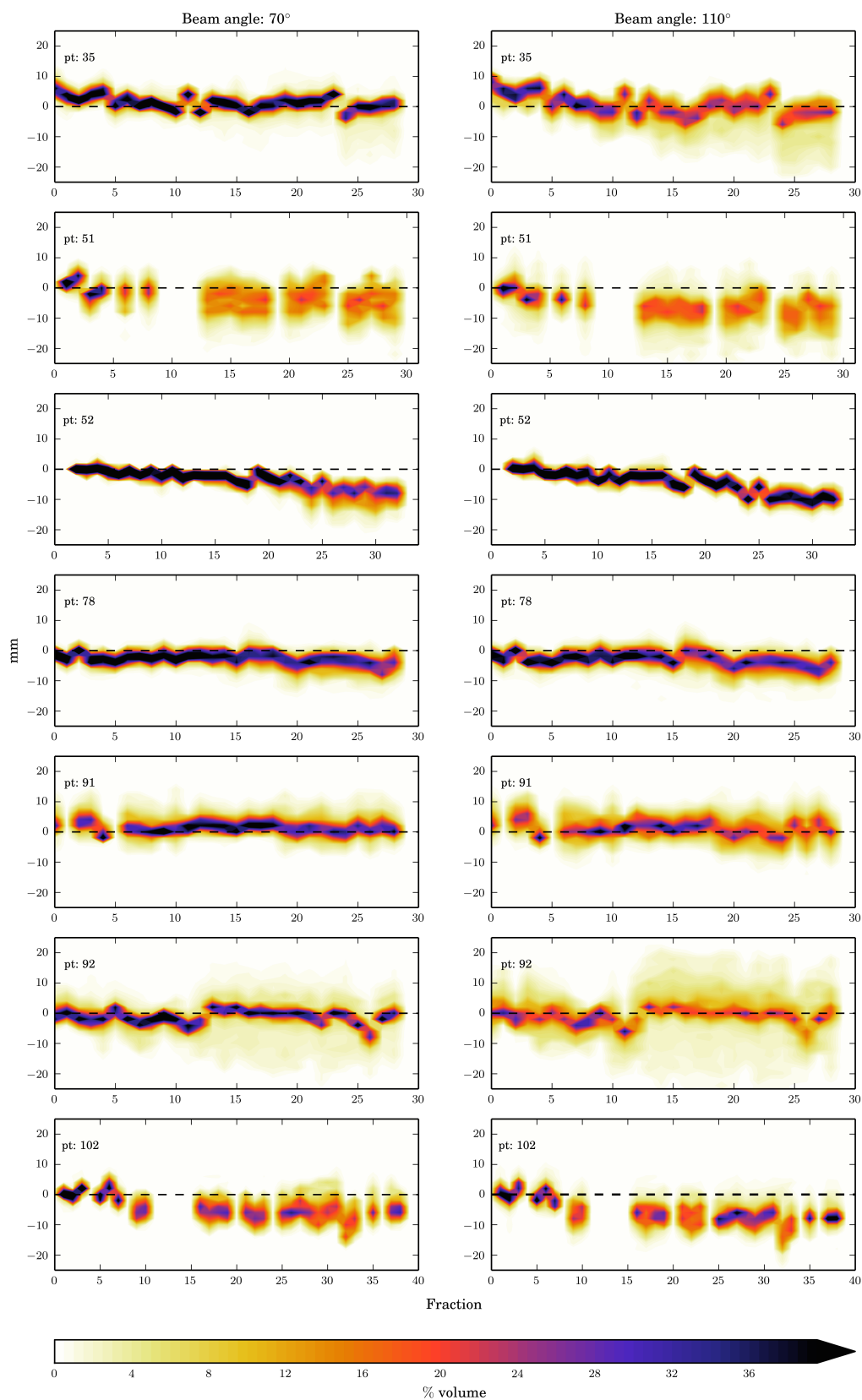


Fig. 4.7 Heat plots of %volume range error histograms for all head and neck patients with treatment fraction at 70 and 110 degree beam angles.

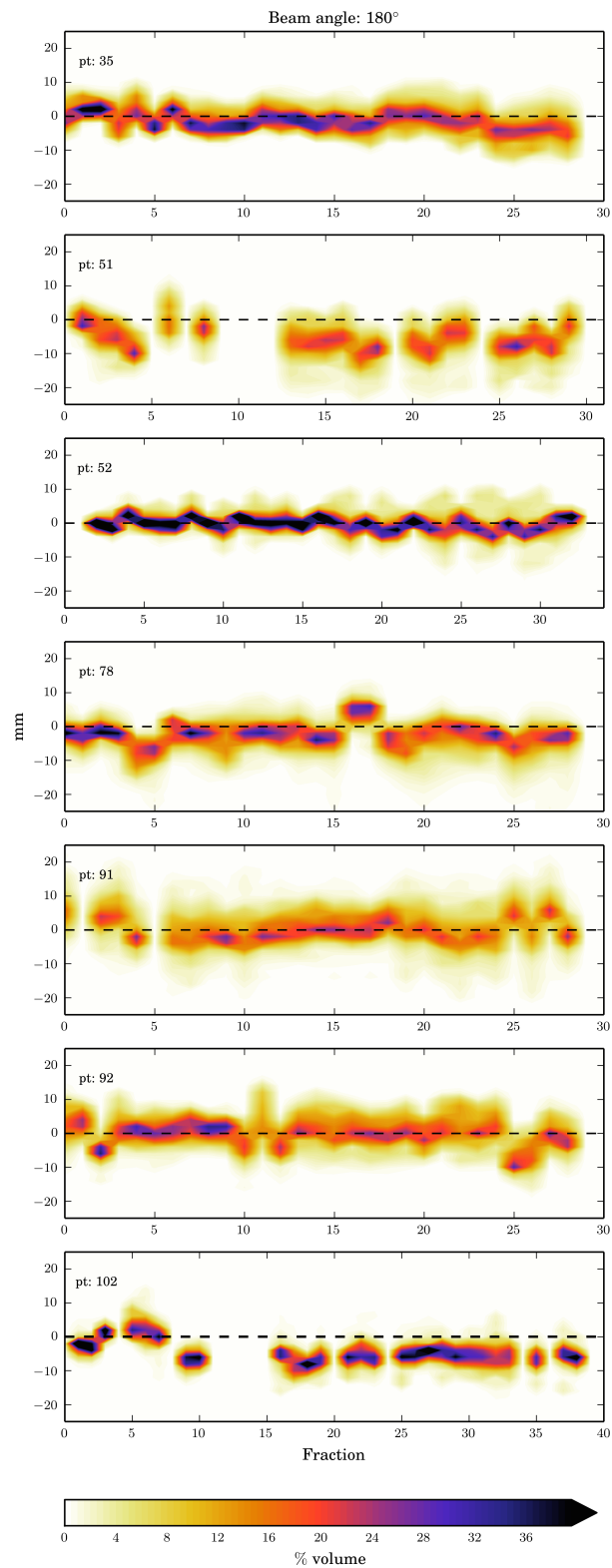


Fig. 4.8 Heat plots of %volume range error histograms for all head and neck patients with treatment fraction at 180 degree beam angle.

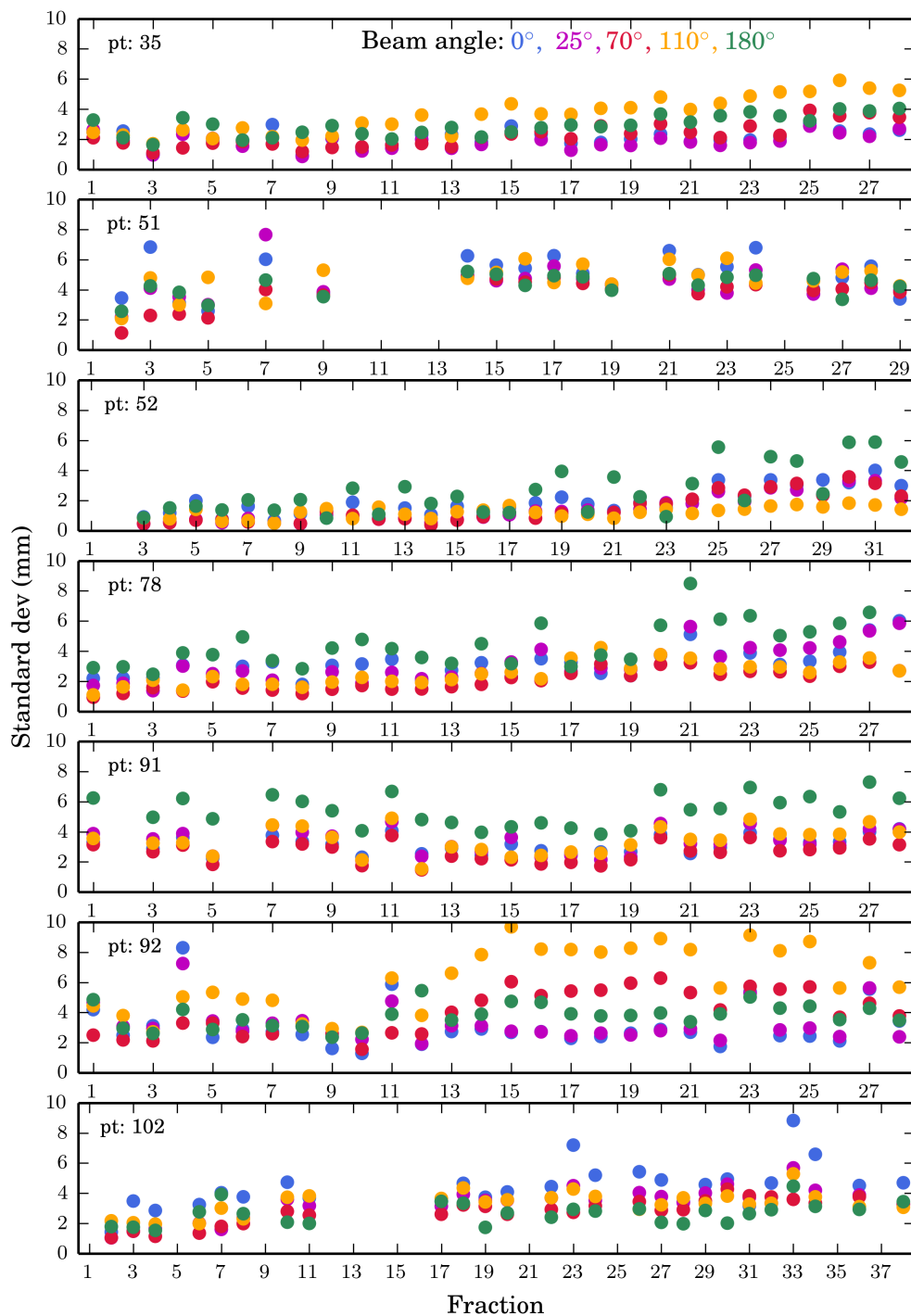


Fig. 4.9 Plots of the standard deviation of range error for each patient with fraction and beam angle.

4.3.3 Population Data

The aim of this project was to build a better understanding of the magnitude of range uncertainty from daily patient changes in proton therapy. It was also to determine a method for this information to be used at robust optimisation and plan analysis. In treatment planning a single composite random range uncertainty is convenient for either choosing margins, or for using in a robust optimisation. To this end, estimates of the overall mean error, random inter-fraction and systematic inter-fraction error for all patients have been calculated. These have been calculated using methods similar to those set out by *Greener* (2003), though here weighting has been by number of images analysed rather than number of patients for both the overall mean and the systematic uncertainty (Σ). The systematic inter-fraction error was calculated by plotting a histogram of the mean range change for each usable fraction across all patients and beam angles shown in Figures 4.10 to 4.13 and taking the standard deviation. Figure 4.13 shows the overall mean histogram for both the prostate data (top) and head and neck (bottom). For all histograms, a Gaussian distribution has been fitted.

For prostate and head and neck patients, the binned data from every fraction for each beam angle was also plotted, but as a line histogram shown in Figures 4.14 and 4.15 for each treatment site respectively. The black histogram represents the average histogram of all angles, whereas the colours represent individual beam angles. The standard deviation (σ) were calculated from all the non-binned fraction data, this means that the random uncertainty was calculated with weighting on number of data points and not number of images. All means, Σ 's and σ 's for all patients for each beam angle, are shown in Tables 4.4 and 4.5 and is representative of that treatment site.

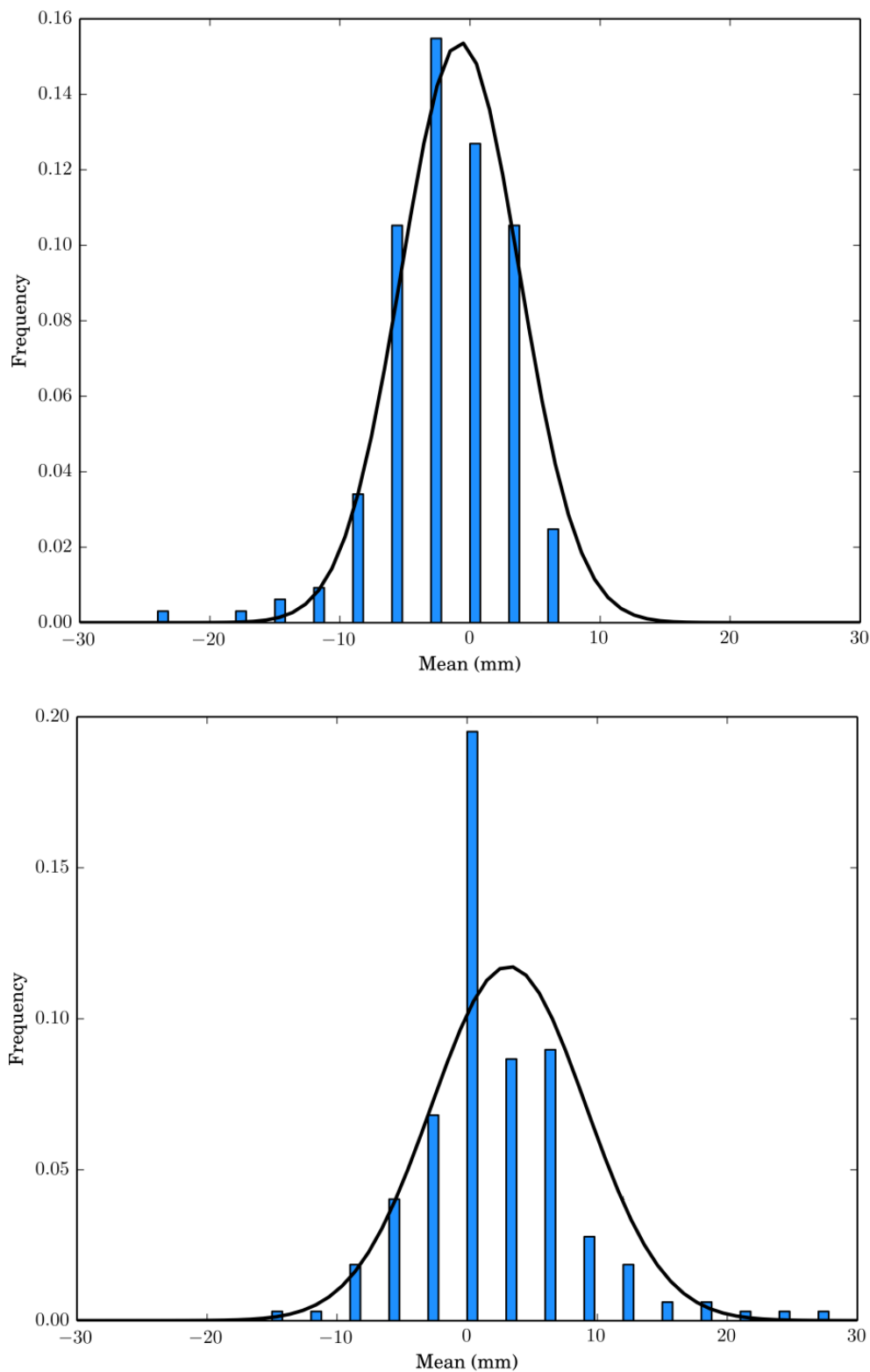


Fig. 4.10 The fractional means of WEPL difference for each prostate patient was plotted as a histogram for both angles (top is 0° and bottom 90°). The total mean can be taken from these plots for each angle as well as the standard deviation which is the systematic component of the range error for these sites.

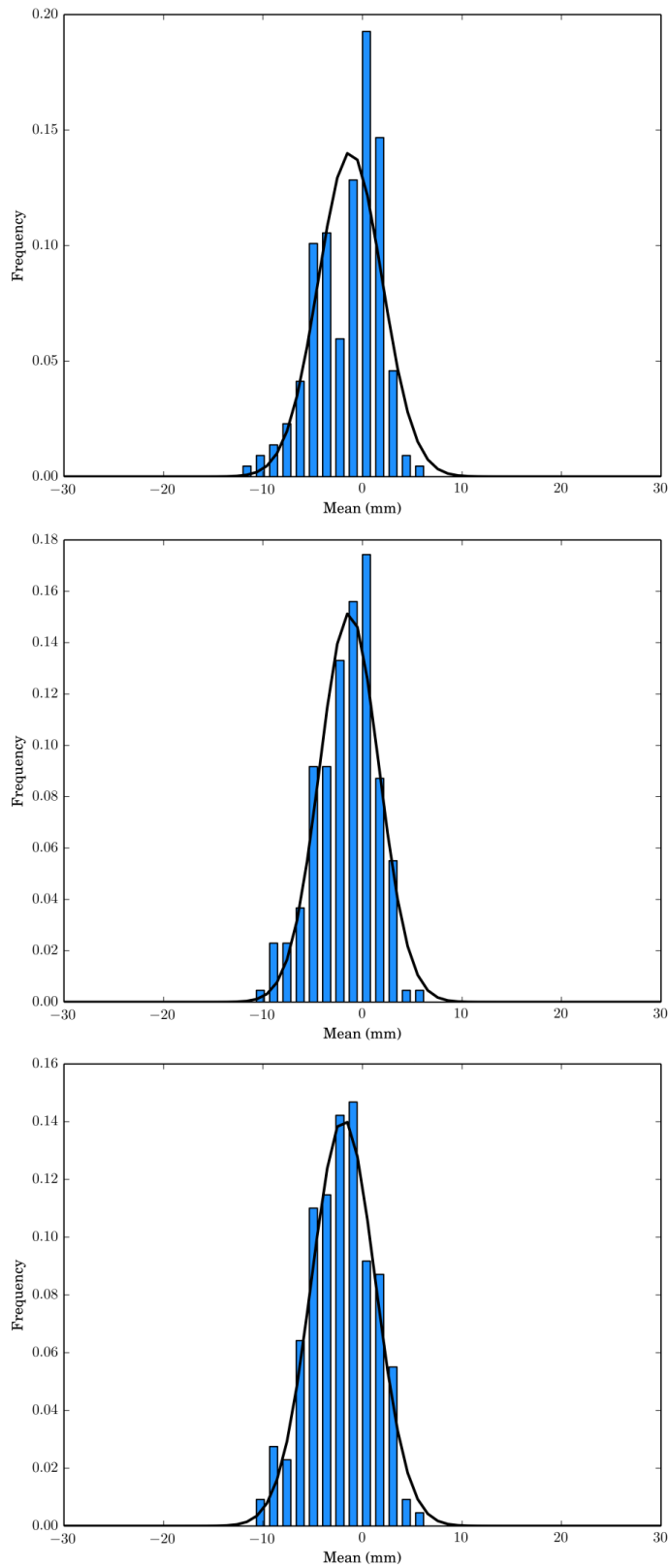


Fig. 4.11 The fractional means of WEPL difference for each head and neck patient was plotted as a histogram for three angles (top is 0° , middle is 25° and bottom 70°). The total mean can be taken from these plots for each angle as well as the standard deviation which is the systematic component of the range error for these sites.

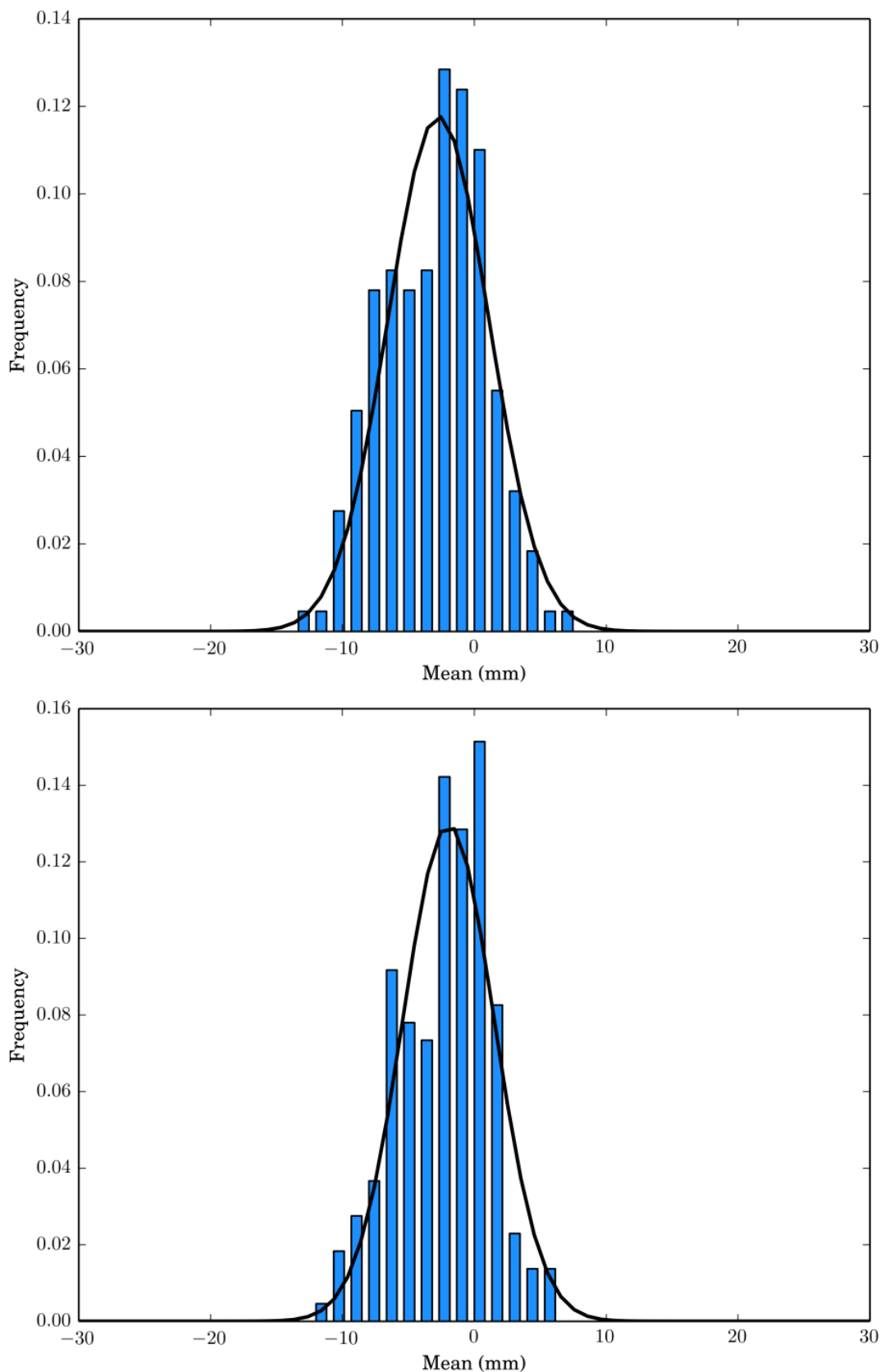


Fig. 4.12 The fractional means of WEPL difference for each head and neck patient was plotted as a histogram for three angles (top is 110° and bottom 180°). The total mean can be taken from these plots for each angle as well as the standard deviation which is the systematic component of the range error for these sites.

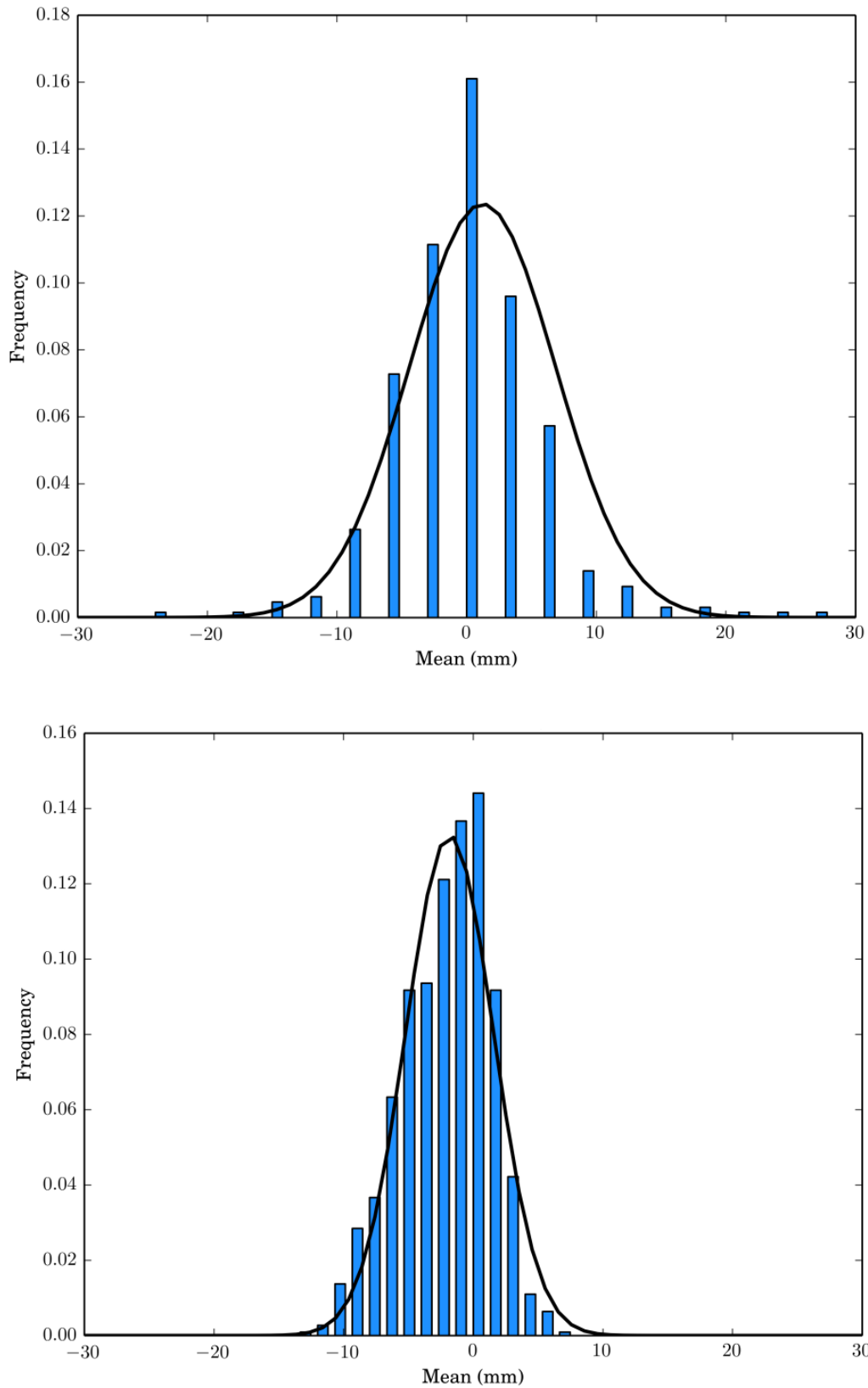


Fig. 4.13 The fractional means of WEPL difference for all prostate patients (top) and all the head and neck (bottom) were plotted as a histogram for all angles. The total mean can be taken from these plots as well as the standard deviation.

Table 4.4 Table of prostate range error in mm for all patients at each beam angle.

| Angle | Mean (mm) | $\Sigma(mm)$ | $\sigma(mm)$ |
|-------|-----------|--------------|--------------|
| 0 | -0.98 | 4.53 | 5.37 |
| 90 | 2.94 | 5.94 | 6.45 |
| All | 0.98 | 5.64 | 5.91 |

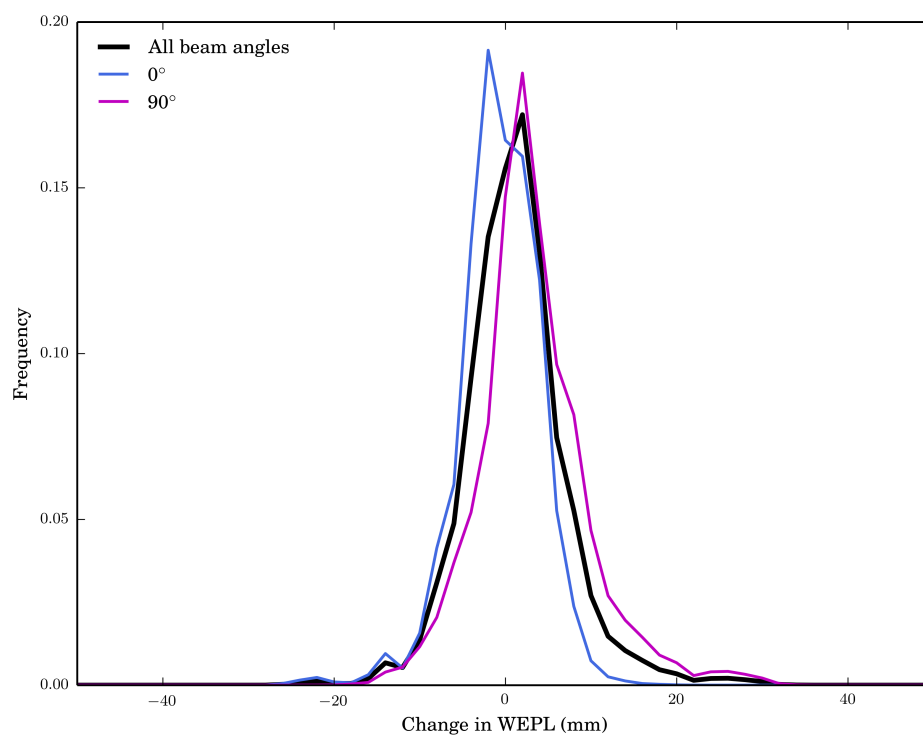


Fig. 4.14 The binned prostate data for each beam angle from each fraction for all patients was summed and plotted as a histogram normalised to one. Each colour represents a beam angle, and the black histogram is of all binned data.

Table 4.5 Table of head and neck range error in mm for all patients at each beam angle

| Angle | Mean (mm) | $\Sigma(mm)$ | $\sigma(mm)$ |
|-------|-----------|--------------|--------------|
| 0 | -1.22 | 3.21 | 4.71 |
| 25 | -1.31 | 2.97 | 4.47 |
| 70 | -1.91 | 3.20 | 3.93 |
| 110 | -2.71 | 3.83 | 4.81 |
| 180 | -1.95 | 3.48 | 5.69 |
| All | -1.82 | 3.39 | 4.72 |

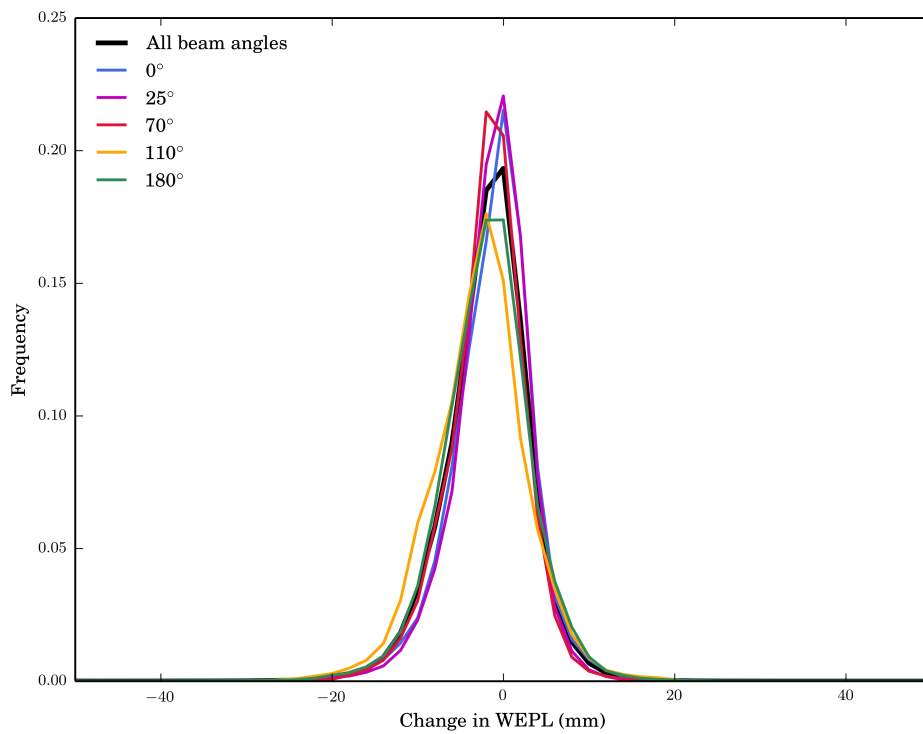


Fig. 4.15 The binned Head and neck data for each beam angle from each fraction for all patients was summed and plotted as a histogram normalised to one. Each colour represents a beam angle, and the black histogram is of all binned data.

4.4 Discussion

The method previously described in Chapter 3 has been tested using patient data to determine the range changes for a selection of prostate and head and neck patients. The range error from inter-fraction motion has been calculated by comparing the WEPL in each pixel within a region of interest at each fraction to the equivalent one in a fraction chosen, usually the first fraction, as a reference. Ideally, each treatment fraction would be compared to the planning CT, as this is the reference scan the treatment will be planned to. Due to the difference in the two modalities, kV and MV imaging, this not been carried out. However, another solution may be to acquire an MVCT at the same time as the planning kVCT.

In the prostate data the gaps seen in the plots is where imaging data was missing for these fractions. From the heat maps it was seen that there was a large spread in the means and no particular trend in their values. The standard deviation was seen to be larger for 90° , yet there was not a distinguishable difference seen in that mean values between the two angles. For 90° the standard deviation was greater than that seen for 0° in all except two patients, one of which the standard deviations of both angles were comparable. The spread in means represent the systematic component of inter-fraction error, whereas the standard deviation represents the random component. The larger range errors seen in the 90° was most likely caused by the fact that the prostate moves independently of bony anatomy and the images are aligned to soft tissue matching. Comparing the standard deviations for individual fraction in Figures 4.3 and 4.4 could be misleading, as the large standard deviation seen in the prostate population data does not appear to coincide with the individual fraction data. This is due to the large variation in the mean as seen in the heat maps. A large amount of the data could not be analysed due to missing data within the ROI, which leads to a bias in this data set. One patient, patient 58, had their images used to investigate intra-fraction range changes for eight fractions. The results from are less than 1mm and as expected, comparable to the results seen in *Thomas et al.* (2013).

For the head and neck data a lot more images could be analysed leading to more reliable data. The mean range error at each fraction is seen to be closer to zero than that seen in the prostate and there is less variability in the means with fraction. There is a noticeable shift in the mean from zero for several patients with time which is also seen in the population results. This shows that throughout treatment the WEPL is decreasing. This may be due to slight weight loss and represents a risk of proton overshoot. Three patient examples are shown in Figure 4.17, each shows an overlay of the same MVCT slice of the first and last fraction.

Yellow represents pixels that match well, red represents the first fraction image and green the final fraction image. Slight weight loss throughout treatment appears uniform across this sample and across beam angles. There is a larger spread in ranges seen for the larger beam angles (70° - 180°). This is due to two reasons. Firstly, that the 'beam' is passing through a greater volume of the patient before reaching the target, and travelling through more density heterogeneities. Secondly, for some of the patients, the high dose CTV was on the opposite side of the head and neck to the direction of the beam angles chosen. This has led to a larger amount of tissue to be traversed, as well as more density heterogeneities in the proton path. Further investigation using clinical treatment beam angles is required. Due to this second issue a slightly smaller standard deviation for the head and neck population may be expected. The standard deviation in the head and neck for angles 110° and 180° were larger than those seen in the prostate data. This is most likely due to the density heterogeneities seen in the head and neck leading to larger range uncertainties.

In several of the head and neck patients the CTV was partly in the mouth and when using angles such as zero or 25° the proton path passed through the patient's jaw and teeth. For these two angles tooth fillings will affect the range. Figure 4.16 illustrates the problem of tooth filling in both a kVCT image (left) and MVCT image (right). Though artefacts are not present in the MVCT, a small setup or motion error, in any direction other than the beam direction, will result in a large range error for a proton beam travelling through the filling due to the high density of the filling material. Another issue is that the calibration has not been made to include such high density material. In a clinical proton case beam angles would be chosen to avoid passing through the teeth with fillings or the teeth may be removed due to the risk these materials and the resulting artefacts can have on the proton range.

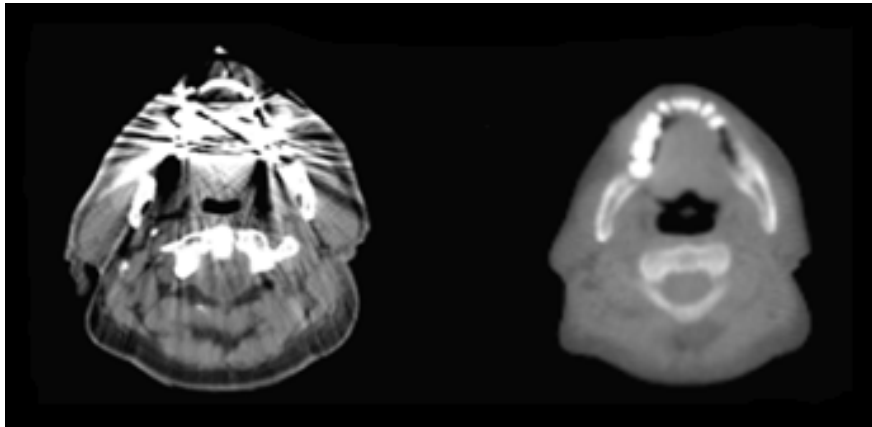


Fig. 4.16 Example of tooth filling artefact in kV CT image (left) and in MVCT image (right)

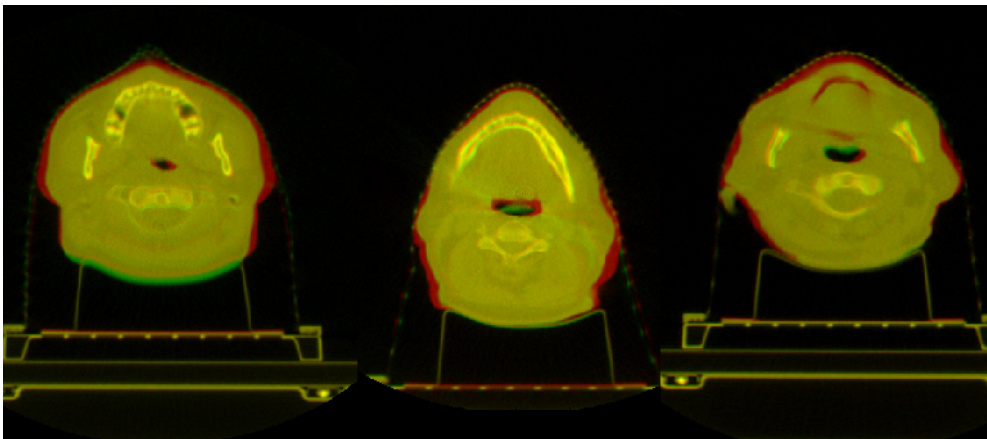


Fig. 4.17 Possible weight loss leading to negative Σ for Head and Neck. Images left to right of patients 52, 91, 92

The population results from the head and neck patient sample show range uncertainties from inter-fraction changes are smaller than that seen in the prostate data. The systematic inter-fraction range uncertainty was largest for prostate for 90° . The population data for head and neck across all angles had the smallest random range uncertainties. The random range uncertainty in the head and neck data is slightly smaller than that of the prostate. The density heterogeneities in the head and neck prove to be as challenging as range changes due to the target moving relative to bony anatomy in the prostate. The systematic range error in head and neck was also smaller than that of the prostate, and this was seen in the individual heat maps. The overall means for all population data was non-zero. In the head and neck this is believed to be potentially due to slight weight loss throughout treatment. Due to the limited number of patients used in this study and the number of fractions that could not be analysed for the prostate patients in particular it is expected that the values for Σ and σ are an overestimate. As well as carrying this work out with a larger patient sample, further work to provide suitable correction strategies for determining the systematic error would be to identify those errors unlikely to have occurred by chance and apply a correction as suggested by *Greener* (2003).

These results have highlighted a limitation in this method of using of IGRT images from conventional radiotherapy due to truncation of the region of interest due to changes in scanning length. This problem has led to a lot of the fractions being unusable. Daily TomoTherapy IGRT allows for online correction of inter-fraction geometric uncertainties. In this work these datasets have been used offline to quantify inter-fraction range uncertainties. In the case of this study the data sets are used in a way they were not intended for, and it is this reason that gives rise to their limitations for this work. For this type of data to be used for quantifying WEPL changes set protocols on patient set-up, imaging criteria and what constitutes as a volume of interest will be required. In a study carried out at Addenbrooke's by *Bates et al.* investigating IGRT imaging times using TomoTherapy, it was found that for every additional 1cm of scan length resulted in an extra 8 seconds to acquire at a slice thickness of 6mm and an extra 12 seconds to image match. Across a normal treatment day this would add an extra 6.7 minutes per day in imaging and matching (*Bates et al.*, 2013), which it was deemed implementable at Addenbrooke's for the use in IGRT studies. Another solution would be to extrapolate the missing data after the shifts are applied to the MVCT data and to keep this in consideration when analysing the data.

4.5 Conclusion

This work aimed to demonstrate how the use of daily imaging data sets from previously treated conventional radiotherapy patients could be used to quantify the random range uncertainty in the proton radiological path-length (WEPL) within the CTV caused by inter-fraction motion. Though limitations in the data sets exist, this method can be adjusted and solutions have been discussed to allow it to be suitable to investigating inter-fraction range uncertainty in proton therapy. The method has been used for two treatment sites and several beam angles. Further work will be to carry out such calculation using clinical beam arrangements and image guidance protocols. The same method can be applied to investigating range changes between CTV and OARs in the beam direction.

Based on these results for head and neck, assuming range uncertainty to be normally distributed, a $\Sigma = 3.4\text{mm}$ and a $\sigma = 4.7\text{mm}$ was calculated with an overall mean of -1.82mm . These values are representative of the residual range uncertainty still present after daily correction has been applied. For prostate, a $\Sigma = 5.64\text{mm}$ and a $\sigma = 5.91\text{mm}$ was calculated with an overall mean of 0.98mm . It is deemed that there was too few prostate images analysed to produce a non-biased determination of the population range uncertainty, however, a smaller range uncertainty is present for an anterior beam compared to a lateral beam direction. Measured data of this kind will support more sophisticated models for future studies allowing for limits on the actual magnitude of range uncertainty to derive more precise uncertainty models for specific tumour sites and planning protocols. These results show that inter-fraction range changes are not insignificant and therefore, should not be excluded from either the plan creation or plan analysis when considering robustness.

Chapter 5

Defining Robustness Protocols

The work in this chapter was carried out during a five month placement at the Proton Therapy Centre at the Paul Scherrer Institute in Villigen, Switzerland. The contents of this chapter, including tables and figures have been accepted for publication in *Physics in Medicine and Biology* on the 8th December 2014. The permission of my co-authors has been given to use the work here.

5.1 Introduction

Whether a plan has been created using margins or through a method of robust optimisation, analysis of a plan's robustness is required. Quantifying the uncertainty for given protocols will aid in setting limits on the amount of robustness needed. As a consequence, the aspect of robustness should be reflected in dose reporting protocols as to better represent the quality of the plan (*Unkelbach et al., 2007*). In this chapter plan robustness is retrospectively analysed for a sample of clinical plans. Using this information it is demonstrated how centre- and site-specific robustness constraints may be established for different volumes to aid making planning decisions. 3D IMPT offers the ability to deliver highly conformal radiotherapy to the patient, reducing integral normal tissue dose (*Chang et al., 2006*) and providing greater OAR sparing through the use of multiple inhomogeneous fields. However, without certainty in our ability to deliver these highly complex and conformal plans at each fraction caution must be heeded when choosing beam arrangements and positioning steep dose gradients near OARs (*Albertini et al., 2010; Lomax, 2008b; McGowan et al., 2013*). As mentioned, any uncertainty might lead to severe target underdose or OAR overdose. Several authors are proposing to include the plan robustness as an extra parameter directly during the optimisation process (*Chen et al., 2012; Fredriksson et al., 2011; Liu et al., 2012;*

Pflugfelder, 2008; Unkelbach et al., 2007). Unfortunately when introducing the robustness parameter into the optimisation algorithm, the nominal plan quality is often compromised (*Fredriksson et al., 2011; Unkelbach et al., 2007*). Improving plan plan robustness is clearly desirable and producing robust plans is probably the correct way to deal with the problem of uncertainties in IMPT. However, it should not be at the cost of compromising nominal plan quality to achieve robustness against very large and extremely unlikely uncertainties (*Unkelbach et al., 2007*). A thorough understanding of the magnitude and probability of uncertainties is required to ensure plan conformity is not being sacrificed unnecessarily. It is extremely important that the trade-off between plan conformity and plan robustness is thoroughly explored. Clinical experience so far has been achieved without considering the robustness of the plan. Although the importance of including robustness during the plan analysis is recognised, it is not yet clear how much the nominal dose distribution can be compromised without compromising the patient's treatment. The actual status is therefore that the robustness analysis is not yet fully included into the clinical plan evaluation phase. Currently no commercial planning system has a robustness evaluation module integrated and to the best of my knowledge, the research centres that have developed their own robustness analysis tools are not yet using them clinically to make decisions. It is therefore of paramount importance to find a way to introduce the robustness analysis into the clinical plan evaluation process, without compromising the nominal dosimetric plan quality. Specifically, site-specific robustness thresholds are needed to define a threshold between robustness and plan quality. It is important to establish the adequate level of robustness for each volume, both the target and OAR. In doing so, this can be used on one side as an input parameter during the robust optimisation process and on the other side as control parameter during the plan evaluation phase. The concept of a site-specific robustness database can indeed be used for both purposes.

5.1.1 Methods and Materials

In this chapter a method to define site specific robustness protocols is proposed based on retrospectively analysing the robustness to both range and set-up uncertainties for a sample of Chordoma and Chondrosarcoma plans. All plans were clinically acceptable and had been delivered in the last five years at the Paul Scherrer Institute (PSI). All plans were calculated using the in-house treatment planning system at PSI. The treatment planning system uses a pencil beam model to calculate absolute dose delivered to the patient (*Pedroni et al., 2005; Scheib and Pedroni, 1992*) and uses a quasi-Newton optimisation technique (*Lomax, 1999*).

The model parameters have been adjusted to fit the measured data, which takes into account range straggling, proton energy loss and the width of the initial energy spectrum. To take into account density heterogeneities in the patient, CT data is converted into water equivalent depth using a ray casting model (*Schaffner et al.*, 1999).

To determine plan robustness the set-up and range uncertainties were modelled using the method proposed by *Albertini et al.* (2011b) and later validated by *Casiraghi et al.* (2013). This method will be briefly described here.

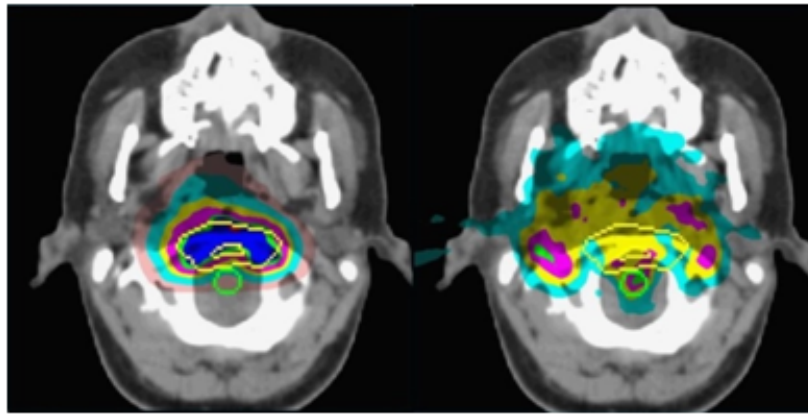


Fig. 5.1 The ebDD represents in each voxel a dose-error-bar that brackets the calculated deviations from the nominal dose distribution. Here are the screenshots of the nominal plan (using typical PSI beam arrangements referenced as $A(4f)$ in this chapter) and the ebDD calculated for $\pm 3\%$ HU from one patient.

Set-up Uncertainty: The effect of random set-up uncertainty on plan robustness was simulated by recalculating the nominal dose distribution on 14 isocentrically shifted CT data sets. The shifts used were applied along the major anatomical axes and their indices in both positive and negative directions (equivalent to the six faces and eight vertices of a cube) resulting in multiple spatially shifted dose distributions associated with each shifted CT data set. *Bolsi et al.* (2008) showed that the use of a remote patient positioning device reduced systematic set-up uncertainties to negligible values (below 0.6mm), whereas random set-up uncertainties of over 2mm can be observed, depending on tumour location and immobilisation device used. Using this data a three dimensional shift vector was calculated from the standard deviation of each shift in left-right (LR), anterior-posterior (AP) and cranium-caudal (CC) directions which represents of the radius of the spherical error-space used in this analysis. Following the same method as *Albertini et al.* (2011b) a shift of magnitude

equivalent to a confidence interval of 85% was applied. In particular shifts of $\pm 3.2\text{mm}$, $\pm 4.7\text{mm}$ were used for bite block and for head mask fixation devices respectively. The nominal dose distribution and each recalculated dose distribution are then combined into one *error-bar* dose distribution (ebDD) by storing in each voxel the difference between the maximum ($Max(D^i)$) and minimum ($Min(D^i)$) value for that corresponding voxel (i) from all the shifted plans and the nominal plan (nom). This amplitude of dose uncertainties, ΔD^i , in each voxel is calculated using formula 5.1, where D^i is the dose in voxel after each shift has been applied and *nom* refers to the nominal distribution. Each voxel stores a value which represents a dose-error-bar that brackets all the possible deviations from the nominal dose distribution that can be detected when patient shifts within an 85% confidence interval occur (Casiraghi et al., 2013).

$$\Delta D^i_{random} = Max(D^i_{+LR}, D^i_{-LR}, \dots, D^i_{-CC}, D^i_{nom}) - Min(D^i_{+LR}, D^i_{-LR}, \dots, D^i_{-CC}, D^i_{nom}) \quad (5.1)$$

Range Uncertainty: Radiotherapy plans are generally produced using a single CT data set of the patient and so any uncertainties in either the Hounsfield Units (HU), or their conversion to relative proton stopping power, will lead to a systematic uncertainty that will propagate throughout the treatment delivery (Lomax, 2008a). The effect of systematic range uncertainty on plan robustness was simulated by recalculating the nominal dose distribution on CT data with HUs altered by $\pm 3\%$, thus to simulate an overdose or an underdose scenario [Lomax 2008]. In this case the ebDD is calculated using formula 5.2, where D^i_{HU} refers to the dose at voxel i after a $\pm HU$ shift has been applied.

$$\Delta D^i_{systematic} = Max(D^i_{+HU}, D^i_{-HU}, D^i_{nom}) - Min(D^i_{+HU}, D^i_{-HU}, D^i_{nom}) \quad (5.2)$$

The robustness of each volume has been analysed by extracting the error-bar volume histogram (ebVH). The error-bar volume histogram represents a useful and simple tool to evaluate the quality of the treatment: the closer the histogram is to the ‘0-error’ line, the more robust the dose is to that specific uncertainty. In particular its similarity in presentation to the familiar dose volume histogram used conventionally in radiotherapy allows for easy integration into the planning process. Indeed several metrics can be defined and analysed as for example the maximum uncertainty, the mean uncertainty and the volume receiving an uncertainty of 3%, 5% and 10% ($V_{eb3\%}$, $V_{eb5\%}$, $V_{eb10\%}$).

There is a greater clinical relevance in displaying the potential over-dosage uncertainty

(highest minus nominal value) for the organ at risk and the under-dosage uncertainty (nominal minus lowest value) for the target volume, instead of the more general error-bar dose distribution discussed above, so this has been implemented when creating the database.

5.1.2 Retrospective Robustness Analysis

At PSI Chordomas and chondrosarcomas are treated to 74Gy(RBE) and 68Gy(RBE) respectively. Each treatment consists of three phases delivering a given proportion of the total prescribed dose to the target at each fraction. The first phase is generally comprised of a 3- field uniform dose distribution (SFUD) plan used to deliver up to 34-40Gy(RBE) of homogenous dose to the target volume. The only constraint within the SFUD plan optimisation is to deliver a homogeneous dose to the target volume. As a consequence, the resulting target coverage will be robust to uncertainties, but at the cost of some compromise of organs-at-risk (OARs) sparing (*Albertini et al.*, 2011b). The following two phases are comprised of 3D-Intensity Modulated Proton Therapy (IMPT) plans used to provide dose to the target whilst prioritising OAR sparing. The second phase then will bring the dose to the primary target up to 54Gy(RBE), sparing some critical structures. The third phase (bringing the dose up to 68 or 74Gy(RBE)) is delivered to a reduced target volume with the IMPT plan aiming to spare the critical structures. In all these cases, the PTV is symmetrically grown from the CTV by 5mm. The dose constraints are mainly defined for the brainstem (64Gy(RBE) on the surface, 53Gy(RBE) in the centre) and 60Gy(RBE) in the optical structures (*Ares et al.*, 2009). In the IMPT plans, all the fluences of all the fields are optimized simultaneously. Unlike SFUD treatments, IMPT can deliver a number of non-uniform fields to produce the desired dose distribution.

The standard 3D-IMPT beam arrangement used clinically at PSI for the skull-base is a four field beam arrangement and is illustrated in Figure 5.2. This beam arrangement consists of two posterior oblique beams and two lateral oblique beams. The IMPT plans retrospectively analysed in this study have been planned using these start conditions. For the purpose of this chapter this beam arrangement is referred to as the $A(4f)$ beam arrangement. For each IMPT phase, the plan robustness in the CTV for an underdose scenario was analysed for both types of uncertainty, as well as the overdose scenario in the brainstem and optical chiasm. Due to their proximity to the target, the dose constraints defined for the brainstem and for the optical chiasm tend to drive the optimisation outcome. The parameters measured include the mean and maximum dose uncertainties in the volume, the volume with an uncertainty of

3% and 5% ($V_{eb}3\%$ and $V_{eb}5\%$), and where these uncertainties occur in relation to anatomy and field direction. From this analysis a table of robustness parameters was created to aid planners in the selection between robustness and conformality.

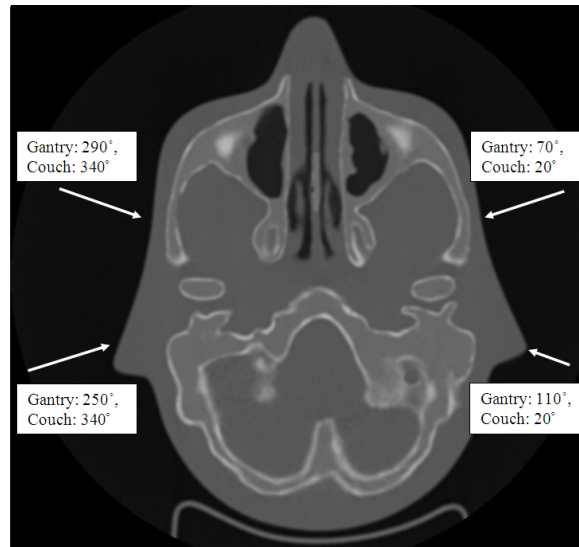


Fig. 5.2 The A(4f) plan consists of four non-coplanar fields, two posterior oblique and two anterior lateral oblique fields. Clockwise from top left the beam angles and couch twists used are (290°, 340°), (70°, 20°), (110°, 20°) and (250°, 340°), where the first angle is the gantry orientation and the second is the table orientation.

Example Case

To illustrate how the robustness table could be clinically used in practice, one plan was identified as an outlier. This plan was found to be un-robust in the brainstem compared to the sample. Due to the degeneracy associated with IMPT there exist many solutions to the given problem of ensuring target coverage whilst meeting dose and robustness constraints. Beyond changing the optimisation itself (*Chen et al.*, 2012; *Pflugfelder*, 2008; *Unkelbach et al.*, 2007), we can alter our starting conditions, such as number of beams and their orientation to obtain solutions to satisfy both dosimetric and robustness requirements. For this case, the plan was re-planned using four different beam arrangements. Four additional start arrangements were investigated to determine which would be more optimal for this patient, included B(4f), B(6f), A(6f) and C(4f) shown in Table 1 along with A(4f). Each plan was created with the aim of keeping the dosimetric quality of the plan in the OARs and target as similar to those achieved in the A(4f) plan so that the degeneracy of robustness to start conditions could be investigated.

Table 5.1 Descriptions of each plan

| Plan | No. fields | Beam arrangement |
|-------|------------|--|
| A(4f) | 4 | Two posterior oblique and two anterior lateral oblique |
| B(4f) | 4 | Two lateral and two posterior lateral oblique |
| A(6f) | 6 | Two posterior oblique, two anterior lateral oblique and two lateral fields |
| B(6f) | 6 | Two posterior oblique, two anterior lateral oblique and two posterior lateral obliques |
| C(4f) | 4 | Two lateral fields and two oblique fields all coplanar |

5.2 Results

5.2.1 Retrospective Robustness Analysis

Sixteen skull-base 3D IMPT plans, phase two and three, were retrospectively analysed in terms of robustness to systematic range and random set-up uncertainties. The volumes analysed were the brainstem, chiasm and the clinical target volume (CTV). The results are shown in Figure 5.3, where for each box plot the central mark is the median, the edges of the box are the 25th and 75th percentiles, the whiskers extend to the most extreme data points not considered outliers, and outliers are plotted individually. Outliers are considered points with a deviation more than $\pm 2.7\sigma$. From the box plots in Figure 5.3 it is seen that the impact of the random set-up error appears greater for an individual fraction than that resulting from the range uncertainty in all three volumes of interest (VOIs) for each parameter measured. It can also be seen that the mean and standard deviation in the range error was lower for the OARs than for the CTV; the opposite was true for the set-up uncertainty.

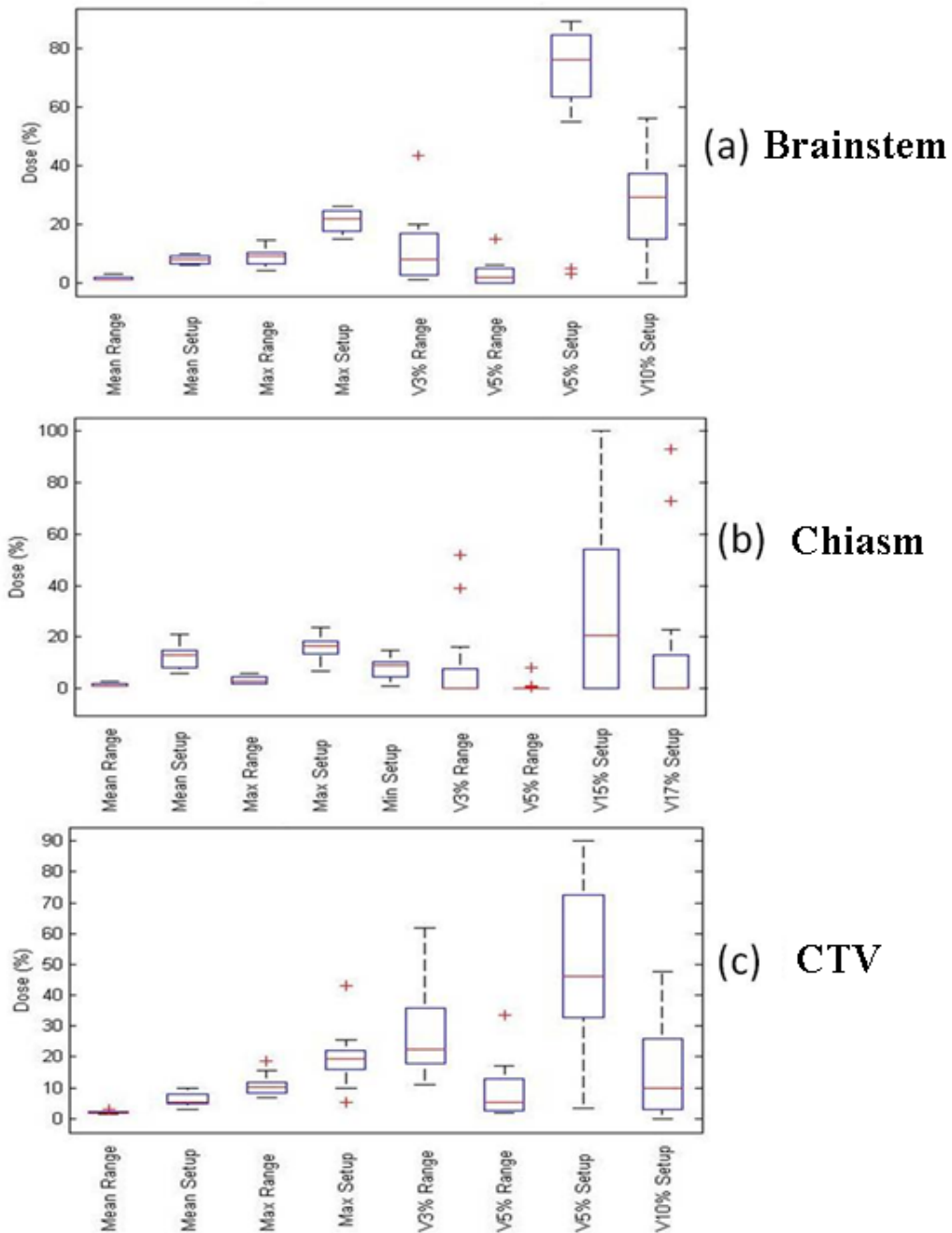


Fig. 5.3 Robustness results, represented as percentage dose uncertainty for 16 skull-base IMPT plans from 8 patients to both the range and set-up uncertainties modelled in (a) in the brainstem, (b) in the chiasm and (c) in the CTV. On each box plot the central mark is the median, the edges of the box are the 25th and 75th percentiles, the whiskers extend to the most extreme data points not considered outliers, and outliers are plotted individually. Outliers are considered points $\pm 2.7\sigma$.

From these results an example of a robustness database for 3D IMPT skull-base plans case has been generated (Table 5.2). This table can be used to aid planners in visualising the magnitude of effect that range and set-up uncertainties can have on patient treatment in terms of percentage change from the nominal dose. The ranges represent the deviation from the nominal dose in that volume caused by the uncertainty for this patient sample. The values correspond to the 25th -75th percentiles as seen in the box plots in figure 5.3 for an over-dosage scenario to OAR and under-dosage scenario to the CTV. The lower limits are included to allow the planner to see where a compromise between conformality and robustness can be made.

Table 5.2 The use of retrospective plan analysis to establish planning parameters of robustness

| VOI | Mean range | Mean setup | $V_{eb}3\%$ Range | $V_{eb}5\%$ Range | $V_{eb}5\%$ Setup | $V_{eb}10\%$ Setup |
|-----------|------------|------------|-------------------|-------------------|--------------------------|-------------------------|
| Brainstem | 1-2% | 6.5-9% | 2.5-17% | 5% | 63-85% | 15-37.5% |
| Chiasm | 1-1.5% | 8-15% | <5% | 0% | ($V_{eb}15\%$) <50% | ($V_{eb}17\%$) <4% |
| CTV | 1.5-2.5% | 5-8% | 17.5-28% | 2.5-11.5% | 32.5-72.5% | 3-25.8% |

5.2.2 How to use the Robustness Database in Practice

To illustrate how the robustness database could be clinically used in practice a clinical case is discussed. For patient X a nominal plan was generated and the robustness to set-up and range uncertainties was calculated and compared to the robustness database table. If the robustness of plan X is within the defined values, the nominal plan is delivered. In contrast, if plan X has a robustness outside the database range for a given set of parameters for one or more volumes, the nominal plan has to be improved in terms of its robustness before delivering it to the patient. Or in the case where robustness is better than expected from the database it must be assured that plan conformality is not being compromised.

Of the plans retrospectively analysed, one plan was shown to have a worse robustness in the brainstem compared to the sample. In particular, this plan had a potential mean range, $V_{eb}3\%$ and $V_{eb}5\%$ uncertainty in the brainstem of 3.9%, 43.5% and 15% respectively (compared to 1-2%, 2.5-17% and 5% in the database in Table 5.2). The possibility of improving the plan

robustness, without using robust optimisation, but by changing the start conditions of the plan has been investigated. While ensuring plan quality was maintained, the field setup was changed to create four dosimetrically equivalent plans. For each new plan, the robustness and conformality of the CTV and each OAR, considered during the optimisation process, were analysed using the error-bar dose histogram and by retrieving the robustness values for both the range and setup uncertainty from these (see Tables 5.3 and 5.4).

The error-bar dose histograms in the CTV for each plan created for this patient are shown in Figure 5.4. The numbers in the plot key refers to the size of the area under each curve (the smaller the area, the greater the robustness). The B(4f) plan in Figure 5.4(a) shows worse robustness in the CTV than the other plans. A comparison between the B(4f) and A(4f) nominal and error-bar dose distributions are shown in Figure 5.5. The B(4f) plan in Figure 5.4(a) shows worse robustness in the CTV than the other plans. A comparison between the B(4f) and A(4f) nominal and error-bar dose distributions are shown in Figure 5.4(c). The B(4f) plan produces an underdose uncertainty to a larger volume of the target than the A(4f) plan. Table 5.3, shows that despite B(4f) having the worst plan robustness it only fails one robustness constraint, the mean range uncertainty which is 2.8% for the B(4f) plan compared to 2.1% for the A(4f) plan. The constraint set in Table 5.2 was 1.5-2.5%. Figure 5.4(b) shows the volume histograms from the set-up uncertainty, A(4f) is the most robust plan, though plan B(4f) is within the robustness constraints in Table 5.3. The C(4f) plan shows to be the most robust plan to range uncertainties, though it is the least robust plan to set-up uncertainties.

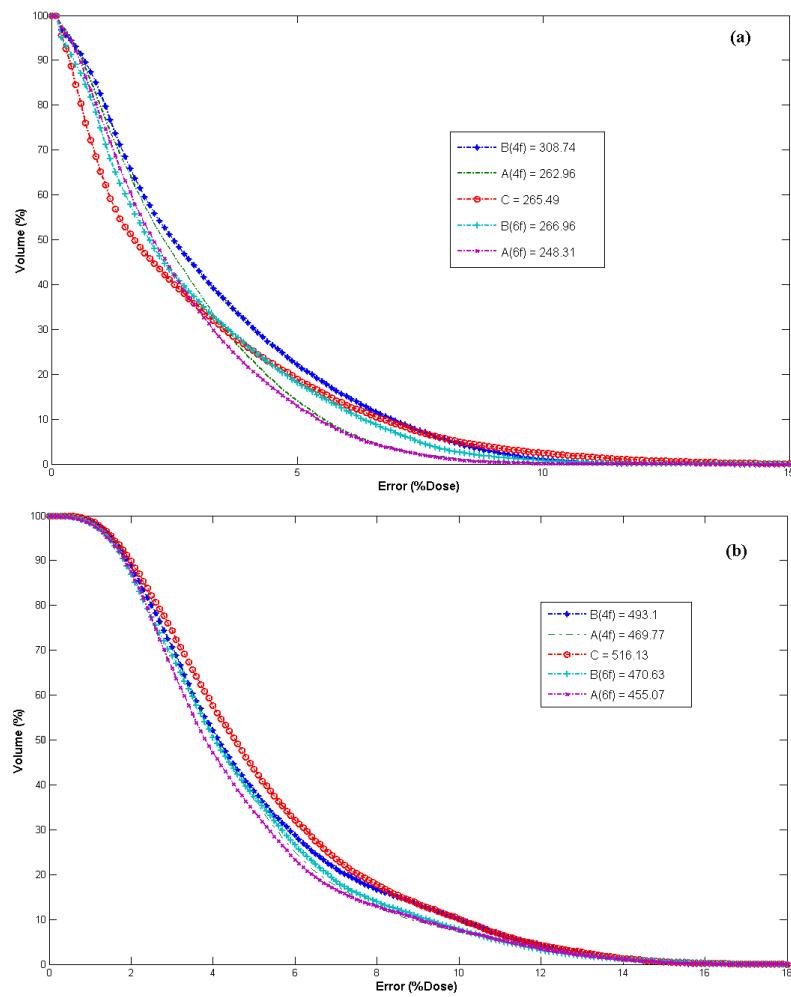


Fig. 5.4 Volume Histogram of (a) systematic range uncertainties and (b) random set-up uncertainties for an underdose scenario in the CTV for five plans of different beam orientations.

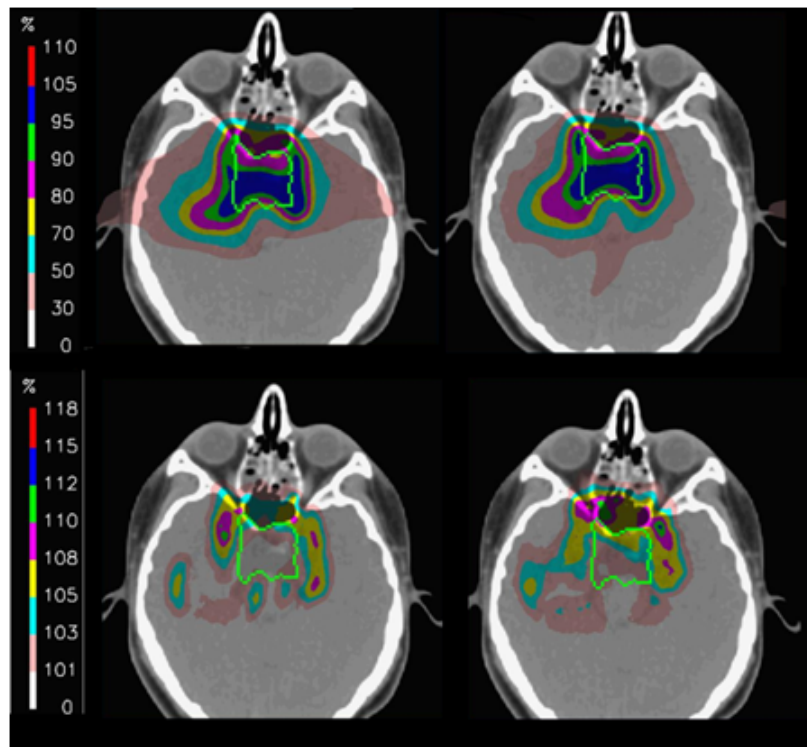


Fig. 5.5 Dose distribution for the A(4f) (top left) and B(4f) (top right) plans and ebDD of systematic range uncertainties for the worst-case underdose scenario for the A(4f) (bottom left) and B(4f)(bottom right) treatment plans showing the CTV in green.

Figure 5.7(a) shows the volume histograms of error-bars from range uncertainties in the brainstem from all plans. The A(4f) plan is least robust to range uncertainties, as discussed in the previous section of these results. Figure 5.6 shows the difference in ebDD between the B(4f) and A(4f) plans indicating the greater uncertainty in the brainstem on the A(4f) plan. Figure 5.7(c) is included to show how the plans are affected by random set-up uncertainties, especially the C(4f) plan which shows a decrease in robustness when compared the other four beam arrangements for this type of uncertainty. As seen in the A(4f) plan there is a hot spot in the centre of the brainstem, whereas in the B(4f) the hot spot is shifted more anteriorly due to the direction of the lateral and posterior beams. Despite this improvement in robustness in the brainstem to range uncertainties, the B(4f) plan is less robust in the chiasm (Figure 5.7(c)) compared to the A(4f), whereas the B(6f) yields the greatest robustness to range uncertainties in the chiasm of all the plans. In the case of the optic nerves again the B(4f) plan is less robust compared to the A(4f), but this time the A(6f) plan is most robust. These results can also be seen in Table 5.3; the chiasm fails a robustness constraint with a V3% range uncertainty of 23%, though this uncertainty in dose has fallen to 1.4% at V5%, matching that achieved by the A(4f) plan. Table 5.4 has been included to show the results for four of the plans for other OARS, though constraints for these volumes have not been established currently.

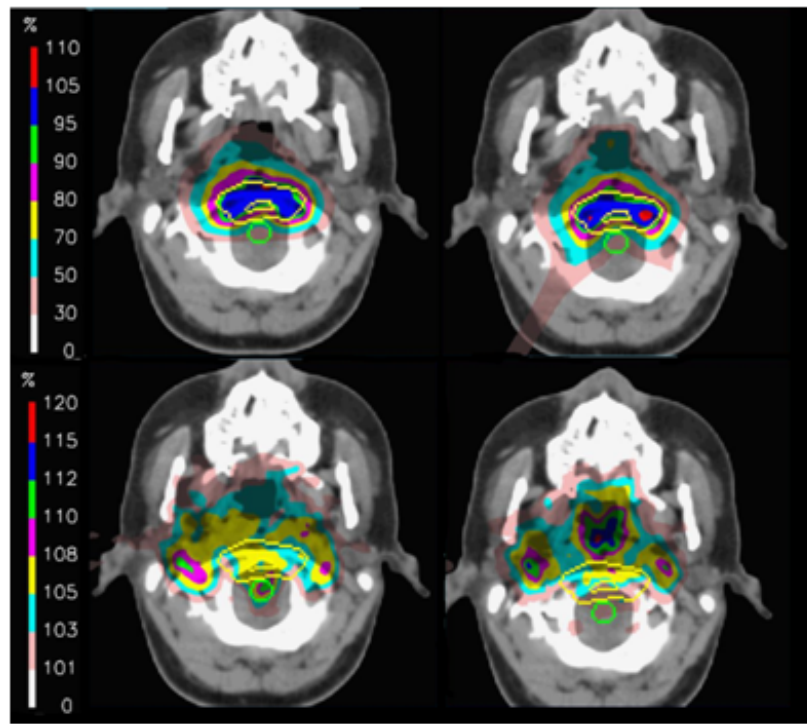


Fig. 5.6 Dose distributions from the A(4f) (top left) and B(4f) (top right) plans and the corresponding ebDD from B(4f) (bottom left) and A(4f) (bottom right) treatment plans showing the brainstem in green and the target in yellow.

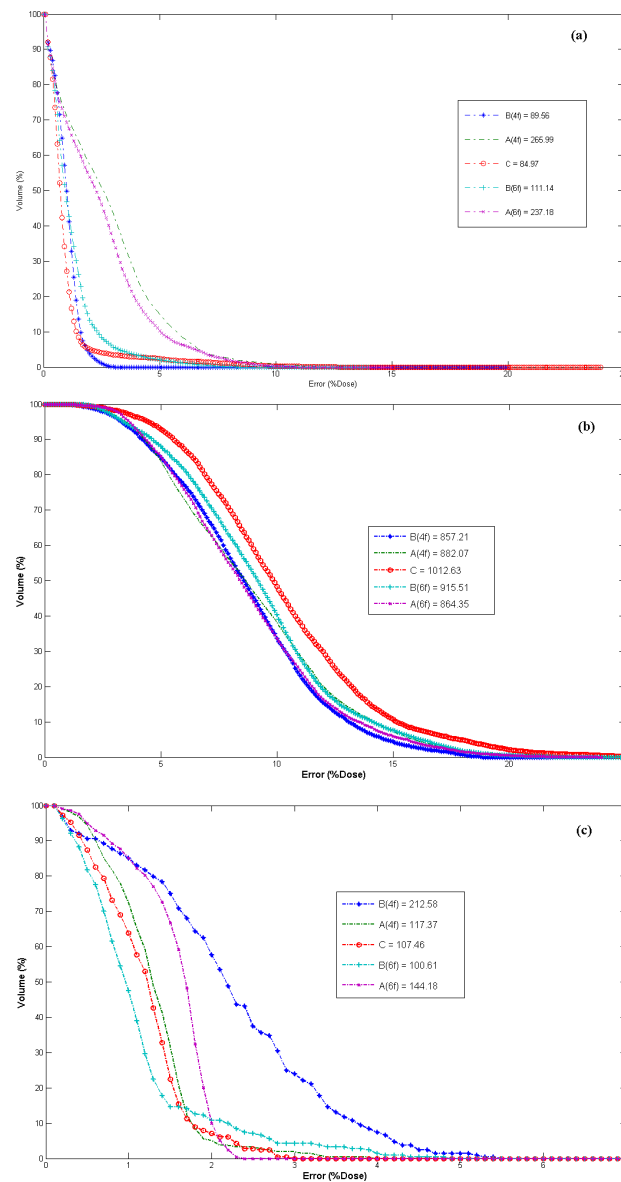


Fig. 5.7 Volume histogram of (a) the systematic range uncertainties, (b) the random set-up uncertainties for an overdose scenario in the brainstem and (c) the random set-up uncertainties for overdose scenario in the chiasm, for five plans of different beam orientations.

Table 5.3 Robustness values for each parameter set in the site specific robustness database in Table 5.2 for plans A(4f) and B(4f). Bold italic values are those that are out of tolerance

| VOI | Mean range | Mean setup | $V_{eb}3\%$ Range | $V_{eb}5\%$ Range | $V_{eb}5\%$ Setup | $V_{eb}10\%$ Setup |
|-----------------|---------------|---------------|----------------------|----------------------|----------------------|-----------------------|
| A(4f) Brainstem | 3.9% | 9% | 43.5% | 15% | 84% | 38% |
| B(4f) Brainstem | 1.1% | 8.7% | 1.1% | 1.1% | 85% | 33.5% |
| A(4f) Chiasm | 1.4% | 6% | 2% | 3.9% | 1.8% | 0% |
| B(4f) Chiasm | 2.4% | 8.7% | 23% | 1.4% | 4% | 0% |
| A(4f) CTV | 2.1% | 5.2% | 16.5% | 3% | 36.5% | 7% |
| B(4f) CTV | 2.8% | 5.3% | 26% | 8.5% | 38% | 10% |

Table 5.4 This table shows robustness results from the original A(4f) plan that patient X was treated with and those from the re-plan created for this work B(4f). Tolerances have not been set for these OARs as they had for the brainstem and chiasm in the robustness database, but they have been supplied here to use to further compare plans.

| VOI Beams | Mean range | Mean setup | $V_{eb}3\%$ Range | $V_{eb}5\%$ Range | $V_{eb}5\%$ Setup | $V_{eb}10\%$ Setup |
|---------------------------|---------------|---------------|----------------------|----------------------|----------------------|-----------------------|
| <u>Cochlea</u> | | | | | | |
| B(4f) | 4 | 6.8 | 64.2 | 32.1 | 68.2 | 5.5 |
| A(4f) | 3.8 | 4 | 84.4 | 24.8 | 20.2 | 1.8 |
| B(6f) | 3.7 | 5.8 | 57.8 | 22.9 | 75.2 | 1.8 |
| A(6f) | 3.9 | 3.4 | 75.2 | 24.8 | 10.1 | 1.8 |
| <u>Left Optic Nerve</u> | | | | | | |
| B(4f) | 3.8 | 5.8 | 36 | 19 | 47 | 14.2 |
| A(4f) | 3.8 | 5.8 | 36 | 19 | 47 | 14.2 |
| B(6f) | 4.4 | 4.9 | 23.7 | 8.3 | 38.3 | 14.2 |
| A(6f) | 2.1 | 5.8 | 9.5 | 1.2 | 47.5 | 12.5 |
| <u>Left Temporal Lobe</u> | | | | | | |
| B(4f) | 4.2 | 4.3 | 15.3 | 10.6 | 19.1 | 4.8 |
| A(4f) | 3 | 3.8 | 11.4 | 6.8 | 12.9 | 2 |
| B(6f) | 3.2 | 3.8 | 11.7 | 7.2 | 15.3 | 2.6 |
| A(6f) | 3.1 | 4 | 12.5 | 7.8 | 16.5 | 2.1 |

5.3 Discussion

In this work it has been demonstrated how retrospective analysis of the robustness of clinical plans at PSI has furthered an understanding of how random set-up and systematic range uncertainties affect the final dose distribution. It was seen that random set-up uncertainties resulted in a greater difference in the resulting dose distribution than that from systematic range uncertainties. Despite this, systematic range uncertainties pose a greater concern due to their systematic origin meaning they are present over the entire treatment leading to a cumulative ‘shift’ of the dose distribution. In contrast, set-up uncertainties are random and act instead to ‘blur’ the final dose distribution; therefore, the risk of reduced plan quality associated with these uncertainties is less. This analysis assumes that systematic set-up uncertainties are negligible. This is the case where a remote patient position device (*Bolsi et al.*, 2008) is used, but might not be true in centres using other set-up techniques. It can, however, be identified and corrected with the use of image guidance techniques. The mean values seen in the sample data show that the brainstem, chiasm and CTV appear to be robust to the systematic range uncertainty with values of around 2% of the planned dose. Of these volumes the target is the least robust to systematic range uncertainties. In the 3D IMPT optimisation OAR sparing has a higher priority over target coverage. This can lead to individual fields showing steep dose gradients within or near to the target which can result in a greater ebDD for both range and set-up uncertainties. Through retrospectively analysing the robustness of each VOI a site specific robustness database was established (Table 5.2). It has been shown how the database can be used to easily identify patients that require a more individualized plan to improve the robustness to uncertainties. In this case patient X may have benefited from the B(4f) plan in regard to reducing range uncertainty in the brainstem. Though for this beam arrangement there was a higher risk of range overdose in the chiasm, this was outweighed by the improvement to the brainstem robustness and did not sacrifice target robustness or plan conformality.

Although the defined database is specific to PSI, the idea can be used as an example for other centres to define, for the moment, their own robustness parameters. Hopefully, with more centres starting to introduce the robustness evaluation in the clinical process, we will be able in the future to define an adequate level of robustness for each volume that is accepted worldwide, in the same way as dose-volume-constraints to organs-at-risk and prescribed dose to target volumes are generally widely accepted and applied in the different protocols.

Chapter 6

Summary

6.1 Discussions

Advances in radiotherapy, such as IMRT and IGRT, have meant that we are capable of creating and delivering highly sophisticated, and often individualised, treatment plans for many cancer sites. These advancements are the direct result of improved technology, increased computational power, access to published guidelines and recommendations, and also to an extent, due to clinical experience. Theoretically, protons offer an even greater benefit for radiotherapy patients, offering improved local tumour control and prevention or reduction of radiation-induced side effects (*Langendijk et al.*, 2013). As treatments progressively move towards individualised care, balancing cost effectiveness and patient throughput is an important factor for a health service. Within England and the NHS there is a far greater experience treating with photons in all aspects of the patient pathway. As well as prescribing and planning itself, this also includes aspects such as carrying out patient specific quality assurance. The greater experience and the technological advances in conventional radiotherapy will mean for many patients protons will not necessarily be the optimal treatment decision. Determining and prioritising indications for patient selection, to take into account the limited capacity and high costs of proton therapy is an important challenge for NHS England (*Crellin and Burnet*, 2014). Patients are currently selected based on the results from dosimetric and observational studies, clinical trials, and models predicting reduced side effects to ensure those treated are deemed to benefit the most (*Langendijk et al.*, 2013). Other challenges include establishing protocols for ensuring plan robustness and training staff in proton therapy planning and delivery.

Optimisation in radiotherapy is a multi-parameter problem. The choice in optimisation

criteria and starting conditions can affect the resultant plan quality, both in its conformity and robustness. The challenge of ensuring that plans are robust to range uncertainties in proton therapy remains. There remains a need for established protocols for proton treatment in the clinic for the English centres, in the same way that there already exists in conventional radiotherapy. It has been to this end that this thesis has been carried out. Firstly, a method of using daily IGRT to quantify changes in WEPL from inter-fraction motion has been explored and demonstrated for several cancer sites. The quantification of uncertainties is necessary in creating CTV-PTV (or beam specific) margins or as input into a form of robust optimisation. Secondly, a method of robustness analysis has been described which can be used with either PTV-based or robustly optimised plans. In this case by retrospectively analysing plans a database of planning robustness objectives has been generated to ensure that for each individual patient the optimal treatment is delivered.

Quantifying Random Range Uncertainty

The most significant limitations in calculating inter-fraction range uncertainty in this dissertation were from calibrating the TomoTherapy MVCT scanner and truncation in the imaging data. Established proton centres such as Orsay, PSI and MD Anderson have been able to sufficiently calibrate their TomoTherapy MVCT scanners using a stoichiometric calibration, so these challenges would not limit other centres from using MVCT for range calculation. At MD Anderson it was found that deviations between individual HU values and the fitted calibration curve were smaller for the MVCT scanner, particularly within soft-tissue ranges compared to that for the kVCT calibration. These results suggest that MVCT images may be as accurate as kVCT images in calculating proton range (*Newhauser et al.*, 2008), though more research is required. If a centre were to adopt this approach of using MVCT to analyse range uncertainty, calibrations would need to be carried out routinely. When analysing a patient data set, the appropriate calibration must be applied. Site specific imaging protocols would need to be established by widening or choosing certain slices to image on the patient to avoid ROI truncation (*Bates et al.*, 2013). Keeping the number of slices similar may also be helpful, though not essential. The concomitant doses have been discussed in Chapter 3. The concomitant dose is relatively small in comparison to the treatment, yet still requires consideration and patient consent.

Despite these limitations the data collected in Chapter 4 from the head and neck patients was useable for all seven patients. Though analysis of the prostate was carried out, significant

numbers of fractions were missing. Missing fractions leads to an over estimate of the range uncertainty for the sample (*Greener, 2003*). From the head and neck data a mean of -1.82mm, a Σ of 3.39mm and a σ of 4.72mm was calculated for the patient sample across all beam angles. For this method to be used clinically to produce uncertainty models to use at either plan optimisation or evaluation a larger number of patients as well as clinical beam angles need to be used.

The concept of deducing probability distributions of uncertainties from daily IGRT to be used to re-optimize patient treatment is not new and has the potential to improve both TCP and normal tissue sparing (*Birkner et al., 2003*). *Birkner et al. (2003)* re-optimized patient treatment plans part way through treatment by including patient specific information from portal images into the adaptive planning process. *Unkelbach and Oelfke (2005)* investigated the same problem and used the information from daily IGRT of the first fractions to establish probability distributions to be used in probabilistic IMRT plans. They found the greatest limitation was the small number of images acquired to deduce the distribution. The novelty of the work presented in this thesis is that the images have been acquired *every* day, and analysed not to change that specific patient's optimisation, but by collecting this data for many patients with the same target sites so that probability distributions are acquired representative of that population. This knowledge can prevent situations where plan conformity may be sacrificed unnecessarily to ensure plan robustness to large or unlikely errors (*Unkelbach et al., 2007*).

Part of the conclusion from the Gordon 2010 paper highlights the importance in setting the objectives and constraints, both in terms of dose and the probability of that dose being received by that voxel. This paper found that their robustness algorithm for producing photon plans produced better plans than standard PTV-based plans. However, only in that optimised plans exploited 'slack' in OAR doses, i.e., cases where OAR doses were below their optimisation limits, to increase target coverage (*Gordon et al., 2010*). This is an example of when target coverage has been prioritised over OAR sparing. Specifically, because the optimized plans were not constrained by a predefined PTV, they were able to provide wider dosimetric margins around the CTV, by pushing OAR doses up to, but not beyond, their optimisation limits (*Gordon et al., 2010*). For such optimisation, it is imperative constraints and objectives are clearly predefined prior to optimisation. The power of optimisation algorithm will exploit any incoherence in the objective request. Unlike the planner, the algorithm will not know what the doctor intended, just what has been asked of it.

Further work includes investigating how the WEPL between the distal edge of the target and the proximal edge of an OAR in the beam direction as well as increasing patient numbers in the samples and choosing clinical beam arrangements.

Evaluating Robustness

Beyond the ability to determine the nature of uncertainties from a patient sample and then create treatment plans robust to these uncertainties for a given percentage of treatments, there still exists the problem in how to define what is robust enough. Due to the degeneracy in the inverse optimisation problem many optimal plans may be generated. The use of a Pareto navigation surface (*Chen et al., 2012*) serves as an ideal way for the planner, whether oncologist, physicist or dosimetrist, to gain experience and an ‘intuition’ for proton planning that they may already have in conventional radiotherapy planning. When using MCO consideration for the balance between the computationally heavy option of calculating many plans or interpolating between a small number of plans along the Pareto surface is required, as well as an awareness of how plans on the surface are generated (*Breedveld et al., 2007*). A principal advantage of probabilistic treatment planning is that it removes the need for artificial planning volumes such as a PTV or PRV. This allows the treatment planner to deal directly with dose distributions and metrics that incorporate the effects of uncertainties (*Gordon et al., 2010*).

Choosing the specific plan to deliver relies on qualitative plan analysis, which may be subject to the planner’s experience. In chapter 5 I have sought for a quantitative method for choosing a plan when balancing robustness and conformity, as is the crux in the multi-criteria problem. The error-bar Dose Distribution (ebDD) was used to analyse plan robustness to both systematic range and random set-up uncertainties for 16 skull-base IMPT plans previously treated at PSI for 8 patients. A site-specific robustness database was created as a simple solution to include robustness into the plan analysis. Such a database will also aid planners to produce plans to meet both dosimetric and robustness criteria by establishing site-specific robustness thresholds for individual volumes. Using these methods further work can be carried out to fully explore how start conditions, and the optimisation itself, affect both the plan robustness and conformity. This will further our ability to determine where a trade-off can be made between these two parameters to ensure the patient receives as optimal treatment as possible.

This quantitative method also serves as an attractive option to use in the clinic due to the

similarity of the ebDVH, proposed by *Albertini et al.* (2011b), and robustness objectives when compared with the familiar DVH and dose constraints used routinely in conventional radiotherapy. Many patients have already been treated with actively scanned protons, so using data from these patients through retrospective analysis will allow for continually updating practices and therefore, continually improving practices. So far only a few centres worldwide are performing a robustness analysis and, to the best of my knowledge, no-one is using this information clinically. Additionally every centre is performing the plan robustness analysis differently, for example by looking at the error bars, at the standard deviation, or at the width of the DVHs. With the introduction of the robustness database as laid out in Chapter 5 it is hoped that more centres will soon start to analyse and report plan robustness uniformly. The ultimate goal to be able to define in the future a reference value for the plan robustness for individual target sites and for specific OARs. In chapter 5 it was demonstrated how, even using a small patient sample, an outlier was identified as lacking in plan robustness when compared to the sample group. All of the plans in this study were clinically acceptable plans and had been delivered to the patients. The clinical results at PSI achieved for patients treated intra-cranially for chordoma and chondrosarcomas had a five year local control of 81% for chordomas and of 94% for chondrosarcomas with only limited toxicities (*Ares et al.*, 2009). Plan robustness for these patients had only been retrospectively analysed; consequently the plan conformity of these plans had never been altered in favour to a more robust plan. Without employing optimisation techniques, a plan using different start conditions could be created that satisfied this specific patient's need for a plan of greater individualisation. The use of a database is envisioned to be implemented alongside the use of robust optimisation techniques to use as part of the planning workflow. The database offers a novel tool to evaluate plan robustness as well as providing feedback that could be used to alter robustness constraints at optimisation itself. One of the challenges of using any robust optimisation is to find a threshold between robustness and nominal plan quality. It is hoped that using the database to collect and analyse data from all patients treated, for many sites, will help to find the threshold.

Further work will be to include random range uncertainty into the ebDD model and to analyse plans that have been created using a robust optimisation as well as margin based plans.

A final point is that there exist many optimisation algorithms in inverse planning and within both probabilistic planning and robust optimisation themselves. These algorithms have not

been a topic of this work, nor has it been to investigate how exactly systematic and random errors in proton therapy are weighted relatively at optimisation. It was seen in Chapter 5 how random range uncertainty had a greater effect on the individual fraction dose compared to the systematic set-up uncertainty. However, over the course of the entire treatment the systematic uncertainty would have a cumulative effect. Due to the directional nature of range uncertainty it is imagined that the position of a voxel relative to the beam direction should affect how the optimisation is driven.

6.2 MVCT and Proton Therapy

Practises used in conventional radiotherapy, such as IGRT and adaptive planning are also required for proton therapy. Accurate set-up is essential in radiotherapy, and even more so in proton therapy due to the element of range. Each centre may use other methods of IGRT, for example PSI uses in room CT scanner on rails, performing scout scans rather than a full CT scan. The first proton specific commercial CBCT went clinical at Penn Medicine in September 2014 (*iba: proton therapy*, 2014). CBCT is becoming routine in IMRT delivery in the UK, as it is worldwide. This development in proton therapy can be seen as delayed and highlights the important discrepancy between what can be achieved in the research setting for protons and the clinical one. The methods of range calculation described in this dissertation could be applied using either MVCT or CBCT. Dose re-computation using CBCT in conventional radiotherapy have been discussed in *Murray et al.* (2014); *Onozato et al.* (2014). In using CBCT to perform dose re-computation for adaptive radiotherapy these studies require pixels in the CBCT to be modified into a small number of ranges. Using masks for HUs is required due to instability of CBCT HUs. These methods may be suitable for conventional radiotherapy, but currently CBCT is not adequate for proton dose re-computation or for calculating WEPL.

In conventional radiotherapy daily MVCT allows, firstly for registration to the planning kVCT so that online patient position correction may be applied (reducing dosimetric affects from inter-fraction changes and systematic set-up error) and secondly, the daily MVCT may be used to assess anatomical changes and the dosimetric implications (*Langen et al.*, 2005). This latter application is paramount to evaluate the necessity of adapting the treatment at some point. This will allow for compensation of dose errors due to anatomical deformations and changes (*Langen et al.*, 2005). In this dissertation changes in range in the CTV between fractions has been calculation from daily MVCT images. As discussed the MVCT

calibration poses as a significant barrier for such practices as dose recalculation. Solutions may include creating a planning MVCT at the same time as the planning kVCT and calculating dose on both modalities. This would be so that the MVCT doses may be used, not to plan treatment delivery, but to carry out dose analysis on daily MVCT images. There are two methods in conventional radiotherapy to determine the dose distribution based on daily MVCT. One method is dose re-computation using exit dose from the treatment itself and recalculating it on the MVCT. The other is to recalculate the planned dose distribution onto the MVCT. Obviously, exit proton dose calculation is not an option using MVCT. However the dose delivered can be recomputed from the proton steering files and from the gantry itself (*Meiers et al.*, 2014). Recalculating the recomputed distribution onto the planning CT acts as treatment verification, but by recalculating it onto daily volumetric image would allow the opportunity to analyse treatment delivery at each fraction and for re-planning to take place as and when required.

Another potential benefit for using MVCT is in the case where metal implants are in or near the target site. Metal can cause dose calculation difficulties, as accurate patient dose relies on CT HU. Uncertainties arise both due to the high atomic number in metal causing calibration uncertainty and due to the artefacts in the planning kVCT. The sharp density interface also affects dose homogeneity as well as there being an increased range uncertainty caused by motion when the proton beam passes through or near metal. Patients treated with tumours along the spinal axis may often be referred for radiotherapy after surgery. When vertebrae have been removed titanium implants are used to stabilise the spine. Prostate or pelvic patients may be referred for radiotherapy with metal hip prosthesis and currently patients with dental fillings may require these teeth to be removed prior to proton therapy, or beam directions avoiding the teeth are chosen. *Rutz et al.* (2007) and *Staab et al.* (2011) followed 40 patients treated for extra-cranial chordoma and chondrosarcoma between 1999 and 2006 at PSI. Twelve of the thirteen local failures observed in this patient sample occurred when stabilising implants were present. The presence of implants was a significant risk factor ($P < 0.01$) for local failure. *Dietlicher et al.* (2014) states that whether there is a clinical reason for this risk, the presence of metal causes challenges in radiotherapy treatment, and even more so in proton therapy. This group then went on to investigate the effectiveness of their artefact correction technique using an anthropomorphic phantom to reproduce calculations of an *in vivo* measurement. The results from this paper suggest the poor survival for patients with metal may not be due to the limitations of dose calculation alone, but due to the aggressiveness of the local tumour for this patient group. Their results also reinforce a need for

multiple fields in proton therapy as individual fields showed a worse gamma analysis, with actual measured differences in dose up to -17.9% behind metal. The authors suggest there is still a need for an improvement in artefact correction at treatment planning. *Newhauser et al.* (2008) investigated using an MVCT and kVCT hybrid scan at planning to avoid the need to correcting metal streaking and saturation artefacts. In addition to avoiding streak artefacts, the MV-based approach yields advantages related to its greater dynamic range (i.e. higher saturation threshold) of relative linear stopping power values than that of kV scanning. Specifically, MVCT avoids saturation effects, enabling more accurate delineation of the metal implant and thus theoretically enabling quantitative identification of the implant material. This hybrid scan method offers a step towards reducing the subjectivity and manual labour associated with correcting for implant-induced artefacts (*Newhauser et al.*, 2008). However, further comparison with streak-resistant kVCT reconstruction algorithms (*McLean*, 2000; *Yazdi et al.*, 2005) and proton CT (*Sadrozinski et al.*, 2004) is needed

Furthermore, the use of DECT has been proposed by several groups to determine stopping power ratios with greater accuracy (*Bourque et al.*, 2014). The kV-MV combination makes the DECT method more robust in resolving the effective atomic numbers for biological tissues than the traditional kV-kV DECT method (*Yang et al.*, 2011). Despite improvements MVCT does produce uncertainties in stopping power ratios due to CT number uncertainties and artefacts such as imaging noise, scatter and beam hardening effects.

6.3 Conclusion

In this dissertation the need and decisions behind establishing proton therapy in England for NHS patients have been introduced, as have the concepts and benefits of this treatment option. In chapter 2 the state of the current literature at the time of this work has been presented and critically analysed. The following chapters describe the methods, results and discussions of the subsequent work following analysis of the literature.

The importance of understanding and quantifying range uncertainty in proton therapy has been thoroughly established and the need to quantify uncertainties to use as input into robust optimisation has been stated. Two methods of analysis have been presented that can aid in providing this information, namely through the use of IGRT, and by retrospective plan analysis. Novel work has been carried out using daily MVCT data to produce probability distributions of range uncertainty from inter-fraction motion. This knowledge is necessary for accurate proton treatment planning.

Currently no established robustness protocols exist in proton therapy in the same way that they do in conventional radiotherapy. Through analysing previously delivered proton plans a database of plan robustness for different ROIs may be established. This type of database may be used within the planning workflow as part of the plan analysis or as another method for acquiring prior information required for probabilistic/robust planning.

The two proposed English centres, together with an additional centre recently announced at Oxford (*University of Oxford*, 2014), offer the ability for the UK to make advancements in this relatively new field of radiotherapy treatment. Further work is needed to bring IGRT and ART in the clinical setting up to date with that which is already achieved in most state of the art conventional radiotherapy centres. I believe there is a place for MVCT in proton therapy, whether it is used for daily correction, dose difference analysis, DECT or for the study of range uncertainty for different tumour sites and beam orientations. It is also essential that methods for including uncertainties and evaluating plan robustness to these uncertainties (without the use of a PTV) are established and become integrated into the treatment planning workflow.

References

- Albertini, F., Planning and optimizing treatment plans for actively scanned proton therapy: evaluating and estimating the effect of uncertainties., Ph.D. thesis, 2011.
- Albertini, F., E. B. Hug, and a. J. Lomax, The influence of the optimization starting conditions on the robustness of intensity-modulated proton therapy plans., *Physics in medicine and biology*, 55(10), 2863–78, doi:10.1088/0031-9155/55/10/005, 2010.
- Albertini, F., M. Casiraghi, S. Lorentini, B. Rombi, and a. J. Lomax, Experimental verification of IMPT treatment plans in an anthropomorphic phantom in the presence of delivery uncertainties., *Physics in medicine and biology*, 56(14), 4415–31, doi:10.1088/0031-9155/56/14/012, 2011a.
- Albertini, F., E. B. Hug, and a. J. Lomax, Is it necessary to plan with safety margins for actively scanned proton therapy?, *Physics in medicine and biology*, 56(14), 4399–413, doi:10.1088/0031-9155/56/14/011, 2011b.
- Allen, A. M., et al., An evidence based review of proton beam therapy: The report of ASTRO’s emerging technology committee., *Radiotherapy and oncology : journal of the European Society for Therapeutic Radiology and Oncology*, 103(1), 8–11, doi:10.1016/j.radonc.2012.02.001, 2012.
- Ares, C., E. B. Hug, A. J. Lomax, A. Bolsi, B. Timmermann, H. P. Rutz, J. C. Schuller, E. Pedroni, and G. Goitein, Effectiveness and safety of spot scanning proton radiation therapy for chordomas and chondrosarcomas of the skull base: first long-term report., *International journal of radiation oncology, biology, physics*, 75(4), 1111–8, doi:10.1016/j.ijrobp.2008.12.055, 2009.
- Bangert, M., P. Hennig, and U. Oelfke, Analytical probabilistic modeling for radiation therapy treatment planning., *Physics in medicine and biology*, 58(16), 5401–19, doi:10.1088/0031-9155/58/16/5401, 2013.
- Bates, A. M., J. E. Scaife, G. S. J. Tudor, R. Jena, M. Romanchikova, J. C. Dean, A. C. F. Hoole, M. P. D. Simmons, and N. G. Burnet, Image guidance protocols: balancing imaging parameters against scan time, *The British Journal of Radiology*, 86(1032), 20130,385, doi:10.1259/bjr.20130385, PMID: 24128423, 2013.
- Bert, C., and M. Durante, Motion in radiotherapy: particle therapy., *Physics in medicine and biology*, 56(16), R113–R144, doi:10.1088/0031-9155/56/16/R01, 2011.

- Bert, C., N. Saito, A. Schmidt, N. Chaudhri, D. Schardt, and E. Rietzel, Target motion tracking with a scanned particle beam, *Medical Physics*, 34(12), 4768, doi:10.1118/1.2815934, 2007.
- Bert, C., S. O. Grözinger, and E. Rietzel, Quantification of interplay effects of scanned particle beams and moving targets., *Physics in medicine and biology*, 53(9), 2253–65, doi:10.1088/0031-9155/53/9/003, 2008.
- Besemer, A., H. Paganetti, and B. Bednarz, The clinical impact of uncertainties in the mean excitation energy of human tissues during proton therapy., *Physics in medicine and biology*, 58(4), 887–902, doi:10.1088/0031-9155/58/4/887, 2013.
- Birkner, M., D. Yan, M. Alber, J. Liang, and F. Nusslin, Adapting inverse planning to patient and organ geometrical variation: algorithm and implementation, *Medical Physics*, 30(10), 2822, doi:10.1118/1.1610751, 2003.
- Bolsi, A., A. J. Lomax, E. Pedroni, G. Goitein, and E. Hug, Experiences at the Paul Scherrer Institute with a remote patient positioning procedure for high-throughput proton radiation therapy., *International journal of radiation oncology, biology, physics*, 71(5), 1581–90, doi:10.1016/j.ijrobp.2008.02.079, 2008.
- Booth, J. T., and S. F. Zavgorodni, Set-up error & organ motion uncertainty: a review., *Australasian physical & engineering sciences in medicine / supported by the Australasian College of Physical Scientists in Medicine and the Australasian Association of Physical Sciences in Medicine*, 22(2), 29–47, 1999.
- Bortfeld, T., Optimized planning using physical objectives and constraints., *Sem Rad Oncol*, (9(1)), 20?34, 1999.
- Bortfeld, T., and W. Schlegel, An analytical approximation of depth - dose distributions for therapeutic proton beams, *Physics in Medicine and Biology*, 41(8), 1331–1339, doi:10.1088/0031-9155/41/8/006, 1996.
- Bourque, A. E., J.-F. Carrier, and H. Bouchard, A stoichiometric calibration method for dual energy computed tomography., *Physics in medicine and biology*, 59(8), 2059–88, doi:10.1088/0031-9155/59/8/2059, 2014.
- Bragg, W. H., On the Absorption of Alpha Rays and on the Classification of Alpha Rays from Radium, *Philosophical Magazine*, 8, 719–725, 1904.
- Breedveld, S., P. R. M. Storchi, M. Keijzer, A. W. Heemink, and B. J. M. Heijmen, A novel approach to multi-criteria inverse planning for IMRT., *Physics in medicine and biology*, 52(20), 6339–53, doi:10.1088/0031-9155/52/20/016, 2007.
- Burnet, N., E. Taylor, K. Kirkby, N. Thorp, R. Mackay, and M. G., Proton beam therapy for cancer: An important development for patients with an explicit agenda., *BMJ*, (344), 2488, 2012.
- Burnet, N. G., et al., Practical aspects of implementation of helical tomotherapy for intensity-modulated and image-guided radiotherapy., *Clinical oncology (Royal College of Radiologists (Great Britain))*, 22(4), 294–312, doi:10.1016/j.clon.2010.02.003, 2010.

- Cancer Research UK, CS_KF_CHILDHOOD, 2014a.
- Cancer Research UK, Cancer statistics newsletter, 2014b.
- Cancer Research UK, UK Cancer Incidence 2011 by country summary, 2014c.
- Caporaso, G. J., Y.-J. Chen, and S. E. Sampayan, The Dielectric Wall Accelerator, *Reviews of Accelerator Science and Technology*, 02(01), 253–263, doi:10.1142/S1793626809000235, 2009.
- Carabe, A., M. Moteabbed, N. Depauw, J. Schuemann, and H. Paganetti, Range uncertainty in proton therapy due to variable biological effectiveness., *Physics in medicine and biology*, 57(5), 1159–72, doi:10.1088/0031-9155/57/5/1159, 2012.
- Casiraghi, M., F. Albertini, and a. J. Lomax, Advantages and limitations of the 'worst case scenario' approach in IMPT treatment planning., *Physics in medicine and biology*, 58(5), 1323–39, doi:10.1088/0031-9155/58/5/1323, 2013.
- Chang, J. Y., X. Zhang, X. Wang, Y. Kang, B. Riley, S. Bilton, R. Mohan, R. Komaki, and J. D. Cox, Significant reduction of normal tissue dose by proton radiotherapy compared with three-dimensional conformal or intensity-modulated radiation therapy in Stage I or Stage III non-small-cell lung cancer., *International journal of radiation oncology, biology, physics*, 65(4), 1087–96, doi:10.1016/j.ijrobp.2006.01.052, 2006.
- Chen, W., J. Unkelbach, T. Alexei, T. Madden, H. Kooy, B. Thomas, and D. Craft, Including robustness in multi-criteria optimization for intensity-modulated proton therapy, *Phys Med Biol*, pp. 591–608, 2012.
- Chu, M., Robust intensity modulated radiation therapy treatment planning, Ph.D. thesis, 2006.
- Chvetsov, A. V., and S. L. Paige, The influence of CT image noise on proton range calculation in radiotherapy planning., *Physics in medicine and biology*, 55(6), N141–9, doi:10.1088/0031-9155/55/6/N01, 2010.
- Cotrutz, C., M. Lahanas, C. Kappas, and D. Baltas, A multiobjective gradient-based dose optimization algorithm for external beam conformal radiotherapy., *Physics in medicine and biology*, 46(8), 2161–75, 2001.
- Craft, D., T. Halabi, and T. Bortfeld, Exploration of tradeoffs in intensity-modulated radiotherapy., *Physics in medicine and biology*, 50(24), 5857–68, doi:10.1088/0031-9155/50/24/007, 2005.
- Crellin, A., and N. Burnet, Proton Beam Therapy: The Context, Future Direction and Challenges Become Clearer, *Clinical Oncology*, 26(12), 736–738, doi:10.1016/j.clon.2014.10.009, 2014.
- De Ruyscher, D., M. Mark Lodge, B. Jones, M. Brada, A. Munro, T. Jefferson, and M. Pijls-Johannesma, Charged particles in radiotherapy: a 5-year update of a systematic review., *Radiotherapy and oncology : journal of the European Society for Therapeutic Radiology and Oncology*, 103(1), 5–7, doi:10.1016/j.radonc.2012.01.003, 2012.

- Deasy, J. O., A proton dose calculation algorithm for conformal therapy simulations based on Molière's theory of lateral deflections., *Medical physics*, 25(4), 476–83, 1998.
- DeLaney, T. F., and H. M. Kooy, *Proton and Charged Particle Radiotherapy*, vol. 83, 87 pp., Lippincott Williams & Wilkins, 2008.
- Department of Health, National Proton Addendum, 2014.
- Dietlicher, I., M. Casiraghi, C. Ares, A. Bolsi, D. C. Weber, A. J. Lomax, and F. Albertini, The effect of surgical titanium rods on proton therapy delivered for cervical bone tumors: experimental validation using an anthropomorphic phantom., *Physics in medicine and biology*, 59(23), 7181–94, doi:10.1088/0031-9155/59/23/7181, 2014.
- Dosanjh, M., G. H. Corral, and L. M. M. Zentina, Development of Hadron Therapy for Cancer Treatment in Europe, *AIP Conference Proceedings*, pp. 12–16, doi:10.1063/1.2979248, 2008.
- Duchateau, M., et al., The effect of tomotherapy imaging beam output instabilities on dose calculation., *Physics in medicine and biology*, 55(11), N329–36, doi:10.1088/0031-9155/55/11/N03, 2010.
- Durante, M., and J. S. Loeffler, Charged particles in radiation oncology., *Nature reviews. Clinical oncology*, 7(1), 37–43, doi:10.1038/nrclinonc.2009.183, 2010.
- Engels, B., G. Soete, D. Verellen, and G. Storme, Conformal arc radiotherapy for prostate cancer: increased biochemical failure in patients with distended rectum on the planning computed tomogram despite image guidance by implanted markers., *International journal of radiation oncology, biology, physics*, 74(2), 388–91, doi:10.1016/j.ijrobp.2008.08.007, 2009.
- España, S., and H. Paganetti, The impact of uncertainties in the CT conversion algorithm when predicting proton beam ranges in patients from dose and PET-activity distributions., *Physics in medicine and biology*, 55(24), 7557–71, doi:10.1088/0031-9155/55/24/011, 2010.
- Fredriksson, A., A. Forsgren, and B. Hardemark, Minimax optimization for handling range and setup uncertainties in proton therapy, *Medical Physics*, 38(3), 1672, doi:10.1118/1.3556559, 2011.
- Furukawa, T., T. Inaniwa, S. Sato, T. Tomitani, S. Minohara, K. Noda, and T. Kanai, Design study of a raster scanning system for moving target irradiation in heavy-ion radiotherapy., *Medical physics*, 34(3), 1085–97, 2007.
- Gammex, Reference table1, 2009.
- Glimelius, B., and A. Montelius, Proton beam therapy - do we need the randomised trials and can we do them?, *Radiotherapy and oncology : journal of the European Society for Therapeutic Radiology and Oncology*, 83(2), 105–9, doi:10.1016/j.radonc.2007.04.009, 2007.

- Gordon, J. J., N. Sayah, E. Weiss, and J. V. Siebers, Coverage optimized planning: Probabilistic treatment planning based on dose coverage histogram criteria, *Medical Physics*, 37(2), 550, doi:10.1118/1.3273063, 2010.
- Grassberger, C., A. Trofimov, A. Lomax, and H. Paganetti, Variations in linear energy transfer within clinical proton therapy fields and the potential for biological treatment planning., *International journal of radiation oncology, biology, physics*, 80(5), 1559–66, doi:10.1016/j.ijrobp.2010.10.027, 2011.
- Greener, T., *Geometric Uncertainties in Radiotherapy. Appendix 2c, Practical determination of systematic and random set-up errors, Σ_{set-up} and σ_{set-up} using Portal Imaging*, 36-43 pp., BIR, 2003.
- Grözinger, S. O., E. Rietzel, Q. Li, C. Bert, T. Haberer, and G. Kraft, Simulations to design an online motion compensation system for scanned particle beams., *Physics in medicine and biology*, 51(14), 3517–31, doi:10.1088/0031-9155/51/14/016, 2006.
- Grözinger, S. O., C. Bert, T. Haberer, G. Kraft, and E. Rietzel, Motion compensation with a scanned ion beam: a technical feasibility study., *Radiation oncology (London, England)*, 3, 34, doi:10.1186/1748-717X-3-34, 2008.
- Haberer, T., W. Becher, D. Scharadt, and G. Kraft, Magnetic scanning system for heavy ion therapy, *Nuclear Instruments and Methods in Physics Research Section A: Accelerators, Spectrometers, Detectors and Associated Equipment*, 330(1-2), 296–305, doi:10.1016/0168-9002(93)91335-K, 1993.
- Harris, V., C. South, C. Cruickshank, and D. Dearnaley, 1299 poster A NATIONAL PHASE III TRIAL OF PELVIC LYMPH NODE (LN) IMRT IN PROSTATE CANCER (PIVOTAL): A COMPARISON OF LN OUTLINING METHODS, *Radiotherapy and Oncology*, 99, S486–S487, 2011.
- Hünemohr, N., B. Krauss, C. Tremmel, B. Ackermann, O. Jäkel, and S. Greilich, Experimental verification of ion stopping power prediction from dual energy CT data in tissue surrogates., *Physics in medicine and biology*, 59(1), 83–96, doi:10.1088/0031-9155/59/1/83, 2014.
- iba: proton therapy, World’s First PT Specific CBCT Goes Clinical, 2014.
- ICRP, The 2007 Recommendations of the International Commission on Radiological Protection, *Ann. ICRP 37, ICRP Publication 103*, 2–4, 2007.
- ICRU 50, International Commission on Radiation Units and Measurements: Prescribing, recording, and reporting photon beam therapy. ICRU Report no. 50, *Tech. rep.*, ICRU, 1993.
- ICRU 62, International Commission on Radiation Units and Measurements: Prescribing, recording, and reporting photon beam therapy. ICRU Report no. 62, *Tech. rep.*, ICRU, 1999.
- ICRU 78, ICRU Report 78: Prescribing, Recording, and Reporting Proton Beam Therapy , *Tech. rep.*, ICRU, 2007.

- ICRU 83, The ICRU Report 83: prescribing, recording and reporting photon-beam intensity-modulated radiation therapy (IMRT). ICRU Report no. 83, *Tech. rep.*, ICRU, 2010.
- Jette, D., and W. Chen, Creating a spread-out Bragg peak in proton beams., *Physics in medicine and biology*, 56(11), N131–8, doi:10.1088/0031-9155/56/11/N01, 2011.
- Jones, B., The potential clinical advantages of charged particle radiotherapy using protons or light ions., *Clinical oncology (Royal College of Radiologists (Great Britain))*, 20(7), 555–63, doi:10.1016/j.clon.2008.02.012, 2008.
- Khan, F. M. (Ed.), *The Physics of Radiation Therapy*, 4th ed., 74 pp., 2010.
- Kirby, D., Radiation dosimetry of conventional and laser driven particle beams., *University of Birmingham, PhD Thesis*, 2010.
- Knopf, A.-C., T. S. Hong, and A. Lomax, Scanned proton radiotherapy for mobile targets—the effectiveness of re-scanning in the context of different treatment planning approaches and for different motion characteristics., *Physics in medicine and biology*, 56(22), 7257–71, doi:10.1088/0031-9155/56/22/016, 2011.
- Lambert, J., N. Suchowerska, D. R. McKenzie, and M. Jackson, Intrafractional motion during proton beam scanning., *Physics in medicine and biology*, 50(20), 4853–62, doi:10.1088/0031-9155/50/20/008, 2005.
- Langen, K., N. Papanikolaou, and J. Balog, QA for helical TomoTherapy: Report of the AAPM Task Group 148, *Med Phys*, (37), 4817–53, 2010.
- Langen, K. M., and D. T. Jones, Organ motion and its management., *International journal of radiation oncology, biology, physics*, 50(1), 265–78, 2001.
- Langen, K. M., S. L. Meeks, D. O. Poole, T. H. Wagner, T. R. Willoughby, P. A. Kupelian, K. J. Ruchala, J. Haimerl, and G. H. Olivera, The use of megavoltage CT (MVCT) images for dose recomputations., *Physics in medicine and biology*, 50(18), 4259–76, doi:10.1088/0031-9155/50/18/002, 2005.
- Langendijk, J. A., P. Lambin, D. De Ruyscher, J. Widder, M. Bos, and M. Verheij, Selection of patients for radiotherapy with protons aiming at reduction of side effects: the model-based approach., *Radiotherapy and oncology : journal of the European Society for Therapeutic Radiology and Oncology*, 107(3), 267–73, doi:10.1016/j.radonc.2013.05.007, 2013.
- Lawrence, E. O., Method and apparatus for the acceleration of ions, 1934.
- Liu, W., X. Zhang, Y. Li, and R. Mohan, Robust optimization of intensity modulated proton therapy., *Medical physics*, 39(2), 1079–91, doi:10.1118/1.3679340, 2012.
- Lodge, M., M. Pijls-Johannesma, L. Stirk, A. J. Munro, D. De Ruyscher, and T. Jefferson, A systematic literature review of the clinical and cost-effectiveness of hadron therapy in cancer., *Radiotherapy and oncology : journal of the European Society for Therapeutic Radiology and Oncology*, 83(2), 110–22, doi:10.1016/j.radonc.2007.04.007, 2007.

- Lomax, A. J., Intensity modulation methods for proton radiotherapy, *Physics in medicine and biology*, 44, 185–205, 1999.
- Lomax, a. J., Intensity modulated proton therapy and its sensitivity to treatment uncertainties 2: the potential effects of inter-fraction and inter-field motions., *Physics in medicine and biology*, 53(4), 1043–56, doi:10.1088/0031-9155/53/4/015, 2008a.
- Lomax, a. J., Intensity modulated proton therapy and its sensitivity to treatment uncertainties 1: the potential effects of calculational uncertainties., *Physics in medicine and biology*, 53(4), 1027–42, doi:10.1088/0031-9155/53/4/014, 2008b.
- Lomax, A. J., et al., Treatment planning and verification of proton therapy using spot scanning: Initial experiences, *Medical Physics*, 31(11), 3150, doi:10.1118/1.1779371, 2004.
- Matlab UK, The Language of Technical Computing, 2011.
- Matsuura, T., et al., Apparent absence of a proton beam dose rate effect and possible differences in RBE between Bragg peak and plateau, *Medical Physics*, 37(10), 5376, doi: 10.1118/1.3490086, 2010.
- McGowan, S. E., C. D. Greaves, and S. Evans, An investigation into truncation artefacts experienced in cardiac imaging using a dedicated cardiac SPECT gamma camera with transmission attenuation correction., *Nuclear medicine communications*, 33(12), 1287–91, doi:10.1097/MNM.0b013e328359db76, 2012.
- McGowan, S. E., N. G. Burnet, and a. J. Lomax, Treatment planning optimisation in proton therapy., *The British journal of radiology*, 86(1021), 20120,288, doi:10.1259.bjr.20120288, 2013.
- McLean, D., Artefact reduction on CT images of fossils to allow 3D visualisation, 2000.
- Meiers, G., A. Nanz, R. Besson, S. Safai, and A. Lomax, Logfile based dose calculations as a quality assurance tool in scanned beam proton radiotherapy , *ICTR, Geneva*, 2014.
- Merchant, T. E., C.-H. Hua, H. Shukla, X. Ying, S. Nill, and U. Oelfke, Proton versus photon radiotherapy for common pediatric brain tumors: comparison of models of dose characteristics and their relationship to cognitive function., *Pediatric blood & cancer*, 51(1), 110–7, doi:10.1002/psc.21530, 2008.
- Moyers, M. F., M. Sardesai, S. Sun, and D. W. Miller, Ion stopping powers and CT numbers., *Medical dosimetry : official journal of the American Association of Medical Dosimetrists*, 35(3), 179–94, doi:10.1016/j.meddos.2009.05.004, 2010.
- Murray, J., D. McQuaid, A. Dunlop, F. Buettner, S. Nill, E. Hall, D. Dearnaley, and S. Guliford, SU-E-J-14: A Novel Approach to Evaluate the Dosimetric Effect of Rectal Variation During Image Guided Prostate Radiotherapy, *Medical Physics*, 41(6), 157–157, doi:10.1118/1.4888065, 2014.
- Newhauser, W. D., A. Giebeler, K. M. Langen, D. Mirkovic, and R. Mohan, Can megavoltage computed tomography reduce proton range uncertainties in treatment plans for patients with large metal implants?, *Physics in medicine and biology*, 53(9), 2327–44, doi:10.1088/0031-9155/53/9/009, 2008.

- Nguyen, T., A. Hoole, N. Burnet, and S. Thomas, The optimization of intensity modulated radiotherapy in cases where the planning target volume extends into the build-up region, *Phys. Med. Biol.*, (54), 2511–2525, 2009.
- NHS Specialised Services, NHS Specialised Services, 2011.
- Nil, S., T. Bortfeld, and U. Oelfke, Inverse planning of intensity modulated proton therapy., *Zeitschrift für medizinische Physik*, 14(1), 35–40, 2004.
- NRIG, International Commission on Radiation Units and Measurements: Prescribing, recording, and reporting photon beam therapy. ICRU Report no. 50, *Tech. rep.*, The National Cancer Action Team, 2012.
- Oelfke, U., and T. Bortfeld, Intensity modulated radiotherapy with charged particle beams: Studies of inverse treatment planning for rotation therapy, *Medical Physics*, 27(6), 1246, doi:10.1118/1.599002, 2000.
- Onozato, Y., et al., Evaluation of on-board kV cone beam computed tomography-based dose calculation with deformable image registration using Hounsfield unit modifications., *International journal of radiation oncology, biology, physics*, 89(2), 416–23, doi:10.1016/j.ijrobp.2014.02.007, 2014.
- Park, P. C., X. R. Zhu, A. K. Lee, N. Sahoo, A. D. Melancon, L. Zhang, and L. Dong, A Beam-Specific Planning Target Volume (PTV) Design for Proton Therapy to Account for Setup and Range Uncertainties, 2012.
- Peach, K. J., et al., PAMELA Overview : design goals and principles, 2009.
- Pedroni, E., S. Scheib, T. Böhringer, a. Coray, M. Grossmann, S. Lin, and a. Lomax, Experimental characterization and physical modelling of the dose distribution of scanned proton pencil beams, *Physics in Medicine and Biology*, 50(3), 541–561, doi:10.1088/0031-9155/50/3/011, 2005.
- Pedroni, E., et al., The 200-MeV proton therapy project at the Paul Scherrer Institute: conceptual design and practical realization., *Medical physics*, 22(1), 37–53, 1995.
- Pflugfelder, D., Worst case optimization : a method to account for uncertainties in the optimization of intensity, *Cancer Research*, 1689, doi:10.1088/0031-9155/53/6/013, 2008.
- Phillips, C., What is a QALY?, 2009.
- Phillips, M. H., E. Pedroni, H. Blattmann, T. Boehringer, A. Coray, and S. Scheib, Effects of respiratory motion on dose uniformity with a charged particle scanning method., *Physics in medicine and biology*, 37(1), 223–34, 1992.
- Proton Therapy Today - The online magazine for proton therapy, Where to get pt?, 2014.
- Ramaekers, B. L. T., M. Pijls-Johannesma, M. a. Joore, P. van den Ende, J. a. Langendijk, P. Lambin, A. G. H. Kessels, and J. P. C. Grutters, Systematic review and meta-analysis of radiotherapy in various head and neck cancers: comparing photons, carbon-ions and protons., *Cancer treatment reviews*, 37(3), 185–201, doi:10.1016/j.ctrv.2010.08.004, 2011.

- Raysearch Laboratory, RayStation 4.5 news, 2014.
- Rietzel, E., and C. Bert, Respiratory motion management in particle therapy, *Medical Physics*, 37(2), 449, doi:10.1118/1.3250856, 2010.
- Rimmer, Y. L., et al., Practical issues in the implementation of image-guided radiotherapy for the treatment of prostate cancer within a UK department., *Clinical oncology (Royal College of Radiologists (Great Britain))*, 20(1), 22–30, doi:10.1016/j.clon.2007.10.001, 2008.
- Robertson, J. B., J. R. Williams, R. A. Schmidt, J. B. Little, D. F. Flynn, and H. D. Suit, Radiobiological studies of a high-energy modulated proton beam utilizing cultured mammalian cells., *Cancer*, 35(6), 1664–77, 1975.
- Rutz, H. P., et al., Extracranial chordoma: Outcome in patients treated with function-preserving surgery followed by spot-scanning proton beam irradiation., *International journal of radiation oncology, biology, physics*, 67(2), 512–20, doi:10.1016/j.ijrobp.2006.08.052, 2007.
- Sadrozinski, H.-W., et al., Toward Proton Computed Tomography, *IEEE Transactions on Nuclear Science*, 51(1), 3–9, doi:10.1109/TNS.2003.823044, 2004.
- Safai, S., S. Lin, and E. Pedroni, Development of an inorganic scintillating mixture for proton beam verification dosimetry, *Physics in Medicine and Biology*, 49(19), 4637–4655, doi:10.1088/0031-9155/49/19/013, 2004.
- Saito, N., C. Bert, N. Chaudhri, A. Gemmel, D. Schardt, M. Durante, and E. Rietzel, Speed and accuracy of a beam tracking system for treatment of moving targets with scanned ion beams., *Physics in medicine and biology*, 54(16), 4849–62, doi:10.1088/0031-9155/54/16/001, 2009.
- Schaffner, B., and E. Pedroni, The precision of proton range calculations in proton radiotherapy treatment planning: experimental verification of the relation between CT-HU and proton stopping power., *Physics in medicine and biology*, 43(6), 1579–92, 1998.
- Schaffner, B., E. Pedroni, and A. Lomax, Dose calculation models for proton treatment planning using a dynamic beam delivery system: an attempt to include density heterogeneity effects in the analytical dose calculation, *Physics in Medicine and Biology*, 44(1), 27–41, doi:10.1088/0031-9155/44/1/004, 1999.
- Schätti, A., M. Zakova, D. Meer, and A. J. Lomax, Experimental verification of motion mitigation of discrete proton spot scanning by re-scanning., *Physics in medicine and biology*, 58(23), 8555–72, doi:10.1088/0031-9155/58/23/8555, 2013.
- Schätti, A., D. Meer, and A. J. Lomax, First experimental results of motion mitigation by continuous line scanning of protons., *Physics in medicine and biology*, 59(19), 5707–23, doi:10.1088/0031-9155/59/19/5707, 2014.
- Scheib, S., and E. Pedroni, Dose calculation and optimization for 3D conformal voxel scanning, *Radiation and Environmental Biophysics*, 31(3), 251–256, doi:10.1007/BF01214833, 1992.

- Schneider, U., E. Pedroni, and A. Lomax, The calibration of CT Hounsfield units for radiotherapy treatment planning, *Physics in Medicine and Biology*, 41(1), 111–124, doi:10.1088/0031-9155/41/1/009, 1996.
- Schulte, R., et al., Conceptual design of a proton computed tomography system for applications in proton radiation therapy, *IEEE Transactions on Nuclear Science*, 51(3), 866–872, doi:10.1109/TNS.2004.829392, 2004.
- Seco, J., D. Robertson, A. Trofimov, and H. Paganetti, Breathing interplay effects during proton beam scanning: simulation and statistical analysis., *Physics in medicine and biology*, 54(14), N283–94, doi:10.1088/0031-9155/54/14/N01, 2009.
- Sheehan, M., et al., Position statement on ethics, equipoise and research on charged particle radiation therapy., *Journal of medical ethics*, 40(8), 572–5, doi:10.1136/medethics-2012-101290, 2014.
- Slater, J. D., C. J. Rossi, L. T. Yonemoto, D. A. Bush, B. R. Jabola, R. P. Levy, R. I. Grove, W. Preston, and J. M. Slater, Proton therapy for prostate cancer: the initial Loma Linda University experience., *International journal of radiation oncology, biology, physics*, 59(2), 348–52, doi:10.1016/j.ijrobp.2003.10.011, 2004.
- Staab, A., et al., Spot-scanning-based proton therapy for extracranial chordoma., *International journal of radiation oncology, biology, physics*, 81(4), e489–96, doi:10.1016/j.ijrobp.2011.02.018, 2011.
- Stroom, J. C., H. C. de Boer, H. Huizenga, and A. G. Visser, Inclusion of geometrical uncertainties in radiotherapy treatment planning by means of coverage probability, *International Journal of Radiation Oncology*Biophysics*, 43(4), 905–919, doi:10.1016/S0360-3016(98)00468-4, 1999.
- Thieke, C., K.-H. Küfer, M. Monz, A. Scherrer, F. Alonso, U. Oelfke, P. E. Huber, J. Debus, and T. Bortfeld, A new concept for interactive radiotherapy planning with multi-criteria optimization: first clinical evaluation., *Radiotherapy and oncology : journal of the European Society for Therapeutic Radiology and Oncology*, 85(2), 292–8, doi:10.1016/j.radonc.2007.06.020, 2007.
- Thomas, S. J., Margins for treatment planning of proton therapy., *Physics in medicine and biology*, 51(6), 1491–501, doi:10.1088/0031-9155/51/6/009, 2006.
- Thomas, S. J., M. Ashburner, G. S. J. Tudor, J. Treeby, J. Dean, D. Routsis, Y. L. Rimmer, S. G. Russell, and N. G. Burnet, Intra-fraction motion of the prostate during treatment with helical tomotherapy., *Radiotherapy and oncology : journal of the European Society for Therapeutic Radiology and Oncology*, 109(3), 482–6, doi:10.1016/j.radonc.2013.09.011, 2013.
- Towse, A., *Cost effectiveness thresholds: economic and ethical issues*, King's Fund/Office for Health Economics., London, 2002.
- University of Oxford, £110m research centre in cancer medicine to be established at Oxford University, 2014.

- Unkelbach, J., and U. Oelfke, Incorporating organ movements in IMRT treatment planning for prostate cancer: minimizing uncertainties in the inverse planning process., *Medical physics*, 32(8), 2471–83, 2005.
- Unkelbach, J., T. C. Y. Chan, and T. Bortfeld, Accounting for range uncertainties in the optimization of intensity modulated proton therapy., *Physics in medicine and biology*, 52(10), 2755–73, doi:10.1088/0031-9155/52/10/009, 2007.
- van de Water, T. a., H. P. Bijl, C. Schilstra, M. Pijls-Johannesma, and J. a. Langendijk, The potential benefit of radiotherapy with protons in head and neck cancer with respect to normal tissue sparing: a systematic review of literature., *The oncologist*, 16(3), 366–77, doi:10.1634/theoncologist.2010-0171, 2011.
- van Herk, M., Errors and margins in radiotherapy., *Seminars in radiation oncology*, 14(1), 52–64, doi:10.1053/j.semradonc.2003.10.003, 2004.
- van Herk, M., P. Remeijer, C. Rasch, and J. V. Lebesque, The probability of correct target dosage: dose-population histograms for deriving treatment margins in radiotherapy, *International Journal of Radiation Oncology*Biology*Physics*, 47(4), 1121–1135, doi:10.1016/S0360-3016(00)00518-6, 2000.
- Vees, H., G. Dipasquale, P. Nouet, T. Zilli, L. Cozzi, and R. Miralbell, Pelvic Lymph Node Irradiation Including Pararectal Sentinel Nodes for Prostate Cancer Patients: Treatment Optimization Comparing Intensity Modulated X-rays, Volumetric Modulated Arc Therapy, and Intensity Modulated Proton Therapy., *Technology in cancer research & treatment*, doi:10.7785/tcrt.2012.500405, 2014.
- voxtox, The voxtox research programme - linking radiation dose at the voxel level with toxicity, 2014.
- Webb, S., The physical basis of IMRT and inverse planning, *British Journal of Radiology*, 76(910), 678–689, doi:10.1259/bjr/65676879, 2003.
- www.dh.gov.uk, London, uk: Department of health; 2012, 2012.
- Yadav, P., R. Tolakanahalli, Y. Rong, and B. R. Paliwal, The effect and stability of MVCT images on adaptive TomoTherapy, *Journal of Applied Clinical Medical Physics*, 11(4), 2010.
- Yang, M., G. Virshup, J. Clayton, X. R. Zhu, R. Mohan, and L. Dong, Does kV-MV dual-energy computed tomography have an advantage in determining proton stopping power ratios in patients?, *Physics in medicine and biology*, 56(14), 4499–515, doi:10.1088/0031-9155/56/14/017, 2011.
- Yang, M., X. R. Zhu, P. C. Park, U. Titt, R. Mohan, G. Virshup, J. E. Clayton, and L. Dong, Comprehensive analysis of proton range uncertainties related to patient stopping-power-ratio estimation using the stoichiometric calibration., *Physics in medicine and biology*, 57(13), 4095–115, doi:10.1088/0031-9155/57/13/4095, 2012.

- Yazdi, M., M. Yazdia, L. Gingras, and L. Beaulieu, An adaptive approach to metal artifact reduction in helical computed tomography for radiation therapy treatment planning: experimental and clinical studies., *International journal of radiation oncology, biology, physics*, 62(4), 1224–31, doi:10.1016/j.ijrobp.2005.02.052, 2005.
- Zenklusen, S. M., E. Pedroni, and D. Meer, A study on repainting strategies for treating moderately moving targets with proton pencil beam scanning at the new Gantry 2 at PSI., *Physics in medicine and biology*, 55(17), 5103–21, doi:10.1088/0031-9155/55/17/014, 2010.
- Zietman, A. L., et al., Randomized trial comparing conventional-dose with high-dose conformal radiation therapy in early-stage adenocarcinoma of the prostate: long-term results from proton radiation oncology group/american college of radiology 95-09., *Journal of clinical oncology : official journal of the American Society of Clinical Oncology*, 28(7), 1106–11, doi:10.1200/JCO.2009.25.8475, 2010.

Appendix A

Published Work and Presentations

Presented here is published work written during the course of this thesis.

Published review article in the British Journal of Radiology. McGowan SE, Burnet NG, Lomax AJ. (2013) *Treatment planning optimisation in proton therapy* The British journal of radiology, 86(1021), 20120,288.

Oral presentation at the 20th International Conference on Medical Physics. McGowan SE, Albertini F, Thomas SJ, Burnet NG & Lomax AJ. A retrospective study of proton treatment plan robustness in the skull base. The 20th International Conference on Medical Physics (ICMP2013) at the Brighton Centre, Brighton, UK from 1-4th September 2013

ePoster presentation at 2014 ESTRO Annual Meeting. McGowan SE, Albertini F, Thomas SJ, & Burnet NG. (2014) *Defining Robustness protocols: a method to include and evaluate robustness in clinical plans.*

Accepted scientific paper in Physics in Medicine and Biology Journal McGowan SE, Albertini F, Thomas SJ, Lomax AJ. PMB (Accepted 2014) *Defining robustness protocols: a method to include and evaluate robustness in clinical plans*

Cite this article as: McGowan SE, Burnet NG, Lomax AJ. Treatment planning optimisation in proton therapy. *Br J Radiol* 2013;86:20120288.

REVIEW ARTICLE

Treatment planning optimisation in proton therapy

^{1,2}S E MCGOWAN, MSc, ^{1,2}N G BURNET, FRCR, MD and ³A J LOMAX, PhD

¹Department of Oncology, University of Cambridge, Cambridge, UK, ²Oncology Centre, Addenbrooke's Hospital, Cambridge, UK, and ³Centre for Proton Radiotherapy, Paul Scherrer Institute, Villigen PSI, Switzerland

ABSTRACT. The goal of radiotherapy is to achieve uniform target coverage while sparing normal tissue. In proton therapy, the same sources of geometric uncertainty are present as in conventional radiotherapy. However, an important and fundamental difference in proton therapy is that protons have a finite range, highly dependent on the electron density of the material they are traversing, resulting in a steep dose gradient at the distal edge of the Bragg peak. Therefore, an accurate knowledge of the sources and magnitudes of the uncertainties affecting the proton range is essential for producing plans which are robust to these uncertainties. This review describes the current knowledge of the geometric uncertainties and discusses their impact on proton dose plans. The need for patient-specific validation is essential and in cases of complex intensity-modulated proton therapy plans the use of a planning target volume (PTV) may fail to ensure coverage of the target. In cases where a PTV cannot be used, other methods of quantifying plan quality have been investigated. A promising option is to incorporate uncertainties directly into the optimisation algorithm. A further development is the inclusion of robustness into a multicriteria optimisation framework, allowing a multi-objective Pareto optimisation function to balance robustness and conformity. The question remains as to whether adaptive therapy can become an integral part of a proton therapy, to allow re-optimisation during the course of a patient's treatment. The challenge of ensuring that plans are robust to range uncertainties in proton therapy remains, although these methods can provide practical solutions.

Received 29 May 2012
Revised 6 September 2012
Accepted 1 October 2012

DOI: 10.1259/bjr.20120288

© 2013 The British Institute of
Radiology

The ability to create and deliver the ideal treatment plan, where the target volume receives 100% of the prescribed dose and normal tissue receives 0%, is the holy grail of radiation therapy [1]. It is, however, impossible to achieve this perfect balance. Instead, multiple trade-offs are required to achieve a clinically acceptable plan, so the problem becomes one of optimisation. There are many factors that can affect how "optimised" a patient's treatment can be. This review focuses on the challenges of proton therapy plan optimisation, particularly in regard to range uncertainties, and how to incorporate them into the plan evaluation and verification process.

The nature of proton therapy makes the aim of cure without complications potentially more achievable, owing to the highly localised deposition of dose in the characteristic Bragg peak [2]. This relates predominantly to the ability to deliver high doses of radiation close to normal tissue structures, which would be dose limiting in conventional X-ray treatments, and to the finite range

of protons, which results in a reduced integral dose to surrounding normal tissues.

From a clinical perspective, the exact role of proton therapy has yet to be defined. However, for childhood cancers, proton therapy delivers a lower dose to tissues around the tumour than X-rays, resulting in less growth disturbance and lower risk of secondary malignancies. There is also the suggestion that the use of proton therapy can reduce impairment of neuropsychological and intelligence quotient development [3]. In adults, proton therapy seems particularly effective in the treatment of radio-resistant tumours close to critical structures such as the brain stem and spinal cord. For example, outstanding results have been published for the use of proton therapy in the treatment of chordoma and chondrosarcoma [4]. The current evidence for the use of proton therapy at different sites has been extensively reviewed [5–8]. However, it will also be important to consider expanding potential indications where logic and dosimetry indicate that proton therapy can confer an advantage [7]. Although clinical results comparing proton therapy with the most modern X-ray therapy are currently lacking, overall clinical outcomes are promising for both delivery options and support the rationale for proton therapy [8]. The reader is referred to the literature [9–11] for more clinical data. Nevertheless, substantial opportunity for further clinical research development and evaluation remains.

Address correspondence to: Miss Stacey E. McGowan, Selwyn College, University of Cambridge, Grange Road, Cambridge CB3 9DQ, UK. E-mail: sem89@cam.ac.uk
SEM's PhD is funded by the Medical Research Council. NGB is supported by the National Institute for Health Research (NIHR), Cambridge Biomedical Research Centre.

Defining robustness protocols: a method to include and evaluate robustness in clinical plans

Stacey McGowan^a, Francesca Albertini^b, Simon Thomas^c, Neil Burnet^c, Tony Lomax^b

University of Cambridge^a, Paul Scherrer Institute^b, Cambridge University Hospitals^c.

Email: sem89@cam.ac.uk

Conclusions

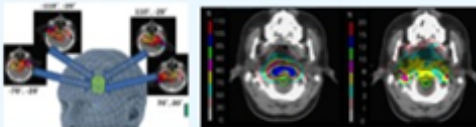
3D IMPT offers the ability to deliver highly conformal radiotherapy to the patient, reducing integral normal tissue dose¹ and providing greater OAR sparing through the use of multiple inhomogeneous fields. However, without certainty in our ability to deliver these highly complex and conformal plans at each fraction caution must be heeded when choosing beam arrangements and positioning steep dose gradients near OARs²⁻⁴ as any uncertainty might lead to severe target undershoot or OAR overshoot. Several authors are proposing to include the plan robustness as an extra parameter directly during the optimization process⁵⁻⁹. Unfortunately when introducing the robustness parameter into the optimisation algorithm,

the nominal plan quality is often compromised^{5,7}. Although we believe that the use of a robust plan is probably the correct way to deal with uncertainties in IMPT planning, we think also that it is extremely important to define a threshold between robustness and plan quality. In particular it is important to establish the adequate level of robustness for each volume. This can be used on one side as an input parameter during the robust optimization process and on the other side as control parameter during the plan evaluation phase.

The concept of a site specific robustness **DATABASE**, hereby introduced can indeed be used for both purposes.

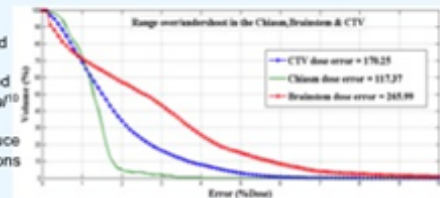
Methods

16 clinical skull base 3D IMPT plans were retrospectively analysed in terms of robustness to systematic range and random set-up uncertainties in the brainstem, chiasm and the CTV.



4-field IMPT arrangement for skull base plans at PSI, Switzerland. Left: Nominal dose. Right: error in dose from range uncertainty

To determine plan robustness the set-up and range uncertainties were modelled as in the method proposed by Albertini *et al*¹⁰ and later validated by Casiraghi *et al*¹¹ to produce 'error-bar' dose distributions (ebDD).



The robustness of each volume has been analysed by extracting the error-bar volume histogram (ebVH). Metrics can be defined and analysed as for example the maximum error, the mean error and the volume receiving an error of 3%, 5% and 10% (V3%, V5%, V10%).

Site Specific Robustness **DATABASE** defined for IMPT plans for skull-base cases at PSI

| VOI | Mean range | Mean set-up | Max range | Max set-up |
|-----------|-------------|-------------|-------------|---------------|
| Brainstem | 1.75 - 2.2% | 4.8 - 7.8% | 8.1 - 11.6% | 15 - 22% |
| Chiasm | 1 - 2% | 6 - 9% | 7 - 12.7% | 17 - 25% |
| CTV | 1 - 1.2% | 8.2 - 15% | 2 - 4.5% | 13.65 - 18.5% |

The **DATABASE** can be used to aid planners in visualising the magnitude of effect that range and set-up errors can have on patient treatment. The ranges represent the deviation from the nominal dose in that volume caused by the error for this patient sample. The values have outliers removed for an over-dosage scenario to OAR and under-dosage scenario to the CTV. The lower limits are included to allow the planner to see where a compromise between conformality and robustness can be made.

Results

It was seen that the impact of the random set-up error was greater than that resulting from the range error in all three volumes of interest (VOIs) for each parameter measured. Also that the mean and standard deviation in the range error was lower for the OARs than for the CTV; the opposite was true for the set-up error. Of the plans retrospectively analysed, one plan showed to have a worse robustness in the brainstem compared to the sample. In particular, this plan resulted to have a potential maximum range error in the brainstem of 12.7% (Vs 8.1-11.6% in the **DATABASE**). To investigate the possibility of improving the plan robustness while keeping the same target coverage and satisfying the dose limits assigned to the organs-at-risk, several plans with different beam arrangements were calculated to obtain a more optimal plan.

Summary

Through retrospectively analysing the robustness of each VOI a site specific Robustness **DATABASE** was established. It has been here discussed how the database can be used to identify patients that require a more individualized plan to improve the robustness to uncertainties. Although the defined **DATABASE** is specific to PSI, the idea can be used as an example for other centres to define, for the moment, their own robustness parameters. Hopefully, with more people starting to introduce the robustness evaluation in the clinical process, we will be able in the future to define an adequate level of robustness for each volume that is accepted worldwide, in the same way as dose-volume-constraints to organs-at-risk and prescribed dose to target volumes are generally widely accepted and applied in the different protocols.



1. Chang J. *et al* *biology physics* (2006) vol 65, 4 p. 1087-1096.
2. Lomax 2008, *Physics in medicine and biology*, 53(4): 1043-56.
3. Albertini *et al* 2010 *Physics in medicine and biology*, 55(10): 2863-70.
4. McGowan, S. *et al* 2013, *The British journal of radiology*, 86(1021): 5.
5. Ueklebar *et al* 2007, *Physics in medicine and biology*, 52(10): 2755-71.
6. Pfugfelder 2008, *Cancer Research*, 68: 7.
7. Emdiksson *et al* 2011, *Med. Phys.* (2011): 38, 1672-8.
8. Liu *et al* 2012 *Med Phys.* 2012: 39(2): 1079-1091.
9. Chen *et al* 2012 *PMB*, 10.
10. Albertini *et al* 2011 *Physics in medicine and biology*, 56(14): 4399-413.
11. Casiraghi *et al* 2013 *Physics in medicine and biology*, 58(5): 1323-39.

Defining robustness protocols: a method to include and evaluate robustness in clinical plans

ABSTRACT Aim: To define a site-specific robustness protocol to be used during the clinical plan evaluation process.

Method: Plan robustness of 16 skull base IMPT plans to systematic range and random set-up errors has been retrospectively and systematically analyzed. This was determined by calculating the error-bar dose distribution (ebDD) for all the plans and by defining some metrics used to define protocols aiding the plan assessment. Additionally, an example of how to clinically use the defined robustness database is given whereby a plan with sub-optimal brainstem robustness was identified. The advantage of using different beam arrangements to improve the plan robustness was analysed.

Results: Using the ebDD it was found range errors had a smaller effect on dose distribution than the corresponding set-up error, and that organs at risk were most robust to the range errors, whereas the target was more robust to set-up errors. A database was created to aid planners in terms of plan robustness aims in these volumes. This resulted in the definition of site specific robustness protocols. The use of robustness constraints allowed for the identification of a specific patient that may have benefited from a treatment of greater individuality. A new beam arrangement showed to be preferential when balancing conformality and robustness for this case.

Conclusions: The ebDD and error volume histogram proved effective in analysing plan robustness. The process of retrospective analysis could be used to establish site specific robustness planning protocols in proton planning. These protocols allow the planner to determine plans that, although delivering a dosimetrically adequate dose distribution, have resulted in sub-optimal robustness to these uncertainties. For these cases the use of different beam start conditions may improve the plan robustness to set-up and range uncertainties.

A.0.1 Other Presentations

Poster presentation at Cambridge Science Festival. McGowan SE, *Proton Therapy* 2011

Poster presentation at the School of Clinical Medicine Research day. McGowan SE, *Planning for Proton Therapy*. 2012

Oral presentation at the 2014 PPRIG, NPL. McGowan SE, Albertini F, Thomas SJ, Burnet NG & Lomax AJ. The importance of plan robustness in proton beam therapy. Proton Therapy Physics Workshop (NPL PPRIG) at the National Physical Laboratory, 12th – 13th March 2014.

Invited speaker at the Christie Hospital in Manchester McGowan SE, *Treatment Planning Uncertainties in Proton Therapy* 2014



Planning for Proton Beam Therapy

Incorporating range uncertainty into the patient's treatment plan

Stacey McGowan, University of Cambridge

Cure without Complication

Ideal

Optimal

Dose (%)

The ideal dose would deliver 100% of the prescribed radiation dose to the tumour and zero dose to healthy tissue. As this is impossible the problem becomes one of optimization.

The optimal dose means plan not only looks to achieve adequate dose coverage whilst sparing healthy tissue (conformality), but also delivers treatment which matches the planned treatment objectives.

X-ray Radiotherapy Vs Proton Beam Therapy

Conventional radiotherapy uses high energy X-rays.

Unlike X-rays, protons have a finite range (we can choose where they stop) allowing greater conformity and reducing radiation exposure to the patient.

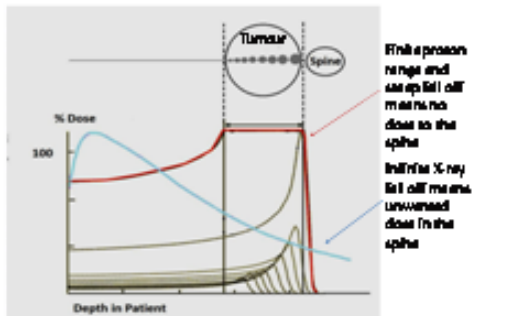
X-ray plan Proton plan

Proton therapy is beneficial for a variety of cancers, especially childhood cancers by reducing...

- The likelihood of growth related complications.
- And, the chance of developing cancer again in the future.

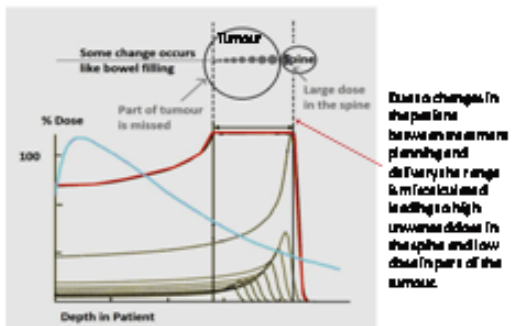
Range Uncertainties in Proton Beam Therapy

Compared to X-rays, protons have a given range highly dependent on the material they are travelling through, resulting in a sharp dose fall at the end of the treatment field.



X-ray and proton dose with depth in patient illustrating tumour coverage and organ sparing.

However, if a mass proton therapy is less robust to a normal change than when using X-rays, emphasizing the need to be careful for the ability to assess and manage uncertainties in proton therapy.



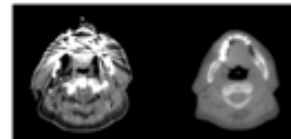
Small changes between planning and delivery can lead to large range uncertainties in the patient.

The need to assess the robustness of a plan to the effects of uncertainty is of major importance in proton therapy. The problem is also that it's not only assessing and managing uncertainties, but in establishing tumour site-specific robustness constraints in proton beam planning.



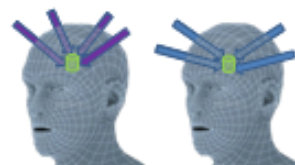
Uncertainties and my PhD research

Several factors will influence a plan's robustness including patient immobilisation, beam orientation and the individual patient anatomy. Specifically from the viewpoint of the clinician, daily patient motion and planning uncertainties conditions, such as the number of beams used and the beam orientation.



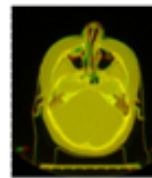
Two X-ray CT images compared by mass localisation. The X-ray CT image is affected by mass, but suffers fewer variations.

Image quality - Mass localisation can corrupt the image. The use of different imaging modalities means we can correct for these artefacts. Ensuring accurate range calculation in patients with metal is a core aim of my PhD.



Schematic of two clinical proton beam arrangements used to treat skull base tumours.

Start Conditions - Two different beam arrangements, like the two shown, can be used to plan near identical treatment. The terms of conformity. However, they will differ in the dose distribution due to the different beam arrangements. The use of density which beam arrangement conditions are most robust for will be a summary.



Quantifying changes in proton range from cone-beam CT scans. Yellow areas are where the images match.

Daily Changes - As anatomy changes daily due to things like weight gain and fluid filling. Using daily acquisition of imaging data from patient allows the change in range can be measured and planned by proton. This data can be used to alter the treatment plan and a dose accumulation model of range uncertainty can be used to assess the daily beam.

Understanding uncertainties and range uncertainty will enable us to use the proton beam treatment to model the effects of range uncertainties to determine how best to proceed in the future and provide the best care possible for the patient.

The Future of Protons in the NHS

In the UK, since 2006 patients have been able to access proton therapy abroad under the auspices of the NHS Proton Charities Programme (PCP). The Government have announced that two proton centres will be established in England. It is hoped that the NHS will be able to treat patients in the next 4-5 years.

Fig. A.3 Winning popular press poster describing my research to the general public at the School of Clinical Medicine Research day 2012



UNIVERSITY OF
CAMBRIDGE

*School of Clinical Medicine
Research Day 2013*

Popular Press Poster Presentation

First Prize awarded to

Stacey McGowan

Course Organiser

*Dr Geraint Wyn Story
Researcher Development Consultant
Graduate School of Life Sciences*

Fig. A.4 Copy of my certificate for presenting a popular press poster at the clinical school Research day

Appendix B

Code

This appendix includes the main functions used to create the results in Chapter 4. In order as presented here these include,

- Startcons
- First Fraction
- Next Fraction
- Read MVCT DICOM
- Apply CT shifts
- Read in structure DICOM set
- Water equivalent path-length code
- Results Script

A more indepth description of how principle functions work is provided below followed by the codes. Some of these functions were created specific to either prostate or head and neck patients. I have only included one of the versions, rather than both, as mostly the code is identical except for directories.

Startcons

This function sets the starting conditions and is where the user can edit the parameters to be used in the rest of the code. These parameters are split into families for programming

ease; each family was constructed as a structure set. The four main families included Beam Data, (*Beam*), Structure data, (*Struct*), DICOM data (*Dicomstruct*) and patient data, (*Pat*). Through the coding process data is added and stored to these families to be called and used later and in other functions. This way only the family structures need to be passed between functions and not an entire lists of variables.

Beam variables include the beam angle, imaging modality and source to isocentre distance (SID)*.

Struct variables include the number of structures to be analysed, their names as a string, and the number of letters in the string.

Dicomstruct variables include the pixel dimensions, number of slices in the data set and the coordinate system.

Pat variables include the patient token, the directory names for retrieving and saving patient data, the treatment site (i.e. prostate) and current fraction being investigated.

**The SID has been set to seven metres in this study, this is the distance used in the proton at CNAO, Pavia and is used simply as an example. At PSI at dose calculation the SID is assumed infinite.*

First fraction Next fraction

These are the two main scripts used to run functions. The first reads in the data required for comparison, this is any fraction of the patient treatment that will be used to compare the consecutive fractions to, or respective fractions depending on the investigation. This script will first call the function to establish the start conditions. It then loops through the folders in that patient directory to find the relevant DICOM information and Structure sets. The next script loops through the remaining fractions and carries out all the same functions, except the one to read in the structure set coordinates as these have already been saved in the directory so they can just be loaded into Matlab to determine which slices on the shifted MVCT are required for calculating the WEPL.

Read MVCT DICOM

This function goes to the pre-specified directory as determined in either `firstfraction.m` or `nextfraction.m` to access the MVCT data. For some patients there may exist two sets of MVCT with the same date label so time labels are also used when organising all the image data. For these fractions, where two MVCT images exist, the patient was imaged prior to and post treatment as part of a previous research study. The code allows for this and will carry out full calculations for both imaging data sets while remaining within the same fraction. This data will be used for investigating intra- fraction range errors by making comparison between the prior and post treatment images.

As well reading the DICOM data and storing it as a 3D matrix, the code will also take and store information from the DICOM header to store in *Dicomstruct*. This structure will hold all the information relevant to that DICOM data needed for calculation. This information includes, pixel size, slice thickness, number of pixels in each dimension, the coordinate system, HU offset and the shifts that were applied to the couch in that instance. In the case where shift data is missing, no shift will be applied.

It must be noted that DICOM data does not usually come with the shift information, this has been retrieved directly from the TomoTherapy system to remove human error and added to the header as part of the VoxTox study.

Apply CT shifts

For each treatment fraction on TomoTherapy the radiographer will set the patient up for treatment and perform an MVCT scan. The radiographer will perform image registration of the MVCT image to the planning kVCT making any of their own adjustments online and determine the final shift required in each axis (x, yz*, zy*) and for the roll. These shifts are translated to changes in the couch position and are applied. The patient will then be treated in this position. By applying these shifts to the MVCT image we can simulate the patient position at the time of treatment. In this study we have not included the roll shifts in our calculation. It is also at this point that truncation is compensated for by reading in and applying shifts to the kVCT data for prostate patients.

* *Normal 'non-TomoTherapy' axis – These are the axis used in script*

The role of this function is to take all the information in the *Dicomstruct* family and use it to apply a shift to the 3D matrix that is our patient's image from that fraction. The shift is

achieved by creating two coordinate systems of the same size of the matrix. The first is the coordinate system retrieved from the DICOM header; the second is this coordinate system with the shifts added to it in each direction. For example if say pixel (1,1,1) existed at the coordinates (0,0,-12) and rigid couch shifts (0.5,1.5,-1) were applied, the new coordinate system for pixel (1,1,1) would be (0.5,1.5,-13). This is done to all pixels, in pixel dimension rather than in *mm*, and a 3D cubic interpolation is carried out to determine the new values of pixel data. Instead of extrapolating the data in the z direction where it is missing, the previous interpolated slices are repeated. In the x and y directions zeros are used to pad the matrix out as only air existed there. These zeros are then dealt with later when all air is assigned to the same value.

Read in structure DICOM set

A function will then read in the correct structure coordinates and store them. This function loops through the relevant part of the structure set DICOM data to find the correct region of interest as specified in the starting conditions. It will also match and align the structure slices to the corresponding shifted MVCT image slices. The resolution of the MVCT and the structure set differ in slice thickness so to determine which structure set slices are required the inbuilt Matlab function *ismember* is used to pinpoint the elements of the two matrix sets where the z coordinates are in correspondence. Only the image slices which have structure data associated with it will be passed back to the main script. The coordinates of the structure set will be saved to that patient directory to be used for the consecutive fractions to save reading them in again (unless the structure set is one that has been re-drawn on each MVCT set, in that case it is read in at each fraction). This function is only called once when investigating the target, when investigating OAR changes for the prostate patients this function is called at every fraction as the rectum has been redrawn on every fraction as part of the VoxTox study which these patients are enrolled on.

It has been assumed that,

- The target has been delineated correctly
- the target is in the correct location
- the target has not rotated

Water equivalent path-length code

In this function, the WEPL is calculated for a given beam direction, and beam parameters, using the shifted MVCT data and the effective depth algorithm previously described. To ensure the quality of the effective depth algorithm several verification tests have been carried out; these included testing the WEPL is accurate by setting the source to the surface of the CT image and the beam angle perpendicular to the pixels. This way the value of the pixel can be checked to determine if it was as expected and that the next pixel had a value equal to its own plus that of the previous pixel. An easy way to check the summation process is to look at water and see that the pixel value increases by a distance of one pixel each time.

Following the calculation of the WEPL, masks are used to pull the WEPL data from pixels that only exist inside the structure set for each fraction. Each subsequent fraction is then compared to the first (or the one was used of the first script). All dimensions are converted into distances and volumes and a histogram for each fraction depicting the percentage volume of the target that experiences a difference in WEPL in *mm* is created. A final histogram is created representative of the entire treatment. Statistical parameters such as the mean and standard deviation of each histogram is calculated, these represent the systematic and range errors associated with the treatment, both as a whole and at each fraction for that given beam angle.

Start conditions

Contents

- Start conditions
- Beam data
- Struct data
- Pat data

```
function [ Beam, Struct, Pat ] = HNstart_cons(Beam, Pat)

%The start coonditions are set by the user here
% The beam structure contains beam information.
% The Struct struct contain info about the structure ROI.
% The Pat structure contains info about that patient.
```

Beam data

```
Beam.beam_angle=45; % define the beam angle, can define elsewhere
Beam.Type=0; % 1=orsay, 0 = tomo
Beam.source_isocentre=7000; %based on CNOA data
Beam.beam_rad=Beam.beam_angle*(pi/180);% converts to rads
```

Struct data

```
Struct.number=1; % to set how many structure sets to analyse
% Struct.volume(2).ROI='rectum'; % define the ROI
% Struct.volume(2).let=8; %how many letters
Struct.volume(1).ROI='ctv65';%'CTV65'; % define the ROI
Struct.volume(1).let=3;
```

Pat data

```
Pat.token =102; % could be set else where
Pat.tok = num2str(Pat.token);
Mac=1; %set whether running on a mac or windows operating system
Windows=0;
CompU=Mac;
```

```

Pat.prostate=0;
Pat.headneck=1;
% creates directory paths to be used
if CompU>Windows;
    Pat.direct_name = ...
        (['/Users/staceymcgowan/Documents/PhD WEPL/HN/Data/'...
        ,Pat.tok]);
    s= exist([Pat.direct_name ...
        '/data_',num2str(Beam.beam_angle)], 'dir');
    if s <1
        mkdir([Pat.direct_name '/data_',num2str(Beam.beam_angle)]);
        % creates directory if there is not one already
    end
    Pat.direct_nameD = ...
        (['/Users/staceymcgowan/Documents/PhD WEPL/HN/Data/'...
        ,Pat.tok,'/data_',num2str(Beam.beam_angle)]);
    Pat.direct_nameResults = ...
        (['/Users/staceymcgowan/Documents/HN/Data/'...
        Pat.tok,'/results']);
else
    Pat.direct_name = (['R:\User Data\Stacey\Data\__Stacey\'...
        ,Pat.tok]);
    Pat.direct_nameD = ...
        (['R:\User Data\Stacey\Data\__Stacey\'...
        Pat.tok,'\data90']);
    Pat.direct_nameResults = ...
        (['R:\User Data\Stacey\Data\__Stacey\'...
        Pat.tok,'\results']);
end
Pat.Vox=1;
Pat.fract=1;
Pat.fraction =num2str(Pat.fract);

```

end of function

Runs functions for the first fraction

Contents

- Runs functions for the first fraction
- read in CT data
- Apply shift to CT data
- Find slices of MVCT and structure set that match
- calculate WEPL
- load mask of structure
- pull wepl data from structure mask
- end of function

```
%Need to read in the Target structure from the kVCT structure set and
%determine its coordinates. Determine which z slices to use.
function [Beam, Struct, Pat] = firstfraction(Beam, Pat)
```

```
[Beam, Struct, Pat] = start_cons(Beam, Pat);
%[sort]=sort_DailyImagesFUN(Pat); %run to organise images
folders = dir(Pat.direct_name);
yy=0; %counter
i = 1;
Pat.fract=i;
Pat.fraction = num2str(Pat.fract);
Pat.foldname = strcat(num2str(i));
time_folders=dir([Pat.direct_name '/' Pat.foldname]);
    for q = 1:length(time_folders)

        if (strcmp(time_folders(q).name,...
            '.') || strcmp(time_folders(q).name, '..')...
            || strcmp(time_folders(q).name, 'MVCTstruct')||...
            strcmp(time_folders(q).name, 'kVCTstruct')...
            || strcmp(time_folders(q).name, 'struct.dcm')...
            || strcmp(time_folders(q).name, '.DS_Store'))
            continue %skips files not required
        end
```

read in CT data

```
Pat.fract_directory = ...
    ([Pat.direct_name '/' Pat.foldname...
    '/' , time_folders(q).name]);
[ct_orig, Dicom_struct] = openimage_fun(Pat); %read CT
Pat.time=time_folders(q).name;
```

Apply shift to CT data

```
[shifted, Dicom_struct ]...
    = applyZ_fun( Dicom_struct, Pat, ct_orig);
```

Find slices of MVCT and structure set that match

```
[Struct, b, d, ct_knownS]... %read structure set
    = firstfractionStruct(Dicom_struct, Struct, Pat, yy);
%ct_knownS=ct_knownS-30;
disp('shift applied')
```

calculate WEPL

```
[ wepl ] = ...
    Wepl_VOXfunfirstCAL( Dicom_struct, Beam, Pat, ct_knownS, yy);
```

load mask of structure

```
Target=load([Pat.direct_nameD '/' , '1structmask.mat']);
logic=logical(Target.thisMAT); % make mask
```

pull wepl data from structure mask

```
needed=wepl(logic);
%nnn = viewing(logic, ct_knownS, Dicom_struct)
if yy <1 % dtermines whether more than one MVCT per #
save([Pat.direct_nameD, '/' , num2str(Pat.fract), ...
    'result1.mat'], 'needed');
```

```
yy=1;
else
    save([Pat.direct_nameD, '/' ,num2str(Pat.fract),...
        'result2.mat'], 'needed');
end

end
```

end of function

Next Fraction

Contents

- Next Fraction
- Clean up slice matrix
- match up slices to Structure set
- end of function

Runs through consecutive fractions and runs all same functions. Except reading the structure DICOM as just load the previous one. unless structure set re drawn on MVCT

```
function [Beam, Struct, Pat] = nextfraction(Beam, Pat)

[ Beam, Struct, Pat ] = start_cons(Beam, Pat);
    %[sort]=sort_DailyImagesFUN(Pat);
folders = dir(Pat.direct_name);
no_fracts =(length(folders)-8);
for i =[2:36] %loop through fractions
yy=0;
Pat.fract=i
Pat.fraction =num2str(Pat.fract);
Pat.foldname = strcat(num2str(i));
time_folders=dir([Pat.direct_name '/' Pat.foldname]);
    for q = 1:length(time_folders)

        if (strcmp(time_folders(q).name, '.')...
            || strcmp(time_folders(q).name, '..')...
            || strcmp(time_folders(q).name, 'MVCTstruct')||...
            strcmp(time_folders(q).name, 'kVCTstruct') ...
            || strcmp(time_folders(q).name, '.DS_Store'))
            continue %skip unneeded folders
        end
        Pat.fract_directory = ...
            ([Pat.direct_name '/' Pat.foldname '/', time_folders(q).name]);
        [ct_orig, Dicom_struct] = openimage_fun(Pat);
        Pat.time=time_folders(q).name;
```

```
[shifted, Dicom_struct ] = applyZ_fun( Dicom_struct, Pat, ct_orig);
disp('shift applied')
MVCTslicemat =...%creates matrix of MVCT slice coords
    ((Dicom_struct.Iz_cord:-Dicom_struct.slicethickness:...
    Dicom_struct.Iz_cord-((Dicom_struct.no_files-1)...
    *Dicom_struct.slicethickness)));
disp(num2str(Dicom_struct.shifts(2)))
```

Clean up slice matrix

```
for iuh= 1:Dicom_struct.no_files
if MVCTslicemat(1,iuh) <0
    if MVCTslicemat(1,iuh) >(-1)
        MVCTslicemat(1,iuh)=0;
    end
end
end
for iuh= 1:Dicom_struct.no_files
if MVCTslicemat(1,iuh) >0
    if MVCTslicemat(1,iuh) <(1)
        MVCTslicemat(1,iuh)=0;
    end
end
end
end
N= num2str(MVCTslicemat,4);
MVCTslicemat= str2num(N);
```

match up slices to Structure set

```
%need to find the coords in the MVCTstructslicemat that match the values
%in the struct mat.
%These values are the correct cordinates to be saved in the mask matrix.
load([Pat.direct_named '/', 'structmat.mat']);
load([Pat.direct_named, '/1d.mat']);
LIA=ismember(MVCTslicemat, structmat(:,oned)); % do slices match?
LIAB=ismember(structmat(:,oned), MVCTslicemat);
```

```

% need this to work to find the nearest values also
[c,bb]=ind2sub(size(LIA), find(LIA==1)); %where do they match?
[a,d]=ind2sub(size(LIAB), find(LIAB==1));
[w,r,numb]=size(bb);
b=fliplr(bb)
load([Pat.fract_directory '/' , 'shifted.mat']);
%[sw,tw,yw]=size(shifted);

shifted(shifted<11)=0;
% if numb>=yw
% ct_knownS=shifted(:,:,b(1:yw));%check it is not d
% end
% if numb<yw
    ct_knownS=shifted(:,:,b);
% end
    %ct_knownS=ct_knownS-30;
    [ wepl ] = Wepl_VOXfunfirstCAL( Dicom_struct, Beam, Pat, ct_knownS, yy);
    imagesc(wepl(:,:,3));
    Target=load([Pat.direct_nameD '/' , '1structmask.mat']);
    logic=logical(Target.thisMAT);
    [sw,tw,ww]=size(logic);
    [sw,tw,dw]=size(wepl);
    % nnn = viewing(logic, ct_knownS, Dicom_struct);
%    if ww>=dw
%        needed=wepl(logic(:,:,1:dw));
%    end
%    if ww<dw
%        needed=wepl(logic(:,:,ww));
%    end
needed=wepl(logic(:,:,d));
%nnn = viewing(logic, ct_knownS, Dicom_struct)%check visually
    if yy <1
        save([Pat.direct_nameD, '/' , num2str(Pat.fract), 'result1.mat'], 'needed');
        yy=1;
    else

```

```
        save([Pat.direct_nameD, '/' ,num2str(Pat.fract), 'result2.mat'], 'needed');  
        yy=0;  
    end  
  
    end  
end
```

end of function

Read MVCT DICOM

Contents

- Read MVCT DICOM
- read in data
- get DICOM header info

```
function [ct_orig, Dicom_struct] = openimage_fun(Pat)

%UNTITLED2 Summary of this function goes here
% Detailed explanation goes here
%directory_name = ...
%uigetdir('/Users/staceymcgowan/dropbox/matlab/fun/');
%directory_name = ...
%uigetdir('C:/Documents and Settings/mcgowans/My Documents/MATLAB/');
```

read in data

```
files = dir([Pat.fract_directory '/*.dcm']);
ct_orig = double(dicomread([Pat.fract_directory '/' files(1,1).name]));
[r,c] = size(ct_orig);
ct_orig = zeros(r,c,length(files));
Dicom_struct.no_files=length(files);
for i = 1:length(files)
    filename = strcat(num2str(i),'.dcm');
    ct_orig(:,:,i) = dicomread([Pat.fract_directory '/' filename]);
    %opens directories so user can choose ct data set, 2D or 3D,
end
```

get DICOM header info

```
infor=dicominfo([Pat.fract_directory '/' files(1,1).name]);
%reads dicom header

[m,n]=size(ct_orig(:,:,1));
Dicom_struct.m=m;
Dicom_struct.n=n;
```

```
Dicom_struct.slicethickness=infor.SliceThickness;
Dicom_struct.ct_coord=infor.ImagePositionPatient(1);
Dicom_struct.pixelsize=infor.PixelSpacing(1);
Dicom_struct.huoffset=infor.RescaleIntercept; %gets the HU offset
Dicom_struct.Iz_cord=infor.ImagePositionPatient(3);
Dicom_struct.inst=infor.InstanceNumber;
%if Pat.prostate>0
Dicom_struct.shifts=infor.Private_0099_1011;
% else
% num= load('shifts11.mat');
% xshift=num.shiftdata(Pat.fract,1);
% yshift=num.shiftdata(Pat.fract,2);
% zshift=num.shiftdata(Pat.fract,3);
%Dicom_struct.shifts=[xshift, yshift, zshift];
if ischar(Dicom_struct.shifts)>0
    Dicom_struct.shifts=[0,0,0];
end

end
```

End of function

Apply CT shifts

Contents

- The shifts
- Apply shifts
- End of function

```
function [ shifted, Dicom_struct ] = applyZ_fun( Dicom_struct, Pat, ct_orig)

if Pat.Vox>0
zshift=Dicom_struct.shifts(2);
xshift=Dicom_struct.shifts(1);
yshift=Dicom_struct.shifts(3);
end

if Pat.Vox<1

if Pat.headneck>0;
% [num]= xlsread('C:/Documents and Settings/mcgowans/My Documents...
%/MATLAB/proton range study/code/HN_shifts.xls', Pat.pt);
[num]= ...
    xlsread('/Users/staceymcgowan/dropbox/matlab/fun/HN_shifts.xls'...
    ,Pat.pt);
end
if Pat.prostate>0
[num]= xlsread...
('C:/Documents and Settings/mcgowans/My Documents...
/MATLAB/proton range study/code/patient_shifts.xls'...
, Pat.pt);
%[num]= ...
xlsread('/Users/staceymcgowan/dropbox/matlab/fun/patient_shifts.xls'...
, Pat.pt);
end
```

The shifts

```

zshift=num(3,Pat.fract);
xshift=num(1,Pat.fract);
yshift=num(2,Pat.fract);

end

%convert from mm to pixel dimensions
dunSliceX=(xshift/Dicom_struct.pixelsize);
dunSliceY=(yshift/Dicom_struct.pixelsize);
dunSliceZ=(zshift/Dicom_struct.slicethickness);

%ct_cordz=Dicom_struct(Pat.fract).Iz_cord:-Dicom_struct.slicethickness:...
    *(Dicom_struct(Pat.fract).Iz_cord-((Dicom_struct.no_files-1)...
    *Dicom_struct.slicethickness));

```

Apply shifts

```

ct_cordz=1:Dicom_struct.no_files;
ct_cordx=1:Dicom_struct.n;
ct_cordy=ct_cordx;

[X, Y, Z]=meshgrid(ct_cordx, ct_cordy, ct_cordz);

%shift applied by cubic interpolation.
% 3D interp require 3D coord systems
% use meshgrid to create existing and new systems

Shift_cordz=ct_cordz+dunSliceZ;
Dicom_struct.zshiftmat=Shift_cordz;
Shift_cordx=ct_cordx-dunSliceX;
Shift_cordy=ct_cordy+dunSliceY;

[Xi, Yi, Zi]=meshgrid(Shift_cordx, Shift_cordy, Shift_cordz);
% 3D interp of data in old to new coord system
% new coord system is old one plus the shifts

```

```
shifted=interp3(X, Y, Z, ct_orig, Xi, Yi, Zi, 'cubic');

% no extrapolating use, so buffer with zeroes in x and y
% assume no pt truncation
% For missing data in z, copy last existing slice
%So...

if zshift == 0
    else
if zshift <0
    first =0;
    %find the coordinate of the first value >1
    if first < 1;
        for I=1:Dicom_struct.no_files
            if Shift_cordz(I) >1
                first=I;
                break
            end
        end
    end
    %jt=abs(floor(Shift_cordz(1)));
    j=first-1;
    w=ones(1,j).*(j+1) ;
    shifted(:,:,1:j)=shifted(:,:,w);
end

if zshift >0
    jt=abs(ceil(Shift_cordz(Dicom_struct.no_files)));
    j=abs(Dicom_struct.no_files-jt);
    q=Dicom_struct.no_files-(j-1):Dicom_struct.no_files;
    w=ones(1,j).*Dicom_struct.no_files-j;
    shifted(:,:,q)=shifted(:,:,w);
end
end
```

```

shifted(isnan(shifted)) = 0; %get rid of NaNs
\subsection{If prostate read in kV and apply shifts and make masks}
if Beam.beam_angle>0
MVCT=shifted;
[Dicom_struct, Pat, kVCT]=kvctreadin(Pat, Dicom_struct);
[Dicom_struct, Pat, kvCT_shifted]=kvctshift(Pat, Dicom_struct,kVCT);
width = Dicom_struct.kvm;
height = Dicom_struct.kvn;
radius = 193/Dicom_struct.kvpixelsize;
centerW = width/2;
centerH = height/2;
[W,H] = meshgrid(1:width,1:height);
mask = sqrt((W-centerW).^2 + (H-centerH).^2) < radius;

maskop=mask.*10;
maskop(maskop<10)=1;
maskop(maskop>1)=0;

mask_mat=ones(Dicom_struct.kvn,Dicom_struct.kvm,Dicom_struct.kvno_files);
for j=1:Dicom_struct.kvno_files
    mask_mat(:,:,j)=maskop;
end

kv_mask=mask_mat.*kvCT_shifted;

kv_mask(kv_mask(:,:,.)<100)=0;
kv_mask(kv_mask(:,:,.)>0)=924;
Dicom_struct.kv_mask=kv_mask;
%if Beam.beam_angle>0
    [Dicom_struct, Pat, MVCT] = painted(Dicom_struct, Pat, MVCT);
%end
one=Dicom_struct.need*2;
x=one+1:Dicom_struct.total;
y=Dicom_struct.need:(Dicom_struct.total-Dicom_struct.need-1);

```

```
shifted=MVCT(y,x,:);
end

clear ct_orig
% s= exist([Pat.direct_name '\ ' Pat.tok '\ ' Pat.fraction], 'dir');
% if s <1
% mkdir(Pat.direct_name, Pat.tok);
% mkdir([Pat.direct_name '/' Pat.tok], Pat.fraction);
% end
if Pat.prostate>0
    save([Pat.fract_directory '/' , 'shifted.mat'], 'shifted');
else
    j=Pat.foldname;
    save([Pat.direct_name '/' j '/' , 'shifted.mat'], 'shifted');
end

end
```

End of function

Read in structure DICOM set

Contents

- Read in structure DICOM set
- Get coordinates out of header
- Create z coordinate matrix of MVCT & structure set
- Storing the slices required
- end of function

```
%function loops through structure DICOM header
% pulls out coordinates for pre defined ROI
% stores this data in 3D matrix
% the slices in this matrix that match the MVCT slices are correlated
```

Get coordinates out of header

article graphicx color

```
function [Struct, b, d, ct_knownS, test]...
    = HNfirstfractionStruct(Dicom_struct, Struct, Pat)
    metadata = dicominfo([Pat.direct_name '/kVCTstruct.dcm']);
    %struct if HN
for j = 1:length(struct2cell(metadata.ROIContourSequence))
    % loop through number of structures
%j=48; %Loop modified from Nick Early's Loop
z = eval(['metadata.StructureSetROISequence.Item_' num2str(j) '.ROIName']);
    if strcmpi(z,Struct.volume(1).ROI,Struct.volume(1).let);
    % if j==2;
        disp(z);
        disp(j);
        g = eval(['length(struct2cell(metadata.ROIContourSequence.Item_'...
            num2str(j) '.ContourSequence)')]); % finds number of slices
        test.Storage(1).stores=zeros(Dicom_struct.m, Dicom_struct.n, g);
        %test.Storage(1).DEstores=zeros(Dicom_struct.m, ...
        Dicom_struct.n, Dicom_struct.no_files);
        %stores=zeros(100,3,g);
```

```

%storey=zeros(g,1);
for k = 1:g          % loop through all these slices
%k=27; %slice of interest number
s = ['metadata.R0IContourSequence.Item_' num2str(j)...
'.ContourSequence.Item_' num2str(k) '.ContourData'];%get cords
CD = eval(s);
CD = [CD; CD(1:3)]; %makes co-ords end where they start
st = -1 + length(CD)/3;%co-ords are all jumbled up (xyzxyz...)
d = [];    %this code splits them into 3 arrays d,e,f
e = [];
f = [];
for i = 0:st
    d(i+1) = CD(1+(3*i),1);
    Struct.cord(Pat.fract).volume(1).xpos(i+1)=d(i+1);
    e(i+1) = CD(2+(3*i),1);
    Struct.cord(Pat.fract).volume(1).ypos(i+1)=e(i+1);
    f(i+1) = CD(3+(3*i),1);
    Struct.cord(Pat.fract).volume(1).zpos(i+1)=f(i+1);

end
cord1=d';
cord2=e';
cord3=f';
if k==1
    Pat.first=cord3(1);
    % Pat.first=3;
end
if k==2
    Pat.structslice= abs(Pat.first-cord3(1));
%Pat.structslice=1;
end
A=[cord1, cord2, cord3];
pos_x = (cord1-Dicom_struct.ct_coord+Dicom_struct.pixelsize)...
/Dicom_struct.pixelsize;
pos_y = (cord2-Dicom_struct.ct_coord+Dicom_struct.pixelsize)...

```

```

        /Dicom_struct.pixelsize;
        %pos_y = 512-pos_ys;
        pos_z=k;
        %((cord3+Dicom_struct.Iz_cord+Pat.structslice)/Pat.structslice)

        roi_mask = poly2mask(pos_x, pos_y, 512, 512);
        test.Storage(1).stores(:,:,k)=roi_mask;
        end
    end
end

\subsection*{Storing the slices required}
MVCTslicemat =(((Dicom_struct.Iz_cord:-Dicom_struct.slicethickness...
    :Dicom_struct.Iz_cord-((Dicom_struct.no_files-1)*...
    Dicom_struct.slicethickness))) -Pat.eee);%took-1 out
[hjk,mvctslice]=size(MVCTslicemat);
%Dicom_struct.no_files=mvctslice;
for iuh= 1:Dicom_struct.no_files
if MVCTslicemat(1,iuh) <0
    if MVCTslicemat(1,iuh) >(-1)
        MVCTslicemat(1,iuh)=0;
    end
end
end
for iuh= 1:Dicom_struct.no_files
if MVCTslicemat(1,iuh) >0
    if MVCTslicemat(1,iuh) <(1)
        MVCTslicemat(1,iuh)=0;
    end
end
end
end%+Dicom_struct.shifts(1,3)
N= num2str(MVCTslicemat,4);
MVCTslicemat= str2num(N);

structmat=(Pat.first:Pat.structslice:Pat.first+(Pat.structslice*g-1));

```

```
%MVCTslicemat(MVCTslicemat<Pat.end)=NaN; % use to avoid slice (shoulders)
%structmat(structmat<Pat.end)=NaN;
LIA=ismember(MVCTslicemat, structmat); %finds matches
LIAB=ismember(structmat, MVCTslicemat);
[c,bb]=ind2sub(size(LIA), find(LIA==1));
[a,dd]=ind2sub(size(LIAB), find(LIAB==1));
[r,numb]=size(bb);
%d=fliplr(dd)
%b=fliplr(bb);
d=dd;
thisMAT=zeros(Dicom_struct.m, Dicom_struct.n, numb);
thisMAT=test.Storage(1).stores(:,:,d);
%disp(d);
    oned=d%+facto;
save([Pat.direct_nameD, '/', num2str(Pat.fract), 'd.mat'], 'oned');
j=Pat.fraction;
load([Pat.direct_name '/', j, '/shifted.mat']);
shifted(shifted<11)=0;
b=fliplr(bb);
%b=bb;
ct_knownS=shifted(:,:,b);%check it is not d
save([Pat.direct_nameD '/', , 'structmat.mat'], 'structmat');
save([Pat.direct_nameD '/', num2str(1), 'structmask.mat'], 'thisMAT');
nnn = viewing(thisMAT, ct_knownS, Dicom_struct)
%clear test;
clear roi_mask
end
```

This LaTeX was auto-generated from an M-file by MATLAB.

Water equivalent path-length code

Contents

- Water equivalent path-length code
- Set up beam conditions
- WEPL loop
- end of function

`%Wep1_VOXfun` is a function that requires beam, Dicom and patient data to then determine the wepl path length of a patient Data set. The calibration details for converting HU to relative proton stopping power for MVCT are included, kVCT could also be added with new cal. This code can be used for photons by adding a new calibration curve.

Set up beam conditions

```
function [ wepl ] = Wep1_VOXfunfirstCAL...
    ( Dicom_struct, Beam, Pat, ct_knownS,yy)

%Modified from Dr Simon Thomas' code
xiso=(Dicom_struct.n/2+1);
ziso=(Dicom_struct.m/2+1);
sid=(Beam.source_isocentre/(Dicom_struct.pixelsize));
%sets up centre of data and isocentre
xf=xiso +(sid*sin(Beam.beam_rad));
%finds x coord of focus (centre of rotation is at centre of CT)
zf=ziso-(sid*cos(Beam.beam_rad));
%finds z coord of focus
xsp=1:Dicom_struct.n;
xp= repmat(xsp, 1, Dicom_struct.n);
%each element is the x coord of the mxn matrix and is in 1 row
nB=1:Dicom_struct.m;
Brep=repmat(nB,Dicom_struct.n,1);
zp=reshape(Brep,1,((Dicom_struct.m)*(Dicom_struct.n)));
```

```

%each element is the z coord of the mxn matrix and is in 1 row
dx=xf-xp;
%distance from focus to point of interest in x
dz=zf-zp;
%distance from focus to point of interest in y
steps=max((max(abs(dx),abs(dz)))));
%number of intervals for later
rl=sqrt(dx.*dx + dz.*dz);
%distnce from point of interest to source
dr=rl/steps;
deltax=dx/steps;
deltaz=dz/steps;
x=xp;
z=zp;
%so can keep original values of xp and zp (zp,xp is coords)
rpath=0;
clear Brep
[a,b,no_slices]=size(ct_knownS);
v=ones((Dicom_struct.m+2),1)*(1);
t=ones(1,Dicom_struct.n)*(1);
C=zeros(Dicom_struct.n+2, Dicom_struct.m, no_slices);
G=zeros(Dicom_struct.n+2, Dicom_struct.m+2, no_slices);
for tt = 1:no_slices
    C(:,:,tt)=[t;ct_knownS(:,:,tt);t];
    G(:,:,tt)=[v C(:,:,tt) v];
end
ct=permute(G, [3 1 2]);
%reorders pt dtata in the form of slicesx261244
Gdim=max(size(ct));
Gsize=Gdim*ones(1,2);

```

WEPL loop

```

%Loop structure from Dr Simon Thomas
for i=1:steps

```

```
%loop to calculate water equivalent path to the point of interest
iz=round(z);
iz(iz<1)=1; iz(iz>Gdim)=1;
ix=round(x);
ix(ix<1)=1; ix(ix>Gdim)=1;
use 1 as flag both sizes
if max(iz)==1, break, end
if max(ix)==1, break, end
hu=double(ct(:,sub2ind(Gsize,iz,ix)))+Dicom_struct.huoffset;
%gets hu value from ct
%hu=ctimages(:,sub2ind(ctsize,iz,ix));
hu(hu<=(-900))=-1000;
%for air so it does contribute to the water equivalent path
fhu=double(hu);
    if Beam.Type<1 %new cal
rhop=0.9652+(0.0009914*fhu);
rhop(rhop<0)=0;          %trap negative densities
end
end
if Beam.Type>0 %orsay cal
rhop=1.0153+(fhu/1000); % A
rhop2=1.0152+(fhu.^3*4e-08)+(fhu.^2*6e-06)+(0.0006*fhu);
rhop3=1.0356+(fhu/1111.11);
rhop(rhop<0.812)=0;
rhop(rhop>0.812)=rhop2(rhop>0.812);
rhop(rhop>1.065)=rhop3(rhop>1.065);
end
rpath=rpath+rhop;
%sums the previous relative electron densities and
%will get multiplied by distance dr later
x=x+deltax;
z=z+deltaz;
end
a=ones(no_slices,1);
dr2=a*dr; %
```

```

rpath=rpath.*dr2;
%water equivalent path length for all slices
wepl=permute(rpath, [2 1]);
wepl=reshape(wepl,Dicom_struct.n, Dicom_struct.m, no_slices);
wepl=permute(wepl, [2 1 3]);
%puts matrix into conventional order of (XxY)xZ
if yy <1
    save([Pat.direct_nameD '/' , num2str(Pat.fract),'wepl1'], 'wepl');
    yy=1;
else
    save([Pat.direct_nameD '/' , num2str(Pat.fract),'wepl2'], 'wepl');
end

```

end of function

Results code Fraction Data

Contents

- Stats for fraction bit!
- Plot bit fraction bit
- Cumulative
- Entire Treatment bit
- codes

```
function [Beam] = ResultsOut( Beam)
```

```

count=0;
statsdatastore=zeros(5, 12);
for beam_angle=[0,90];

    count=count+1;
    Beam.beam_angle=beam_angle;
    Pat.token=21;
    bnb=36;
    Dicom_struct.pixelsize=0.7647;
    Dicom_struct.slicethickness=6;

```

```

Dicom_struct.no_files=bnbn;
storingHIST=zeros(Dicom_struct.no_files+2, 58);
storingCUML=zeros(Dicom_struct.no_files+2, 58);
[ Beam, Struct, Pat ] = start_cons(Beam, Pat);
% if Beam.beam_angle > 0
%     sheet=Pat.token;
% else
%     sheet=Pat.token+1;
% end
%folders = dir(Pat.direct_nameD);
no_fracts = bnbn;
getfirst=load([Pat.direct_nameD '/' ,num2str(1),'result1.mat']);
[resSize,tyh]=size(getfirst.needed);
gotn=zeros(resSize,1);
goth=zeros(resSize,1);
got_again=zeros(resSize,no_fracts-1);
counter=0;
hgf=[17 36 15 18 11 19 3 10 27 35 12 32];
for i = [17 36 15 18 11 19 3 10 27 35 12 32]

    %2:3,7,10:12,16,17,23,31,33,34 to
    %1?5,6,8,9,15,18:20,24:30,36 to4? -pt 78
    counter=counter+1;
    getnext=load([Pat.direct_nameD '/' num2str(i),'result1.mat']);
    neededfirst=getfirst.needed.*Dicom_struct.pixelsize;
    needednext=getnext.needed.*Dicom_struct.pixelsize;
    got=(needednext-neededfirst);

    gotn=gotn+got;

```

Stats for fraction bit!

```

metadata=mean(got);
got_again(:,i-1)=got;
mi=min(got);
mx=max(got);

```

```

st=std(got);
varian=var(got);
storingHIST(i,52)=metadata;
%storing(i,103)=mod;
storingHIST(i,53)=varian;
storingHIST(i,54)=st;
storingHIST(i,55)=mi;
storingHIST(i,56)=mx;
%v=linspace(mi,mx,100);

```

Plot bit fraction bit

```

v=-50:2:50;
[numbe,a]=size(got);
%h_vol=(numbe*(Dicom_struct.pixelsize*Dicom_struct.pixelsize...
%*Dicom_struct.slicethickness));
whole_vol=(numbe*(Dicom_struct.pixelsize*Dicom_struct.pixelsize...
    *Dicom_struct.slicethickness))/1000;%cm cubed
h_vol=(Dicom_struct.pixelsize*Dicom_struct.pixelsize*...
    Dicom_struct.slicethickness);%mm cubed
totalvol=h_vol*numbe;%mm cubed
totalvoll=repmat(totalvol,1,51);
h=got;
hh=hist(h, v);
normed=((hh.*h_vol)./totalvoll).*100;
storingHIST(1,1:51)=v;
storingHIST(i,1:51)=normed;
    handle(i)=figure(i);
    plot(v, normed);
    xlabel('Change in WEPL (mm)');
    ylabel('%Volume');
    %title(['Range Volume Histogram: Interfraction WEPL changes in fraction',...
    % num2str(i), ' - pt ',num2str(Pat.token), ' prostate ', ...
    %num2str(Beam.beam_angle), ' coplanar beam']);
saveas(handle(i),[Pat.direct_nameD, '/' , num2str(Beam.beam_angle)...

```

```
,Pat.tok,'_', num2str(i),'_', 'Hist.png'], 'png');
```

Cumulative

```
totalvoll= repmat(totalvol,1,51);
cuh=abs(got);

goth=goth+cuh;

cvg=0:0.5:25;
cuhh=(hist(cuh, cvg));
cuhc=cumsum(cuhh);
cumnormedd=(((cuhc.*h_vol)./totalvoll).*100);
cumnormed=(cumnormedd*(-1))+100;
%cumnormed(cumnormed>100)=100;
%cumnormed(cumnormed<0.5)=0;
handle(i+40)=figure(i+40);
plot(cvg, cumnormed);
xlabel('Change in WEPL (mm)');
ylabel('%Volume');
%title(['Cumulative Range Volume Histogram: Interfraction WEPL ...
%changes in fraction',...
% num2str(i), ' - pt ',num2str(Pat.token), ' prostate '...
%, num2str(Beam.beam_angle), ' coplanar beam']);
saveas(handle(i+40),[Pat.direct_nameD, '/' , num2str(Beam.beam_angle...
),Pat.tok,'_', num2str(i),'_', 'Cuml.fig'], 'png');
storingCUML(1,1:51)=cvg;

storingCUML(i, 1:51)=cumnormed;

ggett=[2,3,5,10,20]; % vol getting range mm
pervols=interp1(cvg, cumnormed, ggett);
storingCUML(i,52:56)=pervols;

end
```

Entire Treatment bit

```

v=-50:2:50;
disp(counter)
gotT=gotn./(counter-1);
%gotT=sum(got_again,2);
[numbe,a]=size(gotT);
%h_vol=(numbe*(Dicom_struct.pixelsize*Dicom_struct.pixelsize*...
%Dicom_struct.slicethickness));
whole_vol=(numbe*(Dicom_struct.pixelsize*Dicom_struct.pixelsize...
    *Dicom_struct.slicethickness))/1000;%cm cubed
h_vol=(Dicom_struct.pixelsize*Dicom_struct.pixelsize...
    *Dicom_struct.slicethickness);%mm cubed
totalvol=h_vol*numbe;%mm cubed
totalvoll= repmat(totalvol,1,51);
h=gotT;
hh=hist(h, v);
normed=((hh.*h_vol)./totalvoll).*100;

% storingHIST((i+1),:)=sum(storingHIST(2:no_fracts+1,:),1);
% storingHIST((i+2),:)=storingHIST(i+1,:)./no_fracts;
handle(31)= figure(31);
plot(v, normed);

% stdevT=std(gotn/36)
% VarT=var(gotn/36)
xlabel('Change in WEPL (mm)', 'fontsize', 12);
ylabel('%Volume', 'fontsize', 12);
%title(['Range Volume Histogram: Interfraction WEPL changes in pt '...
%,num2str(Pat.token), ' sacrum, ', num2str(Beam.beam_angle)...
%, 'degree beam'], 'fontsize', 12);
saveas(handle(31),[Pat.direct_nameD, '/' , num2str(Beam.beam_angle)...
    ,Pat.tok,'_', 'THist.png'], 'png');
metadata=sum(gotn)./(36*resSize);

handle(32)=figure(32);

```

```

scatter(hgf, storingHIST(hgf, 54));
lsline
xlabel('fraction', 'fontsize', 12);
ylabel('stdev', 'fontsize', 12);
%title(['Pt ', num2str(Pat.token), ', ' num2str(Beam.beam_angle),
%'degree beam - stdev of change in range in CTV
%relative to first fraction'], 'fontsize', 12);
saveas(handle(32), [Pat.direct_nameD, '/' ,...
    num2str(Beam.beam_angle), Pat.tok, '_ ', 'StDev.png'], 'png');
%mod=mode(gotn)
mi=min(storingHIST(2:no_fracts,55));
mxsys=max(storingHIST(2:no_fracts,52));
misys=min(storingHIST(2:no_fracts,52));
mx=max(storingHIST(2:no_fracts,54));
meanT=mean(gotT);
stdev_thistimeB=sqrt(sum(storingHIST(i,53)));
stdec_thistimeC=std(gotT);
stdev_thistimeD=mean(storingHIST(i,54));
storingHIST(i+2,52)=meanT;
storingHIST(i+2,53)=sum(storingHIST(i,53));
storingHIST(i+2,54)=stdev_thistimeB;
storingHIST(i+2,55)=misys;
storingHIST(i+2,56)=mxsys;
storingHIST(i+2,57)=stdec_thistimeC;
storingHIST(i+2,58)=(sum(storingHIST(i,53)))/(sqrt(counter-1));

cuh=abs(gotT);
cuhh=(hist(cuh, cvg));
cuhc=cumsum(cuhh);
cumnormedd=((cuhc.*h_vol)./totalvoll).*100;
cumnormed=(cumnormedd*(-1))+100;

handle(33)=figure(33);
plot(cvg, cumnormed);
xlabel('Change in WEPL (mm)', 'fontsize', 12);

```

```

ylabel('%Volume', 'fontsize', 12);
%title(['Cumulative Range Volume Histogram: Interfraction
%WEPL changes in pt ', num2str(Pat.token), ' Sacrum, ',
%num2str(Beam.beam_angle), 'degree beam'], 'fontsize', 12);

saveas(handle(33), [Pat.direct_nameD, '/' , ...
    num2str(Beam.beam_angle), Pat.tok, '_', 'TCuml.png'], 'png');
pervolsT=interp1(cvg, cumnormed, ggett);
storingCUML(i+2,52:58)=[pervolsT,0,0];
%storingHIST(1,52:58)=[ 'mean', 'var', 'std', 'min', 'max', 'C', 'SE'];
% figure(i+41)
% plot(cv, storingCUML(i+2,1:51));

%storingHIST(1, 52:56)=[ 'Mean', 'std', 'Max', 'Min', 'hmm'];
%storingCUML(1, 52:56)=[ 'V3%', 'V5%', 'V7%', 'V10%', 'V50%'];
storingone=[storingCUML];
storing=storingHIST;
statsdata=[storingHIST(i+2,52:58) , pervolsT];
statsdatastore(count, :)=statsdata;
%save([Pat.direct_nameD, '/' , num2str(Beam.beam_angle), 'stats.mat'],
%'statsdata');
% for bb=[2:32];
%     savefig([Pat.direct_nameD, '/' , num2str(Beam.beam_angle),
%Pat.tok, num2str(bb), handle(bb), 'Hist.fig']);
% end
% for bb=[41:72];
%     savefig([Pat.direct_nameD, '/' , num2str(Beam.beam_angle),
%Pat.tok, num2str(i), handle(bb), 'cuml.fig']);
% end
% savefig([Pat.direct_nameD, '/' , num2str(Beam.beam_angle), Pat.tok,
%num2str(i), handle(73), 'stdev.fig']);
%savefig([Pat.direct_nameD, '/'
%, num2str(Beam.beam_angle), handle(2), 'figcuml.fig']);
titleh = ['hist', num2str(Pat.token), '_', num2str(Beam.beam_angle)];
%titlel = ['HN2cuml', num2str(Pat.token), '_', num2str(Beam.beam_angle)];

```

```

dlmwrite(titleh, storing, 'delimiter', '\t');
xlswrite([titleh,'.xlsx'], storing);
%xlswrite([titleh,'.xlsx'], storingone);
%close(handle)
%save([Pat.direct_nameResults '/' ,Pat.tok, '
%NcalHist_data', num2str(Beam.beam_angle)], 'storing');

```

end of function

article graphicx color

```

function [Beam] = ResultsOut_all( Beam)
got_all=zeros(7,2);
anothercounter=0;
for beam_angle=[0, 25,70,110,180];
    anothercounter=anothercounter+1;

    Beam.beam_angle=beam_angle;
counter=0;
    for token= [35,51,52,78,91,92,102]
        counter=counter+1;
        Dicom_struct.pixelsize=0.7647;
Pat.token=token;
[ Beam, Struct, Pat ] = HNstart_cons(Beam, Pat);
co=1;
fractions=[2:30];
if token==51
    fractions=[3:6,8,10,15:20,22:25,27:31];
    co=2;
end
if token==102
    co=2;
    fractions=[3:5,7:9,11,12,18:21,23:25,27:35,37,39:40];
end
getfirst=load([Pat.direct_nameD '/' ,num2str(co),'result1.mat']);
[resSize,tyh]=size(getfirst.needed);

```

```
got_again=zeros(resSize,37);

if token==52
    fractions=[4:18,20:34];
end
if token==91
    fractions=[2,4:6,8:30];
end

for i = fractions
    getnext=load([Pat.direct_nameD '/' num2str(i),'result1.mat']);
    neededfirst=getfirst.needed.*Dicom_struct.pixelsize;
    needednext=getnext.needed.*Dicom_struct.pixelsize;
    got=(needednext-neededfirst);

    got_again(:,i-1)=got;
end

Store.token(counter).squareit=sum(sum(got_again.^2));
Store.token(counter).summer=sum(sum(got_again));
Store.token(counter).numall=length(fractions)*resSize;
end

Tl=[Store.token(1).squareit,Store.token(2).squareit,...
    Store.token(3).squareit,Store.token(4).squareit,...
    Store.token(5).squareit,Store.token(6).squareit,...
    Store.token(7).squareit];

Sl=[Store.token(1).summer,Store.token(2).summer,...
    Store.token(3).summer,Store.token(4).summer,...
    Store.token(5).summer,Store.token(6).summer,...
    Store.token(7).summer];

Nl=[Store.token(1).numall,Store.token(2).numall,...
    Store.token(3).numall,Store.token(4).numall,...
```

```
    Store.token(5).numall,Store.token(6).numall,...  
    Store.token(7).numall];  
  
N=sum(N1);  
S=sum(S1);  
T=sum(T1);  
mean = S/N;  
sd=sqrt((T/N)-((S/N)^2));  
got_all(anothercounter,:)= [mean, sd];  
end  
end
```

end of function